Dissertations   Electronic Theses and Dissertations

12-31-2020

Characterizing reactive iron mineral coatings and their roles in natural attenuation at a site with historical contamination

Han Hua
New Jersey Institute of Technology

Recommended Citation

ABSTRACT

CHARACTERIZING REACTIVE IRON MINERAL COATINGS AND THEIR ROLES IN NATURAL ATTENUATION AT A SITE WITH HISTORICAL CONTAMINATION

by
Han Hua

Reactive iron mineral coatings in redox transition zones play an important role in contaminant attenuation. These mineral coatings include poorly crystalline to crystalline iron sulfides, carbonates, and oxyhydroxides, and are a signature of the biogeochemical processes occurring. To better understand these processes, reactive iron mineral coatings are characterized in an 18-m Anaerobic Core collected from a contaminated industrial site. This study targets redox transition zones uncovered in the core. A suite of complementary analyses is applied to distinguish the surface coating mineralogy using X-ray Diffraction, X-ray fluorescence, and field-emission scanning electron microscopy (FESEM) with energy dispersive X-ray analyzer (EDX). In the shallowest redox transition zones, framboidal pyrite and greigite are observed in the clay lenses, while iron (III) phases in the aquifer include goethite, ferrihydrite, lepidocrocite, and hematite. In the transition zone in aquitard, iron sulfides are found as flaky aggregates of mackinawite, pyrite, and pyrrhotite. In addition, the iron (II)/(III) mineral magnetite is also observed in this same area. Other related data such as groundwater chemistry and microbial genera are also collected. Possible cycling pathways for Fe and S mineral coatings are proposed and compared between transition zones. Using multiple lines of evidence, the shallowest two redox transition zones are expected to play a significant role in the degradation of site contaminants. Reactions in other redox transition zones may be slower where iron mineral coatings are not dominant.

The identified reactive iron mineral coatings in the Anaerobic Core are compared with a Cryo Core which has been collected with the cryogenic technique applying liquid nitrogen. After thawing the Cryo Core in an oxygen-free glovebox, the same suite of analyses is applied. Among the iron minerals identified, crystalline pyrite is found throughout the Cryo Core sediment samples, which contrasts with that observed for the Anaerobic Core. Moreover, mackinawite and greigite which are ubiquitous in the Anaerobic Core were not observed in Cryo Core samples. Meanwhile, a freeze/thaw process is simulated on Anaerobic Core samples using a liquid-nitrogen quench with surface coatings characterized by FESEM/EDX. In these quenched samples, mackinawite is no longer observed, and in its place was pyrite. In addition, both greigite and pyrite are found to be unique morphologically after quenching. Dissolution and re-precipitation of iron sulfide coatings during the freeze/thaw process appears to affect the geochemistry of the pore water through two main mechanisms of freeze-concentration and freezing potential.

Overall, reactive mineral coatings characterized with multiple chains of evidence are important contributor to the natural attenuation processes of contaminants of concern in redox transition zones.

**CHARACTERIZING REACTIVE IRON MINERAL COATINGS AND
THEIR ROLES IN NATURAL ATTENUATION
AT A SITE WITH HISTORICAL CONTAMINATION**

by
Han Hua

A Dissertation
Submitted to the Faculty of
New Jersey Institute of Technology
in Partial Fulfillment of the Requirements for the Degree of
Doctor of Philosophy in Environmental Engineering

John A. Reif, Jr. Department of Civil and Environmental Engineering

December 2020

APPROVAL PAGE

CHARACTERIZING REACTIVE IRON MINERAL COATINGS AND THEIR ROLES IN NATURAL ATTENUATION AT A SITE WITH HISTORICAL CONTAMINATION

Han Hua

Dr. Lisa B. Axe, Dissertation Advisor	Date
Professor of Civil and Environmental Engineering, NJIT	
Chair of Department of Chemical and Materials Engineering	

Dr. James Dyer, Committee Member	Date
Savannah River National Laboratory, Aiken, South Carolina	

Dr. Donna E. Fennell, Committee Member	Date
Professor of Environmental Sciences, Rutgers University, New Brunswick, New Jersey	

Dr. Wen Zhang, Committee Member	Date
Associate Professor of Civil and Environmental Engineering, NJIT	

Dr. Lucia Rodriguez-Freire, Committee Member	Date
Assistant Professor of Civil and Environmental Engineering, NJIT	

Dr. Michel Boufadel, Committee Member	Date
Professor of Civil and Environmental Engineering, NJIT	

BIOGRAPHICAL SKETCH

Author: Han Hua

Degree: Doctor of Philosophy

Date: December 2020

Undergraduate and Graduate Education:

- Doctor of Philosophy in Environmental Engineering,
  New Jersey Institute of Technology, Newark, NJ, 2020

- Master of Science in Environmental Engineering,
  New Jersey Institute of Technology, Newark, NJ, 2014

- Bachelor of Science in Environmental Engineering,
  Shanghai Ocean University, Shanghai, P. R. China, 2011

Major: Environmental Engineering

Publications:

Hua H, Yin X, Dyer JA, Landis R, Axe L. A Geochemical Study on Reactive Iron Mineral Coatings in Anaerobic Contaminated Sediment, under preparation for publication.

Hua H, Yin X, Dyer JA, Landis R, Axe L. Characterizing Reactive Iron Mineral Coatings in Redox Transition Zones, *ACS Earth and Space Chemistry* (2020), https://doi.org/10.1021/acsearthspacechem.0c00233.

Hua H, Yin X, Renno MI, Sale TC, Dyer JA, Landis R, Axe L. Impacts of Cryogenic Sampling Processes on Iron Mineral Coatings in Contaminated Sediment, *Science of the Total Environment* (2020), https://doi.org/10.1016/j.scitotenv.2020.142796.

Yin X, Hua H, Burns RF, Fennell D, Dyer JA, Landis R, Axe L. Identifying Redox Transition Zones in the Subsurface from a Site with Historical Contamination, *Science of the Total Environment* (2020), https://doi.org/10.1016/j.scitotenv.2020.143105.

Yin X, Hua H, Dyer JA, Axe L. Investigating Reactive Iron Minerals Cycling in Redox Transition Zones from the Site with Historical Contamination with Sequential Extraction, under preparation for publication.

Landis R, Hua H, Axe L, Morgan S. Biogeochemical Coring and Preservation Method for Unconsolidated Soil Samples, *Groundwater Monitoring & Remediation*, under review.

Presentations:

Hua H, Yin X, Renno MI, Sale TC, Landis R, Dyer JA, Lisa A. "Impacts of Cryogenic Sampling Processes on Iron Mineral Coatings in Contaminated Sediment", ACS Fall 2020 Virtual Meeting & Exposition, online poster, March 2020.

Ding W, Hua H, Yin X, Axe L. "Abiotic Degradation of 1,4-Dichlorobenzene with Reactive Iron Mineral Coatings", 2019 AIChE Annual Meeting, Hyatt Regency, Orlando, US, November 10-15, 2019.

Hua H, Yin X, Axe L. "Reactive Iron Mineral Coatings in Redox Transition Zones" (updated version), session: reactions at the mineral-fluid interface: dissolution, precipitation and controls on geochemical element cycling, Goldschmidt Conference, Boston, Massachusetts, US, August 12-17, 2018.

Yin X, Hua H, Axe L. "Determining Reactive Iron Mineral Contributions in Redox Transition Zones with Sequential Extraction", 28th Goldschmidt Conference, Boston, Massachusetts, US, August 12-17, 2018.

Hua H, Yin X, Axe L. "Reactive Iron Mineral Coatings in Redox Transition Zones", session: site investigation, 33rd Annual International Conference on Soils, Sediments, Water, and Energy, Amherst, Massachusetts, US, October 2017.

Yin X, Hua H, Axe, L. "Identifying Redox Transition Zones in the Subsurface" (Poster), 33rd Annual International Conference on Soils, Sediments, Water, and Energy, Session: Site Investigation, Amherst, Massachusetts, US, October 16-19, 2017

Hua H, Yin X, Axe L. "Characterizing Reactive Iron Mineral Coatings in Redox Transition Zones" (updated version), Iron & Manganese Oxides: Their Formation, Structure, Reactivity & Applications Symposium, 254th American Chemical Society Meeting & Exposition, Washington DC, US, August 20-24, 2017.

Yin X, Hua H, Axe L. "Identifying Redox Transition Zones in the Subsurface", Iron & Manganese Oxides: Their Formation, Structure, Reactivity & Applications Symposium, 254th American Chemical Society Meeting & Exposition, Washington DC, US, August 20-24, 2017

Hua H, Yin X, Axe L. "Characterizing Reactive Iron Mineral Coatings in Redox Transition Zones", Fate & Transport of Environmental Contaminants Symposium, 45th Middle Atlantic Regional Meeting of the American Chemical Society, Hershey, Pennsylvania, US, June 4-6, 2017.

Yin X, Hua H, Axe L. "Identifying Redox Transition Zones in the Subsurface", Fate & Transport of Environmental Contaminants Symposium, 45th Middle Atlantic Regional Meeting of the American Chemical Society, Hershey, PA, US, June 4-6, 2017

To my parents, Jindong Hua (华敬东) and Yan Zhu (朱琰),

for their patience, understanding, support, and love.

ACKNOWLEDGMENT

TABLE OF CONTENTS

TABLE OF CONTENTS
(Continued)

LIST OF TABLES

LIST OF FIGURES

ABBREVIATIONS

ACS   American Chemical Society

cis-DCE   cis-dichloroethene

COC   Contaminants of concern

DBS   Depth below the surface

EPA   Environmental Protection Agency

FESEM/EDX   Field-emission scanning electron microscopy with energy

                            dispersive X-ray analyzer

FeRM   Fe(III)-reducing microorganisms

ICDD   International Centre for Diffraction Data

ICSD   Inorganic Crystal Structure Database

MLS   Multi-Level System

MNA   Monitored natural attenuation

NAPL   Nonaqueous-phase liquid

ORP   Oxidation reduction potential

OUT   Operational taxonomic unit

PAH   Polycyclic aromatic hydrocarbon

PCE   Perchloroethylene

QLL   Quasi-liquid layer

RIR   Reference intensity ratios

RNA   Ribonucleic acid

RTZ   Redox transition zone

SE	Sequential extraction
TCA	Trichloroacetic acid
TCE	Tricholoroethylene
VOC	Volatile organic compound
XRD	X-ray diffraction
XRF	X-ray fluorescence
ZVI	Zero-valent iron

CHAPTER 1

INTRODUCTION

Reductive dehalogenation with reactive iron minerals plays an important role in the natural attenuation of chlorinated organic solvents.[1] Given the continuous process of precipitation and dissolution both biotically and abiotically,[2] these reactive iron minerals are expected to be most significant in redox transition zones. However, there are many challenges in collecting anaerobic cores representative of the subsurface environment and characterizing reactive iron mineral coatings with reduction-oxidation (redox) condition intact. To better understand iron mineral coatings as a function of redox potential in subsurface sediments from a site with historical contamination, this research focuses on using an 18-m Anaerobic Core collected with the redox conditions preserved throughout the entire process of obtaining the core, sampling, and laboratory analysis.[3] The purpose of this research is to characterize reactive iron mineral coatings in redox transition zones (RTZs) using analyses with resolutions from micro- to nanometers. This research is needed to better understand and quantify the abiotic processes in contaminated subsurface systems. With this understanding, mechanisms can be modeled and potentially enhanced to improve natural attenuation processes. Unique mineralogy and morphologies of reactive iron mineral coatings are being observed in RTZs using complementary tools for characterization.

This study helps support a methodology for collecting, preserving, and analyzing complete sediment cores representative of the subsurface. Once the redox condition is preserved, signature coatings formed through abiotic and biotic degradation pathways can be characterized. In addition, this research provides a solid foundation for refining the

conceptual site model with respect to biogeochemical processes, which can be applied to better estimate the mobility, transformation, and natural attenuation of contaminants of concern (COCs). These results can be used to optimize the geochemical environment in groundwater systems to enhance remediation with abiotic reactions.

In addition, iron mineral coatings found in the anaerobic core were compared with a cryogenic core which is referred to as Cryo Core. The two most important iron sulfide "precursors" of pyrite, mackinawite, and greigite, were not found in the Cryo Core but were ubiquitous in RTZs of the (unquenched) Anaerobic Core. By conducting a cryogenic quench study at 77 K on split samples from the Anaerobic Core, poorly crystalline iron sulfide, mackinawite, was observed to decrease while pyrite increased. These unique phenomena can be explained by a mackinawite dissolution, transformation, and re-precipitation process during the freezing process driven by mechanisms of freezing-concentration and freeze potential in the cryogenic process. The results of the quench study also provide evidence that the cryogenic sampling technique for collecting sediment samples may result in a loss of mineralogy and morphology of metastable forms of iron sulfide coatings.

This dissertation includes a literature review on the importance of reactive iron minerals in contaminated subsurface systems, abiotic dehalogenation, and the pathways, as well as reactive iron mineral transformation in transition zones. The literature review is followed by the chapter on hypotheses and objectives. Details on materials and methods used in experiments are presented in Chapter 4. Critical results from different aspects in studying coring samples will be discussed in Chapters 5, 6, and 7. In the last chapter,

Chapter 8 presents conclusions and future work inspired by the current discoveries in this study.

CHAPTER 2

LITERATURE REVIEW

In this chapter, a literature review on the importance of reactive iron minerals is presented and followed by their role in abiotic remediation. Moreover, mechanisms responsible for abiotic dehalogenation of COCs are reviewed and the last section includes geochemical conditions and limitations impacting the transformation of reactive iron minerals.

2.1 Reactive Iron Minerals in Monitored Natural Attenuation

Based on the National Priorities List from the U.S. Environmental Protection Agency,[4] nonaqueous-phase liquids (NAPLs) have been abundantly observed over 60% of the sites. Because of their physical and chemical properties such as low solubility, high specific gravity, and tendency to sink in the subsurface, remediating NAPLs in soil and groundwater has been considered a particularly challenging problem.[5] The size and spatial distribution of the source zone are difficult to determine which limits the effectiveness of both conventional (e.g., groundwater pump-and-treat) and innovative (e.g., in situ chemical oxidation and bioremediation) technologies. As a result, less aggressive treatment of the dissolved phased by monitored natural attenuation (MNA) has been found to be useful in achieving long-term remediation in the subsurface.[6] MNA can be accomplished both biotically and abiotically as well as through volatilization.[7] In the biotic transformation of chlorinated solvents, primary mechanisms include halorespiration and cometabolism.[8, 9] In ecosystems, because it is an essential macronutrient for organisms, iron cycling is important some enzymatic reactions including photosynthesis, respiration, and nitrogen

fixation.[10, 11] Additionally, iron (III) oxyhydroxides in these reactions serve as electron acceptors.[12, 13] For abiotic transformation by reactive iron mineral coatings, important earlier work was addressed by Vogel et al.[14] They found halogenated contaminants such as trichloroacetic acid (TCA) and dichloroethene (DCE) in the groundwater can be transformed through abiotic reactions that included hydrogenolysis, dihalo-elimination (loss of two adjacent chlorines forming a C-C bond), and coupling (loss of chlorines on two separate molecules forming a C-C bond, joining the two molecules). Moreover, these processes were observed to be enhanced by catalysts such as clay.[15] In other studies,[16-18] researchers found that (a)biotic dehalogenation processes were observed in the presence of galvanized steel, stainless steel, aluminum, and iron. Gillham and co-workers[17] initially used iron powders (zero-valent iron, ZVI) as the electron source to remediate chlorinated methanes, ethanes, and ethenes in anaerobic columns. As a result, ZVI was applied as an critical component in PRBs to reduce perchloroethylene (PCE) and tricholoroethylene (TCE) in a pilot-scale field study conducted.[17, 19] The rate of degradation was modeled as pseudo-first-order and more restricted by reaction rate than mass transfer. Abiotic dehalogenation with reactive iron minerals came to the fore through the use of zero-valent iron as permeable reactive barriers (PRBs).[17, 20, 21] Although dehalogenation using ZVI was of focus in the early studies, related and recent work has extended to reactive iron minerals which likely had formed on the ZVI functioning as electron donors or reaction mediators to accelerate reductive dechlorination. Numerous studies have demonstrated the abiotic transformation of chlorinated solvents by mackinawite (FeS) under controlled anaerobic systems, which is including PCE,[22-24] TCE,[24, 25] cis-1,2-dichloroethene (cis-DCE),[26] carbon tetrachloride (CT),[27, 28] and chlorinated alkanes.[29, 30] Many other iron reactive minerals

have been studied including pyrite (FeS_2),[31, 32] green rust,[33] and magnetite.[27, 31, 34] In most of these studies, rate constants were measured and related to the mineral surface area; the trend describing the relative reactivity follows disordered mackinawite (FeS) > mackinawite > ZVI > pyrite (FeS_2) > sorbed Fe^{2+} > green rust (Fe(II)/(III) oxyhydroxide) = magnetite (Fe_3O_4) > biotite = vermiculite.[35] Moreover, with the growing interest in reactive iron minerals, many research groups[34, 36-40] are targeting how abiotic degradation can be practically enhanced in groundwater remediation both through engineered treatment and MNA. Ferrey et al.[34] used magnetite-bearing sediment to treat cis-DCE by natural attenuation; Kennedy et al.[41] injected ZVI with Epson salt ($MgSO_4 \cdot 7H_2O$) and sodium lactate ($NaC_3H_5O_3$) achieving 95% degradation of polychlorinated biphenyl, TCE, and cis-DCE in less than one year; and, recently there are a number of additional studies focused on using reactive iron minerals in abiotic dehalogenation.[36, 39, 42]

2.2 Mineral Coating Characterizing Techniques

To characterize reactive iron mineral coatings in sediments, SE has been initially used for quantitative analysis but are not amenable for evaluating mineralogy and morphological profiles in sediments.[34, 37, 40, 43-45] Jeong et al.[46] used Fe-K edge spectra from X-ray absorption spectroscopy to address the composition of iron minerals and their surface speciation that contributes to cis-DCE abiotic dechlorination. Han et al.[47] used X-ray diffraction (XRD) with X-ray photoelectron spectroscopy analyses to characterize green rust in the degradation of cis-DCE and vinyl chloride. Lee and Wilkin[48] applied SEM images to characterize surface coatings on soil samples from PRBs. Other tools applied have included X-ray fluorescence (XRF) for elemental concentrations,[34] as well as field-

emission scanning electron microscopy (FESEM) with energy dispersive X-ray analyzer (EDX) for morphology and surface elemental composition.[36, 38, 42] Because of the complexity of sediment, multiple techniques are necessary to characterize mineralogy, morphology, and composition as a function of the redox condition. While simulating three anaerobic systems to investigate the abiotic transformation of cis-DCE, Ferrey et al.[34] identified the presence of magnetite using a combination of XRF, acid digestion, and XRD. In another study, Whiting et al.[40] collected mulch samples from a biowall with abundant reactive iron mineral coatings. Chemical extraction revealed iron monosulfides and disulfides, while SEM and EDX were used for elemental composition and grain size analysis. Even though samples were preserved using liquid nitrogen that could potentially impact mineral morphology (at a minimum), results revealed the presence of iron sulfides. While difficult to distinguish, these minerals included potentially mackinawite, framboidal pyrite, pyrrhotite, and greigite.

2.3 Abiotic Degradation Mechanisms

Abiotic transformation of chlorinated solvents includes reductive elimination, hydrogenolysis, dehydrohalogenation, and hydrolysis. In this section, these mechanisms are reviewed. Abiotic degradation may include multiple mechanisms (Figure 2.1) that in many cases may also be achieved biotically.

2.3.1 Reductive Elimination

Reductive elimination, as a very important and common reaction for chlorinated solvent, occurs under methanogenic (anoxic) conditions as well as partially aerobic conditions.[49] Reductive elimination includes α-elimination and β-elimination, which involves the

elimination of chlorine atoms from the same one carbon atom and from two different carbon atoms, respectively. The reaction is observed in alkane transformation,[50] and can be described as follows:

$$RCCl\text{-}CClR + 2e^- \rightarrow RC{=}CR + 2Cl^- \tag{2.1}$$
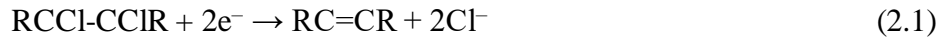
Reductive elimination has been observed in the transformation of TCE to acetylene via the intermediate chloroacetylene;[51, 52] and acetylene may then convert to ethene or/and ethane through hydrogenation that may be a function of pH and oxidation reduction potential (ORP).[53, 54]
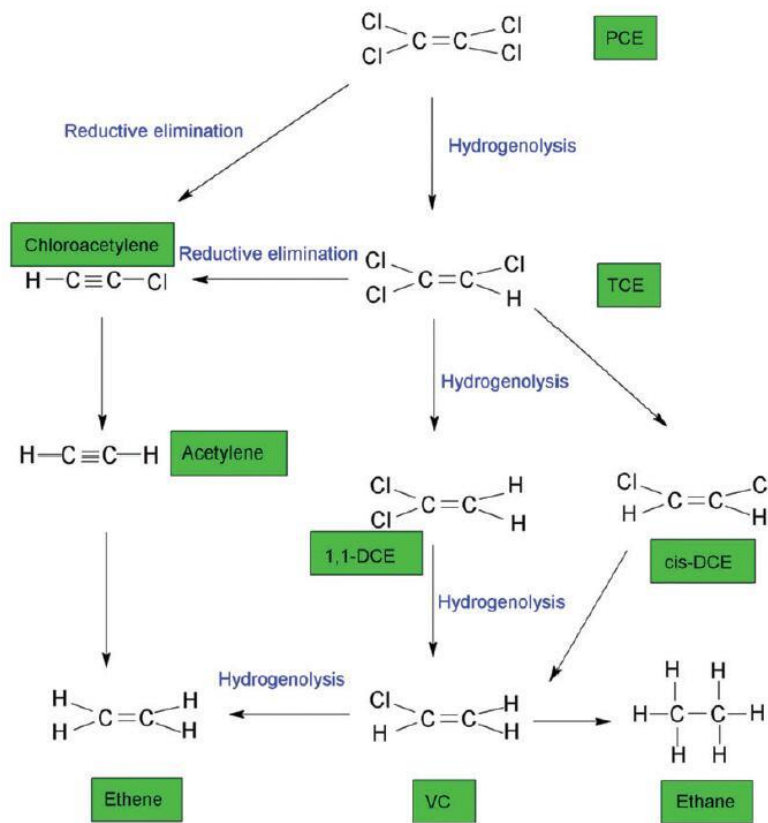
Figure 2.1 PCE degradation includes multiple mechanisms in natural attenuation.
Source: He, Y.; Wilson, J.; Su, C.; Wilkin, R., Review of abiotic degradation of chlorinated solvents by reactive iron minerals in aquifers. *Groundwater Monitoring & Remediation* **2015,** *35*, (3), 57-75.

2.3.2 Hydrogenolysis

Hydrogenolysis is a reductive reaction where a carbon-chlorine bond is broken, and hydrogen replaces chlorine. Simultaneously, two electrons are transferred to the molecule from the electron donor (reductant).[55, 56] The reaction can be described as follows:

$$RCl + H^+ + 2e^- \rightarrow RH + Cl^- \tag{2.2}$$

Chlorinated ethenes and ethanes can be transformed through the hydrogenolysis process in both biotic and abiotic systems.[51] Butler and Hayes[25] reported TCE underwent sequential hydrogenolysis forming cis-DCE, followed by vinyl chloride, and then ethene in the presence of iron sulfides and ZVI.

2.3.3 Dehydrohalogenation

In dehydrohalogenation reaction, chlorinated alkanes lose a chlorine atom from a carbon atom dropping the hydrogen atom from an adjacent carbon atom and forming an unsaturated double bond:[51]

$$RHCCl\text{-}CRH_2 \rightarrow RHC=CHR + HCl \tag{2.3}$$

At pH ranging from extreme basic to neutral, this reaction has been observed in the transformation of 1,1,2,2-tetrachloroethane, 1,1-dichloroethane, and 1,1,2-TCA.[14, 57]

2.3.4 Hydrolysis

Hydrolysis is a substitution reaction where chlorinated solvents react with water, in which the chlorine atom is replaced by a hydroxyl group:

$$RCl + H_2O \rightarrow ROH + HCl \tag{2.4}$$

The products of hydrolysis can be alcohols and alkenes. Studies [14] have shown that the more chlorinated a compound is, the less likely to be hydrolyzed. This reaction is important

in the transformation of 1,1,1-TCA to acetic acid;[51, 52] and it can also be found in the dechlorination of halomethanes.[53, 54]

2.4 Reactive Iron Minerals in Transition Zones

In natural attenuation, reactive iron minerals precipitate in iron cycling between its ferrous and ferric oxidation states through both abiotic and biotic reactions. Iron cycling (Figure 2.2) includes several processes: microbial Fe^{2+} oxidation; abiotic Fe^{2+} oxidation by inorganic substrates; abiotic Fe^{2+} oxidation by organic substrates; Fe^{2+} sorption on inorganic and organic surfaces; biological Fe^{3+} reduction; abiotic Fe^{3+} reduction by inorganic substrates; and, abiotic Fe^{3+} reduction by organic substrates.[58] Precipitation of iron sulfides is affected by redox conditions and concentrations of sulfide in groundwater.[2] The source of iron and sulfur plays an important role in iron cycling. The most common source of dissolved Fe^{2+} is through the reduction of ferric oxyhydroxides.[59, 60] On the other hand, a major source of sulfide is through biotic reduction of sulfate. Under anaerobic conditions, H_2S can be generated from the sulfate reducing bacteria. In the process of iron sulfide precipitation, disordered metastable mackinawite precipitates.[2, 61] Subsequently, mackinawite may be transformed to pyrite through three pathways include in the following (Figure 2.3): (1) FeS reacts with S^0, polysulfides, or other S intermediates to form FeS_2; (2) FeS transforms into FeS_2 through greigite as intermediate; and, (3) FeS_2 is formed via the H_2S oxidation. He et al.[1] summarized the primary factors limiting the formation of iron sulfide minerals: the concentration and reactivity of iron compounds, the availability of dissolved sulfate, and the concentration of organic carbon that acts as a carbon source for
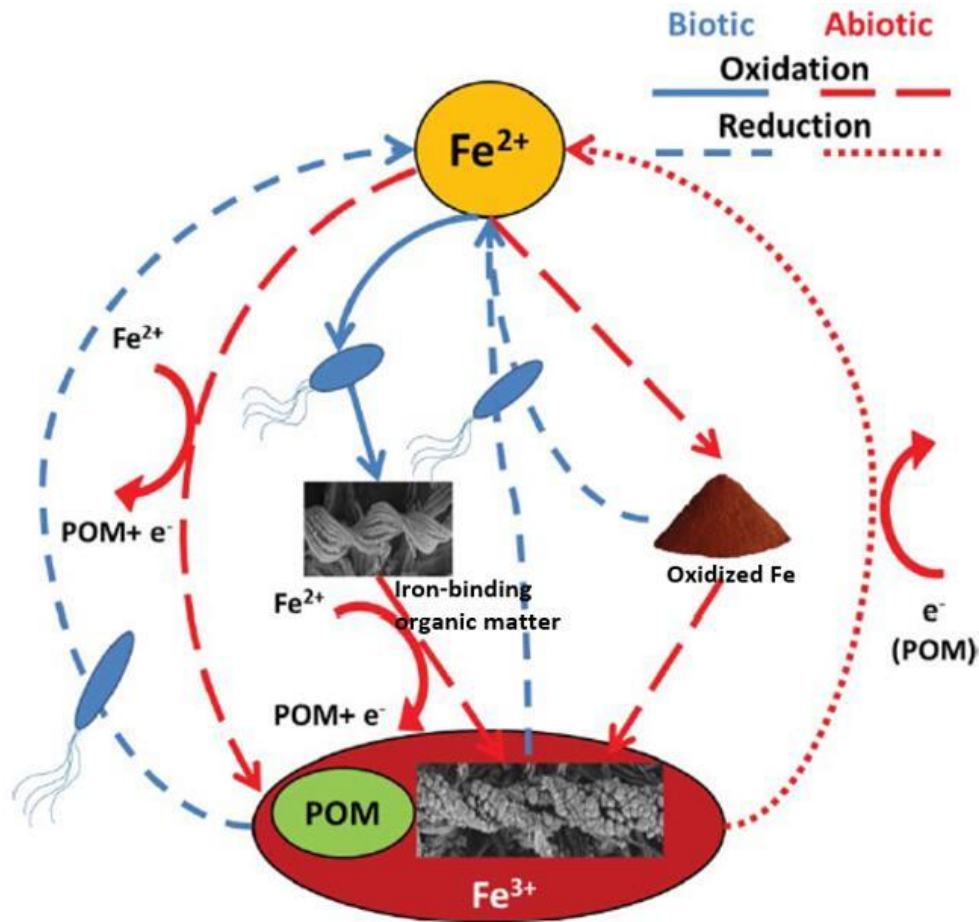
Figure 2.2 Concept of iron cycling through redox reactions in a natural system (POM: particulate organic matter).[58, 62]

Source: Ionescu, D.; Heim, C.; Polerecky, L.; Thiel, V.; De Beer, D., Biotic and abiotic oxidation and reduction of iron at circumneutral pH are inseparable processes under natural conditions. *Geomicrobiol. J.* **2015,** *32*, (3-4), 221-230.

sulfate-reducing bacteria to produce sulfide. In natural systems, the concentration of reactive organic carbon becomes the most common limiting factor in bacterial sulfate reduction. When sulfide is abundant, iron sulfide precipitation is limited by the source of reactive iron minerals.
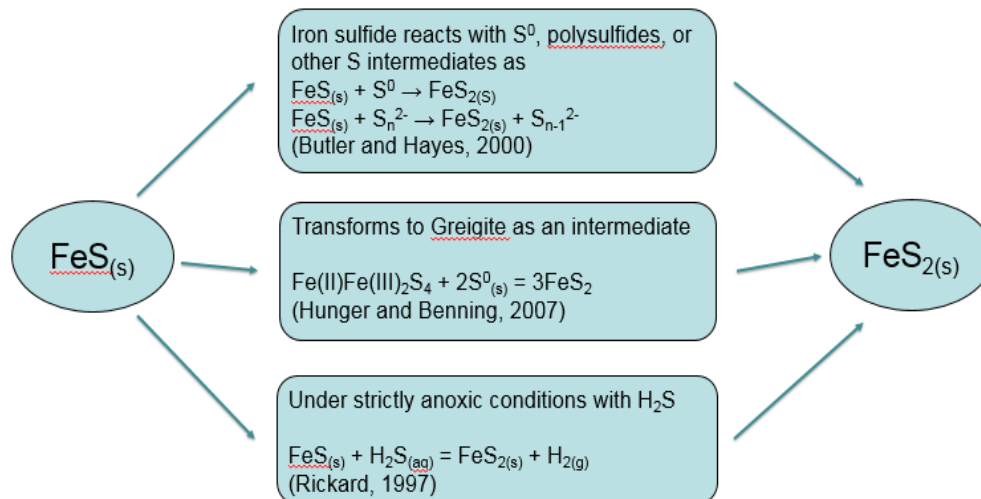
Figure 2.3 Possible formation pathways from mackinawite (FeS) to pyrite (FeS_2).
Source: Butler, E. C.; Hayes, K. F., Kinetics of the Transformation of Halogenated Aliphatic Compounds by Iron Sulfide. *Environ. Sci. Technol.* **2000,** *34 (3)*, 422–429.
Hunger, S.; Benning, L. G., Greigite: a true intermediate on the polysulfide pathway to pyrite. *Geochem. Trans.* **2007,** *8*, (1), 1.
Rickard, D.; Luther, G. W., Kinetics of pyrite formation by the H_2S oxidation of iron (II) monosulfide in aqueous solutions between 25 and 125°C: The mechanism. *Geochim. Cosmochim. Acta* **1997,** *61*, (1), 135-147.

In RTZs, iron cycling results in a continuous process of precipitation and dissolution both biotically and abiotically.[2, 63, 64] Although the transition regime of interest can be in the range of millimeters-to-decimeters (or more) in spatial scales,[65] attempts to characterize iron reactive mineral coatings in RTZs have resulted in limited success.[1] A significant issue in studying these systems is collecting sediment samples representative of the in situ redox potential. Additionally, both the process of collecting a core and its subsequent transport for laboratory analyses are prone to negatively impacting the redox conditions, which affect the reactive iron mineral coatings. Ferrey et al.[34] and Darlington et al.[39] attempted to reduce exposure to the atmosphere after collection. However, they autoclaved samples in their studies, thereby impacting surface chemistry and mineral coatings. Collecting samples in a water column without headspace may be an option;[37] but oxygen diffusion through sample containers including borosilicate glass may impact the

redox condition. Although another method to possibly slow down the transformation process involved freezing samples.[40, 42] the freezing and thawing process itself may potentially change the mineralogy of surface coatings and the rate of transformation is not clearly understood.[66, 67] Furthermore, analyses applied to these samples still need to resolve the relatively low concentrations of the mineral coatings present in a complex matrix where the redox condition is preserved. As a result, numerous studies have focused on lab-synthesized reactive iron minerals.

2.5 Summary of Literature

The literature reviewed in this chapter included studies on the reductive transformation of a variety of halogenated organic compounds by using reactive iron minerals. To evaluate the efficiency of potential abiotic degradation, multiple techniques may be applied for characterizing these mineral coatings. Four dehalogenation processes that are potentially responsible for the transformation of contaminants include reductive elimination, hydrogenolysis, dehydrohalogenation, and hydrolysis. As an important source of reactive iron minerals in subsurface systems, iron cycling is strongly affected by the redox transformation in the subsurface environment. These RTZs are expected to be significant for iron sulfide mineral precipitation and COC dehalogenation. In the following chapter, the research objectives and hypotheses are presented.

CHAPTER 3

RESEARCH OBJECTIVES AND HYPOTHESES

Research objectives are included in the following:

- Study an 18-m Anaerobic Core collected with the redox potential preserved from a contaminated industrial site. A set of geochemistry screening analyses is employed for identifying RTZs: sediment pH, sediment ORP, solid phase elemental concentrations, O_2 and volatile organic compound (VOC) concentrations in the sample head space.

- Develop a protocol and methodology to characterize reactive iron mineral coatings in RTZs.

- Evaluate the change in the surface coating mineralogy as a function of depth in RTZs XRD and FESEM/EDX to assist in resolving surface chemistry, mineralogy, and morphology at the micro- and nano-meter scale.

- Develop models of natural attenuation of COCs by iron mineral coatings in RTZs.

Specific hypotheses being tested in this research include:

- Abiotic and biotic reactions that play an important role in contaminant transformation occur at/very near the mineral-water interface.

- Surface reactivity of interest is most significant in RTZs.

- The speciation and morphology of precipitates forming on the surface of bulk mineral phases control the desired (a)biotic reactions and are a signature of the biogeochemical processes that are active.

CHAPTER 4

MATERIALS AND METHODS

This chapter reviews the methodology used to obtain an Anaerobic Core from an industrial site with historic contamination. The chapter continues with the process for storing the core, collecting subsamples from this core, and studying the reactive iron mineral coatings found in RTZs.

4.1 Study Site Description

The study site had a long history of chemical processing and subsurface contamination. Geologically, there is approximately 150 m of unconsolidated Coastal Plain sediment deposited during the Holocene Epoch, Pleistocene (Quaternary period) Epoch, and Cretaceous Period. Igneous and metamorphic rocks of the Wilmington Complex unconformably underlie the Coastal Plain sediment. These Pleistocene sediments are fluvial, estuarine, and marginal marine in origin. With a site history of industrial operation in producing such products as aromatic chemicals and elastomeric polymers, NAPLs were discovered in the subsurface migrating to deeper sandy aquifers. Although pump-and-treat is in place for containing contaminant migration off-site, COCs such as (di-)chlorobenzene, are still detected at relatively high concentrations. Other contaminants include aniline, benzene, chloroform, nitrobenzene, tetrachloroethylene (PCE), trichlorofluoromethane based on groundwater samples collected from adjacent coring location.

4.2 Sampling, Transportation, and Preservation

The Anaerobic Core was collected in the Detailed Study Area using a 10.2-cm (4-in) diameter by 3-m (10-ft) long hybrid Vibracore core barrel with a Rotosonic drill rig. Following the on-site sample collection protocol, twenty-seven 0.6-m (2-ft) steel-lined sediment cores with stainless steel disks secured at the ends were vertically loaded and sealed in argon-purged PVC tubes; the cores were transported to New Jersey Institute of Technology for further sampling and geochemical analyses. This procedure has been referred to as Biogeochemical Coring and Preservation Methods described by Richard Landis.[3]

The cores were jacked into 5-cm (2-inch) subsamples in an oxygen controlled (< 0.1 ppm O_2 concentration at steady state) glovebox with 99.999% N_2 and a copper catalyst to trap O_2. Each 5-cm subsample was preserved through a triple-layer containment system to prevent oxygen diffusion and chemical corrosion from VOCs in the sediment. Sediment samples were loaded into DURAN® borosilicate glass containers capped with aluminum foil and polytetrafluoroethylene-film-lined lids. Containers were placed in Mylar bags heat-sealed with oxygen indicators and absorbers, and then loaded into high-density polyethylene Nalgene™ jars for handling. A total of 225 5-cm subsamples were preserved at 4 °C to minimize the effect of transformation processes.

4.3 Screening Analyses and Transition Zone Identification

RTZs were determined based on the previous screening study by Yin et al.[68] that included elemental composition using XRF (Niton™ XL3t GOLDD+ XRF Analyzer with built-in soil and mine models) with EPA Method 6200,[69, 70] sediment pH,[71, 72] sediment ORP,[73]

VOC concentration in the sample headspace with a photoionization detector (MiniRAE 3000 Photoionization Detector with 11.7 eV Lamp),[74] and abundant bacteria. The sediment pH and ORP were measured with an Orion Star A211 Benchtop Meter (Thermo Scientific). Five grams of samples were collected from every subsample and sediment pH was measured with a calibrated probe (8302BNUMD, Thermo Scientific) after mixing 0.01 M $CaCl_2$ solution with the sediment to liquid ratio of 1:3 (w/v) under room temperature.[75] Sediment ORP measurements were collected with a sediment/deionized (DI) water ratio of 1:4 (w/v) with an ORP probe (9179BN, Thermo Scientific).[73]

The microbial community was analyzed by amplification of the 16S rRNA gene V4 region using primers described previously,[76] sequencing DNA from each subsample to a read depth of greater than 50,000 reads. Sequences were then error corrected, and subject to de novo operational taxonomic unit (OTU) clustering. The relative abundance of each OTU was determined in each sample (Figure 4.1), and the Mothur analysis pipeline[77] was used to generate genus level taxonomic assignment of the OTUs.

The gradients of key parameters including Fe, S, and ORP along with the microbial data provided important evidence for RTZs. Five transition zones are identified along with geological layers as follows (Figure 4.1):

- Upper Zone (depth below the surface (DBS) from 4 to 4.6 m; B-Aquifer)

- Zone 1 (DBS from 6.4 to 7 m; interface of B-C Clay and C-Aquifer)

- Zone 2 (DBS from 9.5 to 10.7 m; interface of C-Aquifer and D-Aquifer)

- Zone 3 (DBS from 14.6 to 15.3 m; interface of D-Aquifer to D-E Clay)

- Lower Zone (DBS from 19 to 20.1 m; D-E Clay)
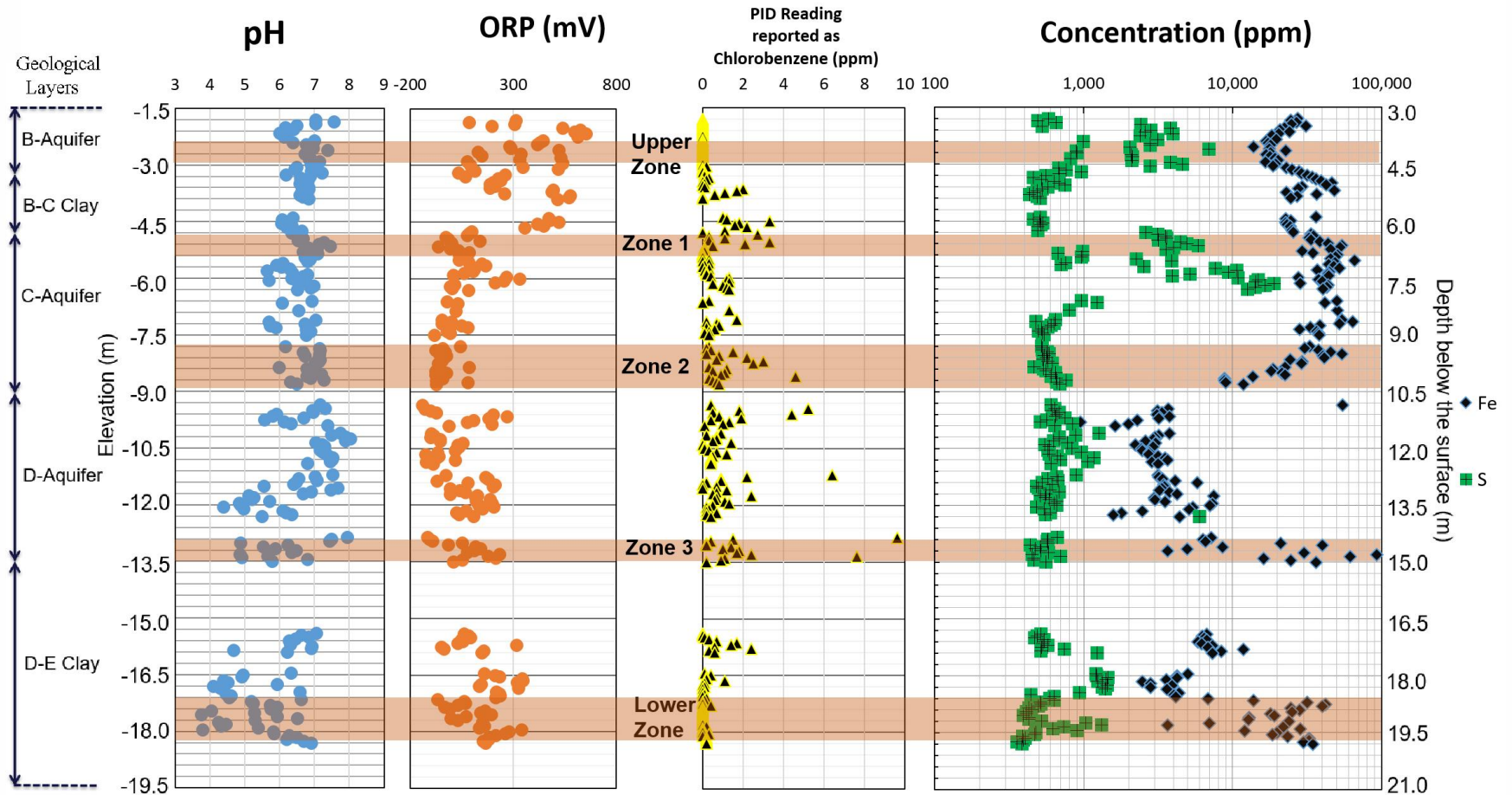
Figure 4.1 Locations of five transition zones along with screening data.

4.4 Water Chemistry

Subsurface hydrogeologic and water chemistry data were collected by a Waterloo Multi-Level System (MLS) which was previously installed in the same area adjacent to the location of the sediment core. Data used in this study are from samples collected from 13 individual sampling ports at depths between 1.7 and 18.1 m depth below the surface (DBS), and analyzed following U.S. Environmental Protection Agency (EPA) standard methods (e.g., Method 150.2, 353.2, 300.0, 6010B, and 6260B). The MLS data include nitrite, pH, dissolved oxygen, chloride, Fe^{2+}, dissolved sulfate, and COCs.

4.5 Sequential Extraction

Sequential extraction (SE) was applied to help quantitatively analyze surface mineral coatings in RTZs as reported in an earlier study.[78] The procedure of SE (Table 4.1) was conducted in the glovebox and involves six steps for isolating Fe phases. The concentration of iron extracted from each phase was measured for each 5-cm subsample from the RTZs with total Fe based on XRF elemental analysis.[78] In each step, an extract of 10 ml was centrifuged and diluted for Fe concentration measurement by atomic absorption or inductively coupled plasma mass spectrometry. The sample residue was rinsed with deionized water between each step of the SE process.

4.6 XRD Analysis

XRD analysis is widely used in mineral identification using search and match tools with standard mineral patterns based on the International Centre for Diffraction Data (ICDD)

Table 4.1 Six-step Sequential Extraction for Iron Phases in Sediment

Step	Targeted iron species	Extractant	Extract volume (ml)	Adapted Time	Reference
1	Ion exchangeable Fe	1 M MgCl$_2$, pH 7	10	3 h	[45, 79]
2	Carbonate Fe: Siderite	1 M NaAc, pH 4.5	10	40 h	[45]
3	Poorly crystalline: (the recovery from standard mineral of Calff's study: Ferrihydrite (98%), Schwertmannite (>98%), Jarosite (65%), Hematite (30%), Magnetite (9%)	1 M HCl	10	11 h	[80, 81]
4	Reducible oxides: Goethite, Akaganeite, Hematite	50 g/L sodium dithionite buffer to pH 4.8 with 0.35 M acetic acid/0.2 M sodium citrate solution	10	7 h	[45]
5	Magnetite	0.2 M Ammonium oxalate buffer to pH 3.2 with 0.17 M oxalic acid solution	10	6 h	[45]
6	Targets Pyrite (>98%)	15.9 M HNO$_3$	10	4 h	[82]

and Inorganic Crystal Structure Database (ICSD) Databases. In this study, two subsamples were collected from each 5-cm sample for XRD analysis (with Philips, EMPYREAN system, and Cu K-α radiation source at 45 kV and 40 mA). Sediment samples were mounted in holders sealed with 1 mil of Kapton film to prevent oxygen diffusion during the 23-minute scans. Each sample was scanned from 10 to 100º 2θ with 0.026 º step size at 100 s per step using a 255-active-channel detector. The interpretation was based on the ICDD and ICSD Databases along with the XRF data on bulk elemental composition. A semi-quantitative analysis provided estimated mass fractions of the accepted phases. The scale factor and the reference intensity ratios (RIR) (also known as I/I_c values) were used to perform the calculation (1% by wt. detection limit).[83] A scoring system (0 - 100%) showed the goodness of fit between reference pattern lines and the scan/peak features. The identification and semi-quantification programs were performed using PANalytical's HighScore plus (ver. 3.0.5) software. For the purpose of identifying and tracking the changes in critical peaks, all diffractograms were scaled based on the quartz (SiO_2) standard intensity and peak location (Appendix A). This adjustment involved a potential shift in the pattern along the X-axis caused by small variations in the distance between the sample surfaces to the X-ray source.

XRD semi-quantitative analysis for both bulk and mineral coatings involved what is referred to as a "100% approach" which is based on the mineral RIRs and scale factors that assume all detected phases make up 100% of the minerals present. This approach is based on two assumptions: (1) the orientation in the samples is uniform for all mineral phases in a mixture, and (2) the RIRs should be the same for all particles of one phase regardless of the natural heterogeneity of these mineral coatings in soils.[84] The semi-

quantification of mineral coatings was limited to iron-related minerals. Water content potentially decreases the peak intensity, the full-width at half-maximum (FWHM) of the peak, and even slightly shifts the peak location depending on the orientation of the mineral lattice.[85]

The accuracy of XRD analysis has been demonstrated to be limited when quantifying mineral coatings at concentrations less than approximately 1 to 5% by weight.[1] Two issues confounded the diffractogram interpretation. First, the signal from quartz is significantly greater than other minerals and diminishes the signal from both (other) bulk and mineral coatings. In this research, to assist in the identification, elemental compositions according to XRF results were applied to constrain the potential mineral candidates especially for mineral coatings. Increasing the scanning time helped in distinguishing some of the weaker peaks; however, the scanning time was limited by the rate of oxygen diffusion through the Kapton film. Second, feature peaks of mineral coatings and clay minerals were potentially indistinguishable because of stronger intensities from the bulk mineral peaks or the broad peaks (from 13 to 18º 2θ in XRD diffractograms) from amorphous minerals. To diminish potential interferences from sediment water content, Mylar film, limited scanning time, and overwhelming signals from bulk as well as amorphous clay minerals, techniques applied included multiple scanning channels, XRF elemental restriction, and a scoring system were applied; as a result, the accuracy and efficiency of the analyses of reactive iron coatings were enhanced.

4.7 FESEM/EDX Analysis

FESEM/EDX analysis can provide high-resolution images of the morphology of reactive mineral coatings on bulk mineral surfaces from micrometer to nanometer scales with surface elemental mapping and identification assessed with EDX. A LEO 1530 FESEM equipped with EDX (Inca series 200) was applied in this study. Before the analyses, samples were transferred (Quorum EMS 150T ES) into a nitrogen-purged glove bag ($O_2 <$ 1%) and coated with Au/Pd metal layer (between 5 and 10 nm) to preserve the redox condition and improve the conductivity of the sample surface. FESEM analysis began with low magnification: (1) Evaluate grain size; (2) Select four to five random locations to conduct EDX mapping at a working distance of 6 mm and magnification of 1500×. Locations with elevated Fe and/or S concentrations were further probed at high magnification with nanoscale FESEM images of morphology and composition. Mineral identification was based on morphology, element composition, and atomic ratio; this surface coating mineralogy was resolved and corroborated with XRD.

CHAPTER 5

CHARACTERIZING REACTIVE IRON MINERAL COATINGS
IN REDOX TRANSITION ZONES

Analytical results from XRD and FESEM/EDX are discussed in this chapter and focus on the reactive iron mineral coatings observed in the Upper Zone (DBS from 4 to 4.6 m) and the Zone 1 (DBS from 6.4 to 7 m). The unique morphology of mineral coatings are highlighted in the figures suggesting transformation pathways and geochemical environments specific to the transition zone studied.

5.1 XRD Diffractograms

The XRD diffractograms from the Upper Zone and Zone 1 reveal a broad peak between 13 and 18º 2θ in most samples indicating the presence of amorphous minerals. The three dominant bulk minerals observed in most samples include quartz, clinochlore, and muscovite with the main peaks at 27º 2θ (3.3 Å) for quartz (used to correct the shift), 12º 2θ (7.2 Å) for clinochlore, and 25º 2θ (3.5 Å) and 28º 2θ (3.2 Å) for muscovite. Zone 1 located in an aquitard-aquifer transition zone is distinguished from the Upper Zone by a higher concentration of clay minerals, muscovite and clinochlore (Figure 5.1). On the other hand, albite and anorthite from the feldspar group were also detected as primary minerals in the Upper Zone. Additionally, zeolite minerals were found to be possible candidates based on remaining XRD peaks, which potentially transformed from aluminosilicate precursor minerals [86] of the feldspar group and other bulk minerals detected.

The signal intensity from mineral coatings was much weaker than from bulk minerals, but stronger than the background. To narrow the scope of potential mineral coatings of interest, the analysis was constrained to minerals composed of elements that were abundant based on XRF and included Si, Fe, Al, Ti, S, and P. Compared to the weaker signal from poorly crystalline and amorphous iron mineral coatings such as mackinawite, greigite, and ferrihydrite, crystalline coatings such as magnetite, siderite, pyrite, goethite, and lepidocrocite were generally more clearly detected. In the Upper Zone, located in a shallow aquifer layer, Fe(III) mineral coatings dominated over the Fe(II) and Fe(II)/(III) minerals in most samples. Fe(II) minerals such as mackinawite and pyrite were observed in samples less rich in Fe(III) minerals and from a more reduced environment overall (Figure 5.1). The redox shift occurred at the bottom of the Upper Zone where reduced iron mineral concentrations increased with a corresponding decrease in the Fe(III) fraction. Given the complex nature of the sediment, the redox potential measured in the sediment samples likely represents a nonequilibrium condition.[68] Within Zone 1 which is abundant in clay minerals, a greater fraction of total iron mineral coatings was found as compared to the Upper Zone; this result is consistent with the concentrations of Fe and S measured in the screening with XRF.[68] Furthermore, Fe(II)/(III) minerals were found to a greater degree in Zone 1 versus the Upper Zone. Although reduced conditions were dominant throughout Zone 1, Fe(III) minerals were observed and peaked in the deepest samples at a DBS of 6.65 to 6.76 m. Samples with lower S concentrations were found in the shallowest and deeper portions of Zone 1, where siderite may be a more abundant reduced iron mineral coating. Pyrrhotite was also found in most samples throughout this zone;
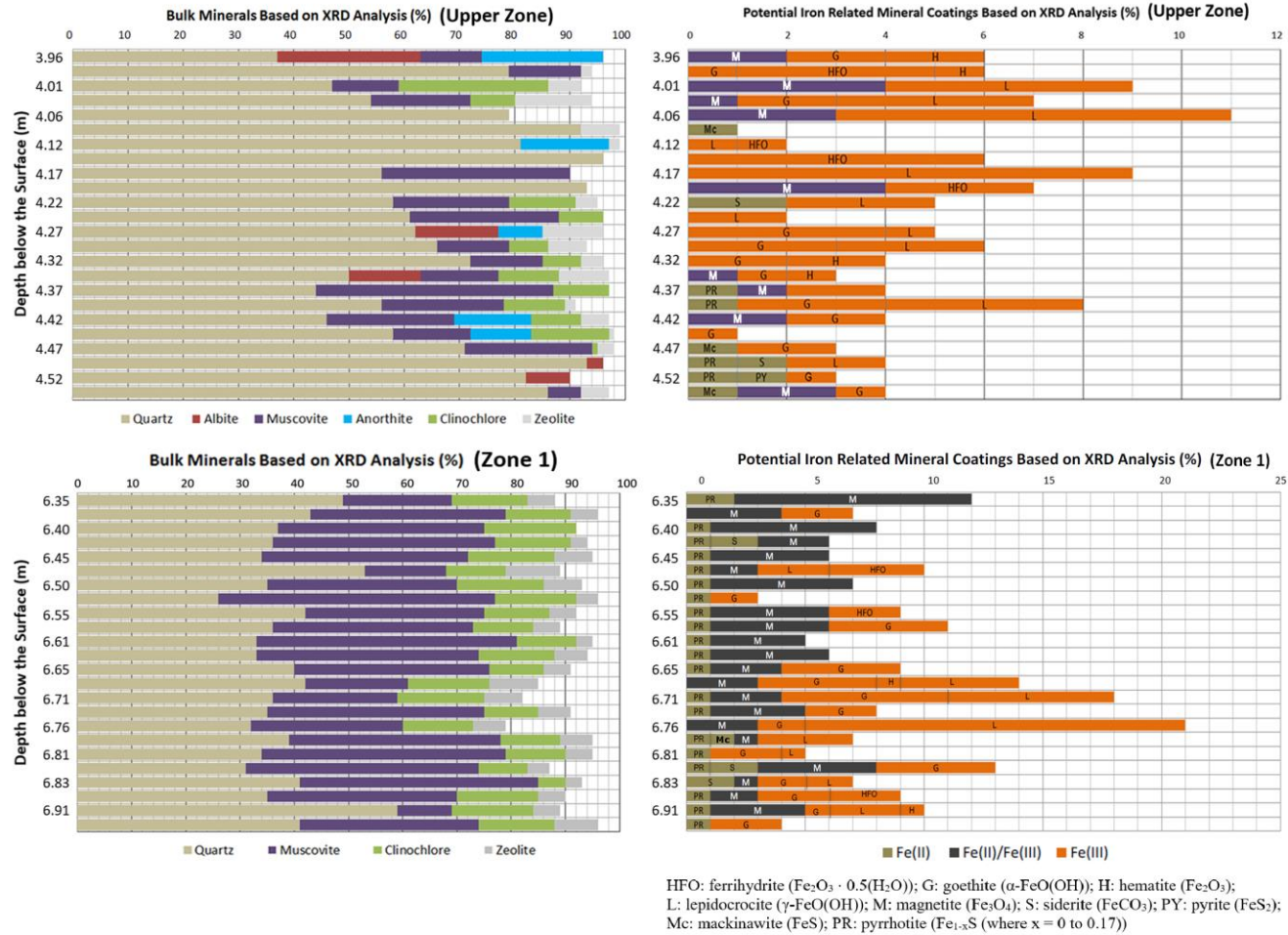
Figure 5.1: XRD identification and semi-quantification results for bulk minerals as well as iron related mineral coatings in the Upper Zone (DBS from 4 to 4.6 m) and Zone 1 (DBS from 6.4 to 7 m).

although the main peaks are more difficult to detect given the greater signal (the broad peak) from amorphous minerals that overlapped the pyrrhotite peaks. As a result, the presence of pyrrhotite cannot be distinguished by XRD alone and requires other tools such as SE and FESEM/EDX.

5.2 FESEM/EDX Analyses

The Upper Zone is the shallowest RTZ at a DBS of 4 to 4.6 m and located in a shallow aquifer layer. The most abundant aggregates of iron sulfide minerals in this zone were observed in clay lenses at a DBS of 4.27 to 4.42 m. Mineral coating morphology in these clay layers (Figure 5.2A and B) is unique, revealing subspherical framboids composed of cubic to octahedral microcrystals with individual grains ranging from 200 nm to 1 μm. EDX identification reveals Fe/S atomic ratios of 0.62 and 0.72, consistent with greigite (Fe_3S_4) having a Fe/S ratio between that for mackinawite (FeS) and pyrite (FeS_2). Greater than 50% of the iron-sulfide mineral coatings found were in the form of framboidal greigite throughout this zone. Interestingly, framboidal pyrite (Figure 5.2C) was found abutting greigite framboids (Figure 5.2D) revealing a potential transformation pathway.[87] Other identified mineral coatings included mackinawite and gypsum ($CaSO_4 \cdot 2H_2O$) (Figure 5.2F).

Zone 1, a RTZ deeper than the Upper Zone, is located at a DBS of 6.35 to 6.96 m; the zone is dominated by an aquitard (that transitions to an aquifer) abundant in sulfide-rich coatings (Figures 5.3A, B, and C). However, in contrast with the Upper Zone, granular pyrite (Figure 5.3A) with a larger grain size (of approximately 3 μm)
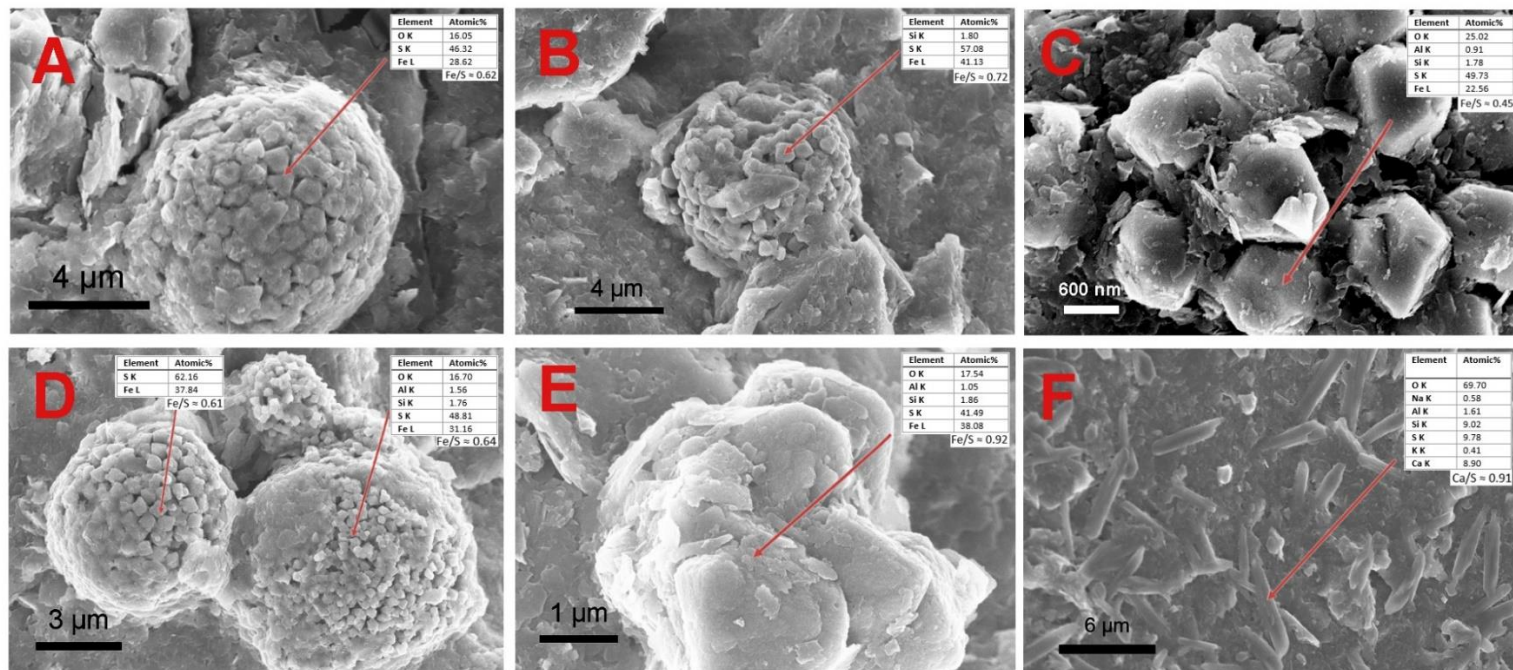
Figure 5.2: Mineral coatings observed in the Upper Zone by FESEM. A and B: framboidal greigite; C: framboidal pyrite; D: spherical framboids of greigite, and some greigite on the left framboid are transforming into pyrite; E: mackinawite is developing cubic structures; and F: Gypsum.
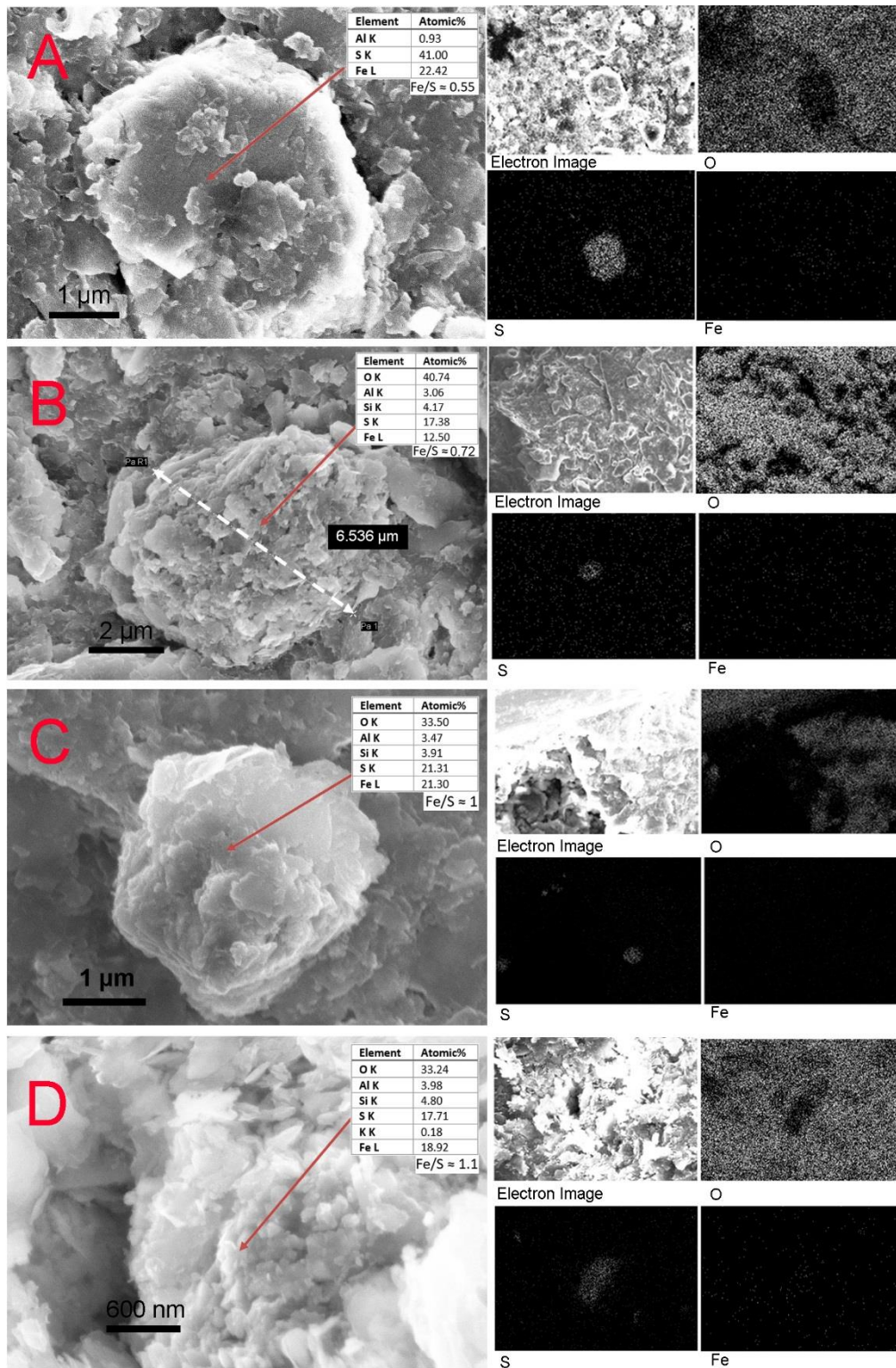
Figure 1.3: Mineral coatings observed in Zone 1 by FESEM along with EDX mapping of O, S and Fe. A: pyrite; B and C: potential pyrrhotite with subpentagonal morphology; and D: flaky aggregates of mackinawite.

than the pyrite grains in the framboidal structures was observed. Additionally, iron sulfide grains of pyrrhotite were found in a pentagonal structure with Fe/S ratios of 0.72 and 1 (Figure 5.3B and C, respectively). Pyrrhotite was observed as a more crystalline structure in contrast to mackinawite (Fe/S ratio of 1) (Figure 5.3D); the Fe/S ratio is consistent with the stoichiometry of pyrrhotite ($Fe_{1-x}S$ (where x = 0 to 0.17)).

FESEM/EDX was effective in identifying and characterizing aggregated iron- and/or sulfide-rich mineral coatings. However, this approach requires that mineral coatings be elementally recognizable from the bulk mineral surface at micrometer (µm) resolution during the elemental mapping phase. For this reason, when iron oxyhydroxides precipitate without aggregating on the surface, the minerals may not be as distinguishable during elemental mapping. In general, locations rich in iron sulfide mineral coatings were found to be present to a greater degree in Zone 1 as compared to the Upper Zone. This observation is consistent with the elemental concentrations of Fe and S in sediment based on XRF screening.[68] Iron sulfide mineral coatings revealed atomic Fe/S ratios between 0.4 and 1.4.

5.3 Iron Coating Sulfidation and Precipitation

To better understand MNA processes in the subsurface systems, contributions from the ferrous sulfides coatings need to be addressed as these mineral surfaces are important indicators of on-going biogeochemical reactions in RTZs. Among the reactive iron mineral coatings, mackinawite (FeS) has been reported as one of the most reactive minerals in abiotic dehalogenation processes given its large surface area and reaction rate of constants determined in lab studies.[35] However, the presence of mackinawite in natural sediment systems are rarely reported because of its sensitivity to oxygen and other oxidizers. In our

XRD analysis, mackinawite was detected as a small broad peak at 5 Å (17.7º 2θ) in diffractograms representing the distance between the tetragonal layers with each Fe atom bonded to four sulfur atoms; the iron sheets are stacked and interact by van der Waals forces.[88] This peak is also reported to be broadened or almost undetectable in other earlier studies because of its high sensitivity to residual oxygen during analyses.[2] Using FESEM/EDX, the observed Fe/S ratios of mackinawite are relatively close to one; consistent with other reports of 0.99 ± 0.02.[89] Because of its nanoparticle grain size, elemental mapping revealed locations of elevated S concentrations with no well-defined boundaries on the bulk mineral surface (Figure 5.3D).

Pyrite, a thermodynamically stable form of iron sulfide found in sediments with little to no oxygen, has a crystalline NaCl-type structure with Fe(II) atoms in octahedral coordination with disulfide making up the FeS_2 stoichiometry. Pyrite is more readily observed with XRD than other iron sulfide minerals. Despite differences in grain size and packing structure, pyrite was observed in both the Upper Zone and Zone 1 with XRD (Figure 5.1), EDX mapping, and FESEM/EDX identification (Figure 5.3A). Two unique morphologies were found, framboidal and granular (also known as euhedral), in the transition area from the aquifer with clay lenses and an aquitard, indicating unique transformation pathways.[90]

Pyrite, a thermodynamically stable form of iron sulfide found in sediments with little to no oxygen, has a crystalline NaCl-type structure with Fe(II) atoms in octahedral coordination with disulfide making up the FeS_2 stoichiometry. Pyrite is more readily observed with XRD than other iron sulfide minerals. Despite differences in grain size and packing structure, pyrite was observed in both the Upper Zone and Zone 1 with XRD

(Figure 5.1), EDX mapping, and FESEM/EDX identification (Figure 5.3A). Two unique morphologies were found, framboidal and granular (also known as euhedral), in the transition area from the aquifer with clay lenses and an aquitard, indicating unique transformation pathways.[90]

The presence of greigite surface coatings is another iron sulfide mineral indicative of specific transformation processes.[87] The Fe(II) and sulfide atoms in the greigite structure theoretically can function as electron donors during abiotic dehalogenation; however, it's role with chlorinated solvents has not been reported. Although not measured directly, a comparison of abiotic degradation rates in bench-scale studies with mackinawite, pyrite, and iron oxides[27, 66] suggests that greigite, a thermodynamically metastable phase, is potentially more reactive than stable phases such as pyrite and magnetite. In the anaerobic cores, greigite framboids were observed in shallow aquifer layers only (the Upper Zone) by FESEM/EDX. In XRD analysis, isolating the greigite signal in the presence of mackinawite is difficult as both are structurally cubic, close-packed arrays of S atoms linked by smaller Fe atoms sharing the structural arrangement of (001).[91, 92] In FESEM images, greigite shows spherical or sub-spherical packs of small cubic or octahedron particles (Figure 5.2A, B, and D). Greigite does not precipitate directly from solution, but instead transforms from mackinawite via an oxidation process,[93] eventually converting to pyrite via the following reaction pathway:[94]

$$3FeS + S_{0(s)} \rightarrow Fe_3S_4 \tag{5.1}$$

$$Fe_3S_4 + 2S_{0(s)} \rightarrow 3FeS_2 \tag{5.2}$$

This pathway conceivably takes place in the aquifer layer (the Upper Zone) where mackinawite, framboidal greigite, and framboidal pyrite were all observed. The

transformation process was found (Figure 5.2D) with microcrystalline framboidal greigite abutting framboidal pyrite. Mackinawite was also observed developing cubic faces and edges in this same zone (Figure 5.2E). Evidence suggests the following transformation pathway of $FeS_{(amorphous)} \rightarrow$ mackinawite $\rightarrow$ greigite $\rightarrow$ pyrite in the Upper Zone. Moreover, the presence of greigite in natural sediment systems has been reported to be related to a seasonal redox cyclicity and changes in the water table.[95] Throughout the Anaerobic Core samples, framboidal greigite was only observed in the Upper Zone, which is the shallowest RTZ with a sediment ORP observed between +76.1 and +538 mV. Because the formation of greigite from mackinawite results in two thirds of Fe(II) oxidation to Fe(III), the dynamic redox environment may be related to a fluctuating sediment redox that contributes to this transformation pathway. As a result, the presence of framboidal greigite may be considered an important indicator of RTZs.

In Zone 1 which transitions from an aquitard to aquifer, iron sulfide minerals were more abundant with clay mineral coatings of mackinawite, granular pyrite, and pyrrhotite, unique from the framboidal pyrite and greigite observed throughout the Upper Zone. Without morphological evidence of greigite, the potential abiotic transformation pathways of iron sulfides in Zone 1 may proceed by one of two routes when greigite is not present: (1) mackinawite reacts with S_0, polysulfides, or other S intermediates to form pyrite,[30, 96] or (2) H_2S is oxidized and mackinawite transforms to pyrite.[97] Both pathways may play a role in Zone 1. The greater presence of iron sulfide coatings observed in Zone 1 as compared to other RTZs may be explained by the elevated concentrations of sulfur and iron as well as the more reduced geochemical environment. Given a reduced sediment ORP (-63.5 to +138 mV) and neutral pH (6.3 to 7.5), sparingly soluble iron sulfide minerals

precipitate. Based on a statistical analysis of atomic ratios for iron sulfide coatings, minerals observed fall between pyrite and mackinawite suggesting an active transformation pathway. Interestingly, clay lenses in Zone 1 are present to a greater degree compared to the Upper Zone, which may also help to explain the formation of iron sulfide coatings. Clay minerals possess large surface areas supporting FeS clusters and related microorganisms.[98] These biogeochemical processes include reduction of Fe(III) minerals to Fe^{2+} with iron-reducers (e.g., *Geobacter*), and sulfate reduction with possibly *Desulfosporosinus*.

5.4 Pyrrhotite Characterization

As an iron (II) sulfide, pyrrhotite (Fe_7S_8, also given as $Fe_{1-x}S$ (x = 0 to 0.17)), a thermodynamically stable form of iron sulfides, is expected to be highly reactive in abiotic dehalogenation.[38] X-ray diffractograms reveal that pyrrhotite was observed throughout the two RTZs studied with its main peak located in the broad amorphous peak (from 13 to 17° 2θ). Further corroboration with FESEM/EDX demonstrated its presence in Zone 1 (Figure 5.3B and C) based on its characteristic pentagonal morphology as well as its composition and atomic ratio; the microcrystalline form is either hexagonal ($Fe_{10}S_{11}$) or monoclinic (Fe_7S_8). The formation of pyrrhotite from hematite and magnetite through biotic processes has been reported.[99, 100]

5.5 Magnetite Related Biogeochemical Processes

XRD results indicate that magnetite is widely distributed in clay lenses; however, aggregate clusters of magnetite were not observed in the FESEM/EDX data in this study. On the other

hand, because of its nanometer-scale particle size, magnetite may not have been distinguishable. In a number of studies,[31, 101-104] abiotic dehalogenation of chlorinated solvents has been investigated using magnetite and dissolved Fe(II), where the Fe^{2+} ion adsorbs on the mineral surface through a $\equiv Fe\text{-}O\text{-}Fe^{2+}$ structure ($\equiv Fe$ refers to structural iron in minerals). Dehalogenation has also been attributed to structural Fe^{2+} on the surface of magnetite.[105, 106] Magnetite shares the same atomic structure with greigite; both are inverse spinels. One potential pathway for magnetite transformation to pyrite is proposed to occur under elevated sulfide concentrations (>1 mM).[107] Moreover, new phases of iron oxyhydroxides are possibly developed from sorbed Fe(II) through interfacial electron transfer with structural Fe(III).[64, 108, 109] Magnetite nanocrystals have been reported to precipitate as individual nanoparticles through abiotic coprecipitation of ferrous and ferric ions in the aqueous phase, where cubo-octahedral-shaped particles form approximately 10 nm in size.[102]

5.6 Siderite Characterization

Siderite is an iron (II) carbonate mineral that is sensitive to oxidizing agents.[1] This mineral coating was observed in samples with relatively lower sulfur concentrations and abundant in deeper reduced aquifer layers. Although it has not been studied extensively, siderite is a reactive iron mineral that was used along with adsorbed Fe^{2+} to treat carbon tetrachloride.[27] The dehalogenation rate of reaction with siderite was four orders of magnitude lower than with mackinawite under the same experimental conditions. Each iron (II) atom in the siderite crystal is in octahedral coordination with CO_3^{2-} ions. The iron atoms can be substituted by other metal atoms in close atomic size such as Mn(II), Mg(II), and Ca(II),

forming different minerals with a similar structure. As a result, when siderite is found, rhodochrosite ($MnCO_3$), magnesite ($MgCO_3$), and calcite ($CaCO_3$) are often present. However, siderite did not appear to form distinguishable structures as it was not observed in FESEM/EDX analyses. In RTZs deeper than Zone 1, siderite was more commonly observed as a dominant Fe(II) mineral coating, where sulfides were not found; this may be because of the decreased availability of organic carbon and sulfate that impacts the S cycle.

5.7 Iron Oxyhydroxides and Gypsum

In RTZs, iron oxyhydroxide coatings detected include goethite, hematite, ferrihydrite, and lepidocrocite, and were ubiquitously distributed over the bulk mineral surfaces. The diameter of these iron mineral coatings ranged from several nanometers to tens of nanometers. In FESEM/EDX analyses, irregularly shaped aggregates of ferrihydrite nanoparticles were observed along with nanoflakes of lepidocrocite in the elevated iron-bearing sediment samples. The intensity of their primary peaks in XRD is weak compared to bulk minerals but nevertheless recognizable. In EDX mapping, Fe is uniformly observed throughout the surface. Fe(III) minerals and sulfate play important roles as electron acceptors for dehalorespirating bacteria in subsurface systems when oxygen is absent. Iron oxyhydroxide minerals have been studied along with sorbed Fe^{2+} in the dehalogenation of chlorinated solvents.

In more oxidized regions, gypsum ($CaSO_4 \cdot 2H_2O$) was observed as well and has the lowest solubility among all calcium sulfate minerals. These coatings were found in sulfur-rich zones both in aquifers and aquitards. From FESEM, characteristic thin to thick tubular morphologies were imaged, sometimes forming rosette-like clusters (Figure 5.2F). The

presence of oxidized forms of Fe- and/or S-related minerals along with reducing bacteria suggests active cycling of iron and sulfur in dynamic systems for the two RTZs studied.

5.8 Summary

Using complementary analyses, reactive iron mineral coatings in two RTZs from an industrial site with historical contamination were characterized where the in situ redox conditions were preserved. XRD revealed trends in bulk mineralogy and mineral coatings in these transition zones; changes in the Fe(II) and Fe(III) coatings demonstrated shifts in redox conditions. Framboidal pyrite was observed abutting framboidal greigite in the Upper Zone clay lenses. This structure is unique from the granular pyrite found in the Zone 1 aquitard suggesting different iron sulfide transformation pathways for the two zones. These structures are morphologically significant and require further study on pyrite coating nucleation and crystallization in RTZs. Zone 1 exhibits are more reduced redox potential than the Upper Zone and is rich in reactive, metastable mineral coatings. With Zone 1 transitioning from an aquifer to an aquitard, both bulk clay minerals as well as reactive iron mineral coatings are present to a greater degree as compared to the Upper Zone. Iron sulfide was found as flaky aggregates of mackinawite as well as pyrite and pyrrhotite in Zone 1. Based on the reactive mineral coatings observed in RTZs, abiotic dehalogenation is expected to be significant.

CHAPTER 6

GEOCHEMICAL STUDY ON REACTIVE IRON MINERAL COATINGS IN REDOX TRANSITION ZONES

In this section, based on geochemical analyses targeting iron mineral coatings, along with water chemistry and microbial data, potential natural attenuation processes in RTZs from the Anaerobic Core were delineated and evaluated. Given multiple lines of evidence he shallowest two redox transition zones are expected to play a significant role in the biogeochemical degradation of COCs. Reactions in other redox transition zones may be slower where iron mineral coatings are not dominant.

6.1 Geological Layers, Potential Redox Transition Zones, and Contaminants

The Anaerobic Core crosses five geological layers (Figure 6.1) based on observation and archived geological logs. In the shallowest layer, the B-Aquifer is located at DBS from 3 to 4.8 m and is dominant in yellowish brown sand with a greenish grey coated sand, clay lenses, cobbles, and gravel. Within this layer, the first potential RTZ referred to as the Upper Zone (DBS from 4 to 4.6 m, Figure 6.1) was identified based on an elevated concentration of iron along with a gradient in sulfur extending over 1.3 orders of magnitude. The B-C Clay is located at DBS from 4.8 to 6.3 m with cobbles, gravel, sand, and clayey silt becoming prevalent as a function of depth. The change from light brown to darker green and brown can be attributed to the shift in redox potential where mineral coatings transform from oxidized iron minerals to a more reduced form. Another RTZ referred to as Zone 1 (DBS from 6.4 to 7 m, Figure 6.1) is located at the interface from the
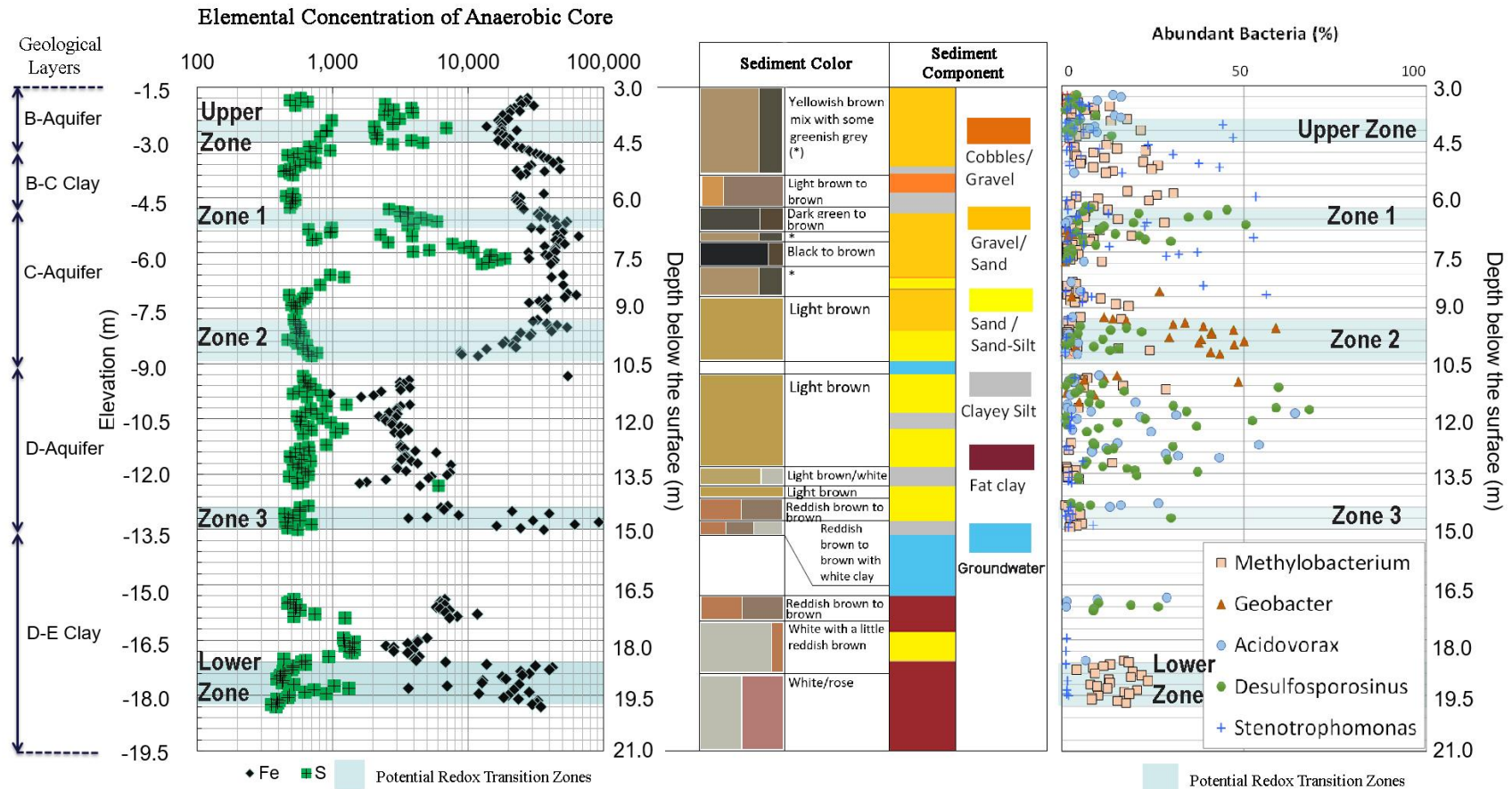
Figure 6.1 Concentrations of Fe and S in sediment as a function of depth along with sediment color and composition, as well as microbial community analysis. Geological layers identified are marked at the left side and RTZs are highlighted in light blue.

B-C Clay to the shallow C-Aquifer where gradients in iron and sulfur concentrations were found. The C-Aquifer (DBS from 6.3 to 10.5 m) is dominated by sand where a viscous colloidal mass is observed in this layer, there is evidence of residual NAPL. The following RTZ, Zone 2 (DBS from 9.5 to 10.7 m, Figure 6.1), is in this aquifer layer with relatively low sulfur concentrations and iron concentrations that again have a steep gradient decreasing as a function of depth (Figure 6.1). A relatively thin aquitard (approximately 0.5 m thick) separates the D-Aquifer (DBS from 10.5 to 15 m) from the C-Aquifer. Without visible NAPLs, light brown sand with very little silty clay comprises the D-Aquifer. Deeper in the D-Aquifer (approximately at DBS of 15 m), white clay lenses identified as kaolinite with reddish brown striping from iron. The RTZ referred to as Zone 3 (DBS from 14.6 to 15.3 m, Figure 6.1) is located in this interface with low sulfur concentrations and gradients in iron concentration. The deepest identified RTZ, the Lower Zone (DBS from 19 to 20.1 m, Figure 1), is located in what is referred to as the D-E Clay (4.2 m thick to the end of the core); this with high-density and low-permeability kaolinite layer retards transport into other layers.

The groundwater data from the MLS (Figure 6.2) shows that relatively high concentrations of 1,2-dichlorobenzene, 1,3-dichlorobenzene, and 1,4-dichlorobenzene were detected in the C-Aquifer and D-Aquifer. The high concentration of COCs in both the C-Aquifer can be attributed to the presence of NAPLs observed at the same depth in sediment. In the D-Aquifer, higher concentrations in the groundwater may be caused by the accumulation of contaminants above the D-E Clay layer. A similar trend of concentration is found for chlorobenzene. Other probed contaminants such as aniline,

nitrobenzene, and benzene peaked at Zone 1, the transition interface from the B-C Clay to the C-Aquifer.

6.2 Microbial Group Profiles

Based on the previous study,[78] the five most abundant OTUs can explain up to 80% of the bacteria genera: *Methylobacterium*, *Geobacter*, *Acidovorax*, *Desulfosporosinus*, and *Stenotrophomonas* (Figure 6.1). *Methylobacterium* species are reported to be responsible for the degradation of organics such as polycyclic aromatic hydrocarbons (PAHs) and dichloromethane.[111, 112] OTUs of *Methylobacterium* were found in the Upper Zone, Zone 1, and Zone 2. Species of *Geobacter* are generally considered as widespread iron-reducing bacteria in anaerobic environments and have the ability to oxidize organic matter by utilizing Fe(III) as an electron acceptor.[113, 114] OTUs of *Geobacter* are observed abundantly in Zone 2. Some species from *Acidovorax* are reported as degraders of aromatic organics such as PAHs[115] and nitrate-reducing Fe(II)-oxidizers.[116] These genera can be found throughout most of the anaerobic sediment samples peaking between Zone 2 and Zone 3 in the D-Aquifer. *Desulfosporosinus*, a sulfate-reducing bacterium,[117] has been reported in organic- or metal-contaminated environments.[118, 119] Species from *Stenotrophomonas* have been identified as degraders for many organics including acenaphthylene, phenanthrene, 4-chloroanilines, chlorocatechol, and even high-molecular-weight PAHs.[111, 120-122] These genera were found in most samples above Zone 2, decreasing at greater depths.
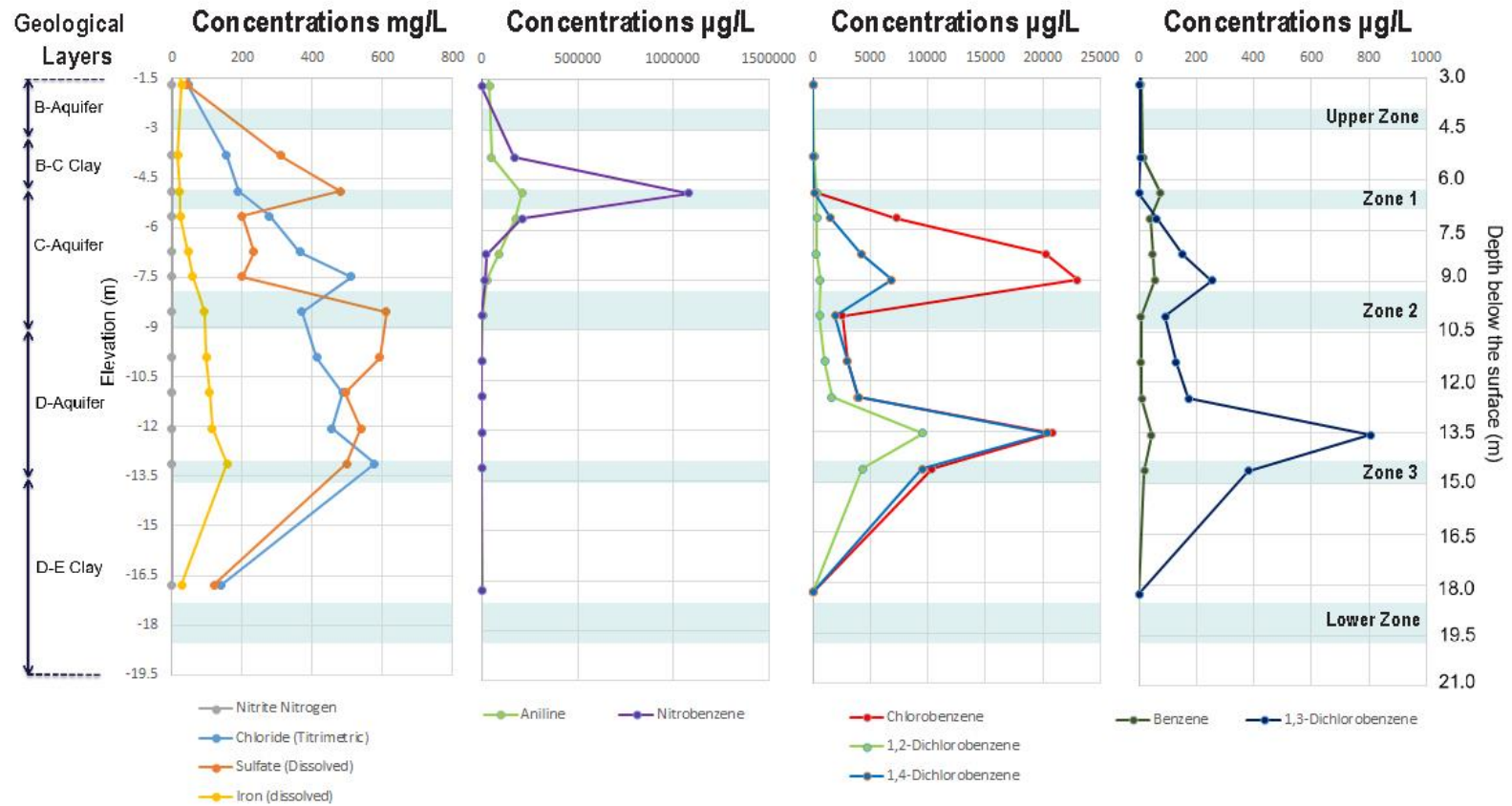
Figure 6.2 Concentrations of COCs and several inorganic species in groundwater from sampling conducted by AECOM[110] as a function of depth based on MLS data with geological layers and RTZs marked.

6.3 Iron Mineral Coatings Profiles

6.3.1 XRD Analysis for Iron Mineral Coatings

Iron mineral candidates resolved in XRD analysis can be divided into three phases: Fe(II), Fe(II/III), and Fe(III) (Figure 6.3; Appendices A and B). Fe(II) minerals include mackinawite (FeS), pyrrhotite ($Fe_{1-x}S$ (where x = 0 to 0.17)), siderite ($FeCO_3$), and pyrite(FeS_2). Mackinawite is a metastable, highly reactive monosulfide that is sparingly soluble, exhibiting a large surface area and precipitating under reduced conditions.[123] The most intense peak from mackinawite was detected at 5 Å (17.7º 2θ) in diffractograms.[124] Pyrrhotite was found in most samples throughout RTZs where its main peaks are overlapped by the broad peak (from 13 to 18º 2θ in XRD diffractograms) from amorphous minerals; its presence requires further confirmation through SE and FESEM/EDX. Pyrite is a thermodynamically stable form of iron sulfide normally found in sediments with little to no oxygen. Siderite forms under reduced conditions with low sulfur concentrations. The only Fe(II)/(III) mineral resolved with XRD is magnetite (Fe_3O_4). Fe(III) minerals included goethite (α-FeO(OH)), ferrihydrite (generally considered as $5Fe_2O_3 \cdot 9H_2O$),[125] hematite (Fe_2O_3), and lepidocrocite (γ-FeO(OH)). Reactive iron mineral coatings are susceptible to the ambient microenvironment through related biogeochemical reactions at and near the mineral-water interfaces. Among the RTZs studied with XRD, shifting of iron mineral coatings between Fe(II), Fe(II/III), and Fe(III) phases suggests dynamic redox environments. In the Upper Zone, Fe(III) species are dominant at shallower depths. Meanwhile, deeper in this zone, signals from Fe(II) minerals such as mackinawite, siderite, and pyrite reveal themselves with a corresponding decrease in the Fe(III) minerals, indicating a more reduced condition. In Zone 1, where the greatest concentration of iron
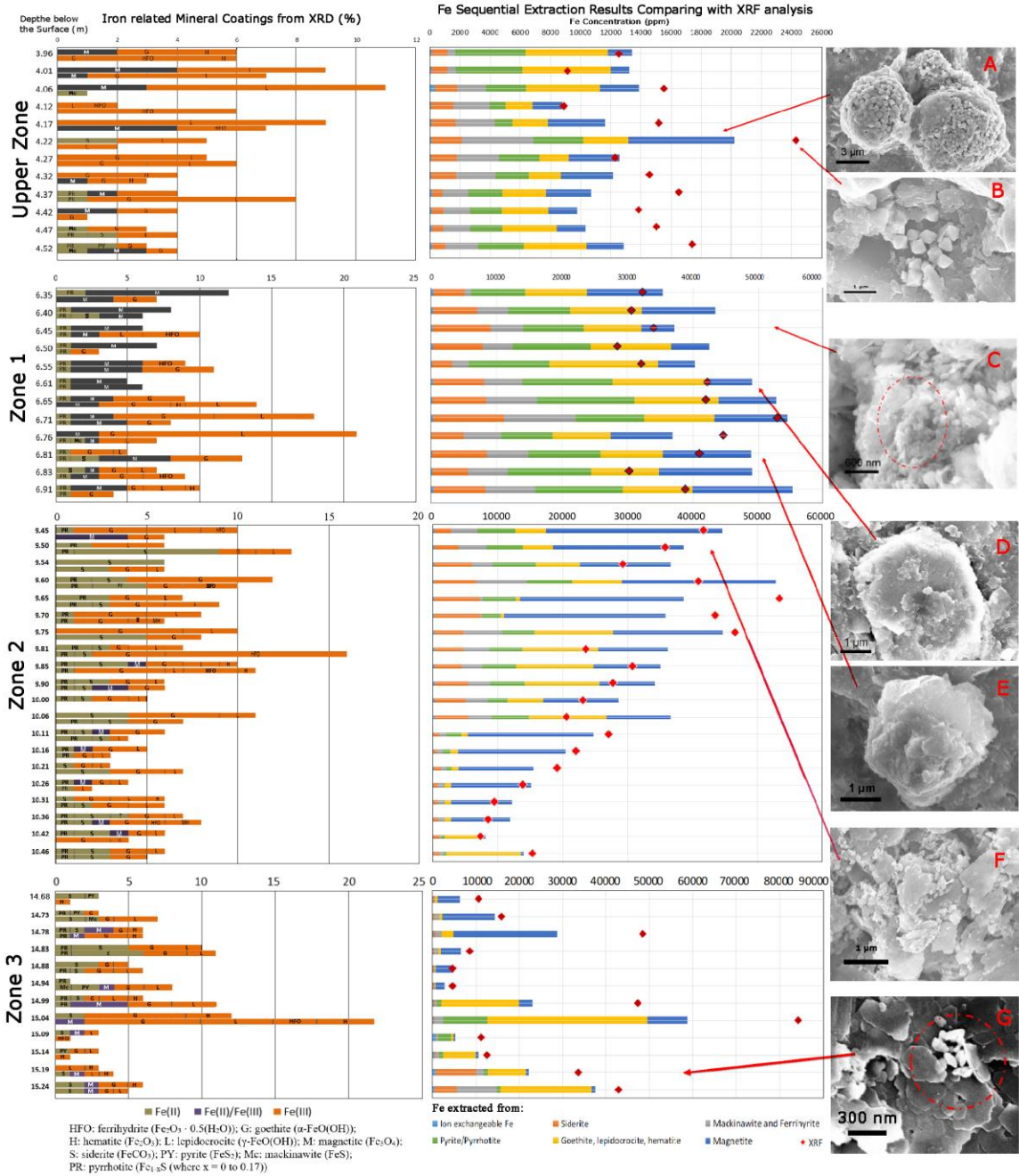
Figure 6.3 Iron mineral coatings identified using XRD in the Upper Zone, Zone 1, Zone 2, and Zone 3, along with iron concentrations based on SE. FESEM images of reactive iron mineral coatings found in RTZs include (A) framboids of pyrite and greigite, (B) octahedral greigite, (C) mackinawite, (D) euhedral pyrite, (F) amorphous iron oxyhydroxide coatings, and (G) kidney-shaped hematite.

mineral coatings is found, the sediments are relatively reduced with Fe(II)/(III) phases at shallower depths and an increase in Fe(III) mineral coatings at the deeper depths, peaking at 6.65 to 6.76 m DBS. Within Zone 2, the trend of the redox transition is not as obvious as in the Upper Zone and Zone 1. The concentration of iron mineral coatings decreases to less than 10,000 ppm with siderite being the most dominant Fe(II) mineral present. In Zone 3, iron sulfide coatings can be found in the shallowest samples; however, Fe(III) mineral coatings are overall prevalent in this zone. The significant variability in iron coating concentrations in this zone may be attributed to reduced transport in the highly dense kaolinite aquitard.

6.3.2 Sequential Extraction

The six-step SE is an approach for quantifying Fe minerals that include ion exchangeable Fe, carbonate Fe, poorly crystalline Fe minerals (e.g., mackinawite and ferrihydrite), reducible iron oxides (e.g., goethite, lepidocrocite, and hematite), magnetite, and pyrite/pyrrhotite (Table 4.1; Figure 6.3). In previous analysis,[78] total extracted iron was compared to the total Fe concentration determined with XRF; and while there is heterogeneity in the sediment, system errors in SE processes accumulate between each step of extraction and contribute to uncertainty in the mass balance. In addition, Fe associated with silicates in the bulk minerals were not extracted. Generally, the trend of Fe mineral coatings is somewhat consistent with XRD (Figure 6.3). In the RTZs studied, reduced iron phases of pyrite/pyrrhotite and poorly crystalline Fe minerals (including mackinawite) were found to be most abundant in the Upper Zone and Zone 1. Particularly for Zone 1, where the highest concentrations of iron mineral coatings were found when compared to other RTZs, reactive iron sulfide coatings of pyrite/pyrrhotite and poorly crystalline phases

made up approximately 40% of the total extracted Fe (Figure 6.3). Interestingly, in Zone 2, the total concentration of extracted iron phases dropped dramatically as a function of depth. Among all extracted iron phases, the concentrations of reducible oxides and poorly crystalline minerals decreased, which is likely a result of their loss in biogeochemical reactions. In Zone 3, extracted iron ranged from approximately 2,700 to 59,000 ppm and the trend was in agreement with other analyses including XRF and XRD.

6.3.3 FESEM/EDX Analyses for Mineral Coatings

In the EDX mapping analysis, iron sulfide minerals (such as mackinawite, pyrite, and pyrrhotite) and iron oxyhydroxides are generally more easily probed given that mineral coating aggregates formed on the bulk mineral surface (Figure 6.3A to G) [124]. The iron sulfides were observed in the Upper Zone and Zone 1, where the atomic ratio of iron to sulfur (Fe/S) ranged from 0.4 to 1.4 (Figure 6.4). Higher concentrations of the iron sulfide coatings were found in Zone1 than in the Upper Zone, and these locations were resolved based on both EDX mapping Fe and S locations and FESESM analysis. Interestingly, in the Upper Zone, the mineral coating of greigite is observed as spherical framboids with FESEM. However, signals from greigite are not picked up by XRD as it exhibits a similar mineral lattice as mackinawite [92]. Framboidal greigite in the Upper Zone is found abutting framboidal pyrite and is indicative of the transformation pathway from mackinawite to pyrite through the intermediate greigite [87]. However, distinct from the Upper Zone, pyrite in Zone 1 presented as granular particles without greigite revealing a different pathway. Moreover, the presence of pyrrhotite coatings was confirmed only in Zone 1 with FESEM/EDX identification, which supports a reduced environment. Iron oxyhydroxide

coatings detected include goethite, hematite, ferrihydrite, and lepidocrocite, and they are ubiquitously distributed on the bulk mineral surfaces throughout all RTZs.
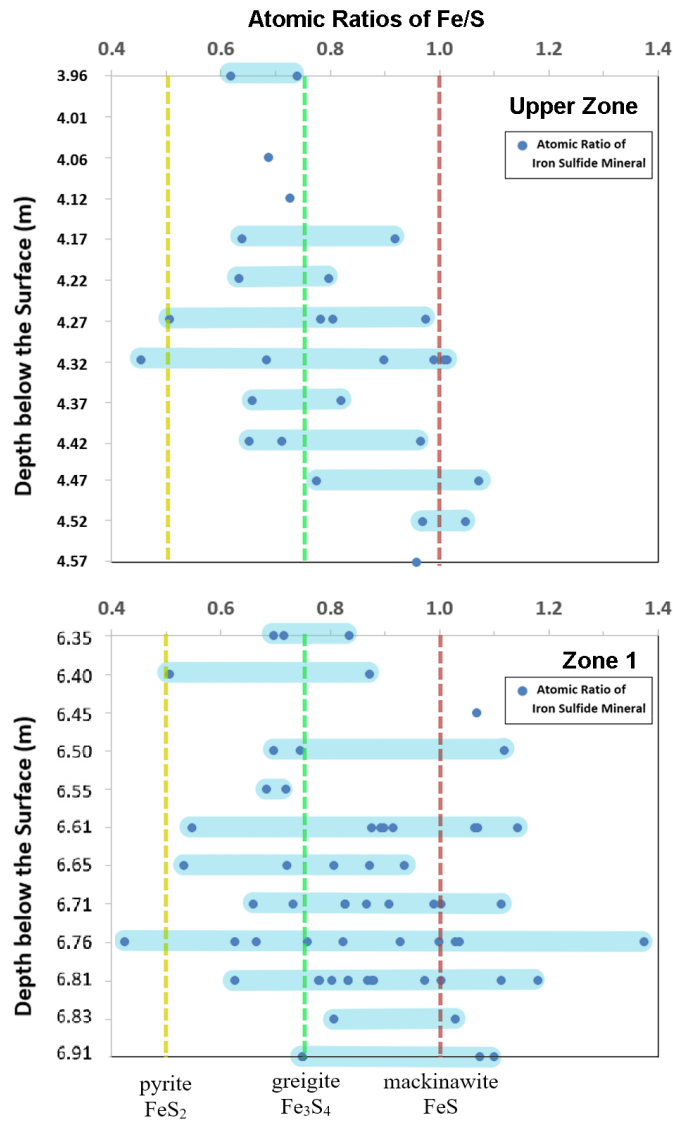
Figure 6.4 Atomic ratios of Fe/S for all identified iron sulfide mineral coatings in the Upper Zone and Zone 1 based on EDX elemental composition analysis.

6.4 Fe and S Cycling in Redox Transition Zones

Active cycling of Fe and S in mineral coatings in RTZs is important in the transformation of COCs through biogeochemical redox reactions. On one hand, oxidized phases including Fe(III) minerals and sulfate minerals/compounds play a role as electron acceptors and macronutrients in many co-metabolism and dehalorespiration processes in the biotic transformation of chlorinated solvent.[8, 9] On the other hand, reduced iron minerals have been found important in the abiotic degradation of chlorinated organics.[1, 35] The redox status of iron mineral coatings to some extent represents the critical surface reactions with related (a)biotic processes. Reduced iron minerals may initially precipitate from aqueous phases containing Fe^{2+} and sulfide as iron monosulfides (e.g., mackinawite $FeS_{(s)}$) in an anaerobic environment.[123] However, $FeS_{(s)}$ is a thermodynamically metastable form that will transform into stable forms of iron sulfides (e.g., pyrite (FeS_2)). In one abiotic transformation pathway, greigite forms as an intermediate species through the partial oxidation of mackinawite in the absence of O_2 (Reaction 5.1).[126, 127] Greigite ($Fe_3S_{4(s)}$) undergoes further transformation into pyrite.[94, 100] In our work, framboids of pyrite and greigite abutting each other in the Upper Zone are evidence of this transformation pathway (Figure 6.3A) shown in Reactions (5.1) and (5.2). This pathway is also observed in natural sediment of near-shore, shoreline, and freshwater systems with oscillatory redox conditions.[90, 95] Moreover, the formation of greigite can also be achieved with low concentrations of dissolved O_2 carried by groundwater. The size of pyrite framboids can be limited by growth between oxic-anoxic boundary and rate of crystal growth;[128, 129] these framboids have been reported as much smaller in anoxic than sub-oxic zones. In the shallower part of the Upper Zone at DBS between 4 and 4.2 m, the atomic ratios of Fe/S

based on FESEM/EDX analysis range from 0.6 to 0.75 which is more consistent with greigite than mackinawite and pyrite (Figure 6.4). In deeper areas of the Upper Zone, where more mackinawite (FeS) coatings were found, the redox condition is more reduced. Other abiotic pathways to generate pyrite from monosulfides, where greigite is not an intermediate, include directly reacting with S^0 polysulfides, and other sulfide intermediates generated from the oxidation of H_2S[96] as well as H_2S itself:[127]

$$FeS_{(s)} + S^0 \rightarrow FeS_{2(s)} \tag{6.1}$$

$$FeS_{(s)} + S_n^{2-} \rightarrow FeS_{2(s)} + S_{n-1}^{2-} \tag{6.2}$$

$$FeS_{(s)} + H_2S_{(aq)} \rightarrow FeS_{2(s)} + H_{2(g)} \tag{6.3}$$

These pathways are more consistent with the observation of iron sulfides in Zone 1, a more reduced condition compared to the Upper Zone. Even though iron sulfide coatings are observed with Fe/S ratios of 0.75 consistent with greigite (Figure 6.4), the mineral coatings morphology is consistent with the flakey morphological appearance of mackinawite (Figure 6.3C) or well-crystalline pyrite/pyrrhotite (Figure 6.3D and E). The abiotic transformation of iron sulfides was reported to be enhanced in the presence of organic matter and microorganisms in clay-rich sediment.[130] This enhancement has been explained by the H_2S generated through other biotic activities with microorganisms[131, 132] and the nucleation process of FeS on the bacterial cell surface.[133] Other pathways include the formation of iron sulfide minerals through the reaction of Fe(II) oxyhydroxides with H_2S[134], but no evidence can support this pathway in RTZs studied.

The oxidation of iron sulfides in the first two RTZs may be facilitated by Fe(III) minerals, dissolved O_2, and O_2 secondary products (e.g., reactive oxygen species ($O_2^{\bullet -}$), hydrogen peroxide, and $OH^\bullet$) in both biotic and abiotic pathways [135-137]. Bacteria that

potentially enhance related reactions and are reported to be present in environments from sub-oxic to anaerobic[138] include the genera *Acidovorax*, which is abundant in the B-Aquifer above the Upper Zone and the D-Aquifer (Figure 6.1). These redox reactions result in Fe(III) oxides, hydroxides, oxyhydroxides, or oxyhydroxysulfates,[139] as well as sulfate minerals (e.g., gypsum ($CaSO_4 \cdot 2H_2O$)) and dissolved sulfate in the aqueous phase. Moreover, in the presence of chlorinated contaminants, iron sulfide minerals can be oxidized during abiotic dehalogenation under anaerobic conditions.[23, 31]

To complete the cycling of Fe and S, Fe(III) minerals and sulfate are expected to replenish Fe^{2+} and S^{2-} consumed by biogeochemical reactions in RTZs through reductive transformations. Although Fe and S minerals can accept the electrons from their reduced forms through abiotic reactions,[140] the data collected in RTZs suggest that microbiological sulfate respiration may be a greater contributor. The process begins with a H_2S sink generated by sulfate-reducing bacteria during respiration:[134]

$$2CH_2O + SO_4^{2-} \rightarrow 2HCO_3^- + H_2S \tag{6.4}$$

Fe(III) minerals such as goethite are reduced within the H_2S sink and generate iron sulfide abiotically:[141]

$$2FeOOH_{(S)} + 3H_2S_{(aq)} \rightarrow 2FeS_{(s)} + S^0 + 4H_2O \tag{6.5}$$

Furthermore, related studies found microbial reduction of Fe(III) minerals by Fe(III)-reducing microorganisms (FeRM) generally controlled the reduction process in non-sulfidogenic sediments. The electron donors utilized by FeRM include not only organic carbon compounds but also inorganic sources such as hydrogen and ammonium.[142] FeRM related reduction processes can generate aqueous Fe(II), Fe(II) minerals (e.g., siderite and mackinawite), and significant Fe(II)/(III) minerals (e.g., magnetite).[143] Based on the

microbial analysis, genera *Geobacter* is potentially responsible for biotic iron-reducing conditions and *Desulfosporosinus* for sulfate-reducing conditions in RTZs (Figure 6.1).

6.5 Natural Attenuation Processes in Redox Transition Zones

The Fe and S mineral transformation pathways identified above to delineate Fe and S cycling in the RTZs support the abiotic contributions in natural attenuation of COCs in these reactions. The degree of natural attenuation activity may be evaluated using multiple lines of evidence collected in this study. The first highly contaminated zone of COCs can be from NAPLs observed in the C-Aquifer between Zone1 and Zone 2 where elevated Fe and S concentrations were found with the dominant genera *Stenotrophomonas*. Moreover, groundwater plumes that include 1,2-dichlorobenzene, 1,3-dichlorobenzene, 1,4-dichlorobenzene, and chlorobenzene are indicative of a second zone of contamination located deeper in the D-Aquifer above Zone 3; the NAPL source is expected to be located at D-E Clay layer. In this area, Fe and S concentrations are relatively low, although *Acidovorax* and *Desulfosporosinus* are abundant. The degradation of COCs is expected through (a)biotic dechlorination processes followed by aromatic organic degradation with self-enriching microorganisms in sediment.

Of the RTZs identified, the Upper Zone groundwater analyses revealed the lowest concentrations of contaminants. Nonetheless, OTUs of the contaminant degraders *Stenotrophomonas* and *Methylobacterium* were significant (Figure 6.1). Iron sulfide minerals are present at relatively high concentrations in this zone as are Fe(II)/(III) minerals, such as greigite and magnetite, indicating potentially active cycling of Fe and S. However, the total concentration of iron coatings determined by SE and XRD is not as high as that

found in the RTZ, Zone 1. Although the activity of abiotic degradation may be limited by the total concentration of iron mineral coatings, reactive natural attenuation processes are expected in this zone, and may be indicated by the low COC concentrations.

Abiotic dehalogenation processes may play a more crucial role in natural attenuation within Zone 1 than in other RTZs. The dominant reduced iron minerals include mackinawite and pyrite, which are highly reactive in dehalogenation.[35] SE results suggest the highest concentrations of total iron mineral coatings can be extracted from Zone 1 among all identified RTZs. Given the dominant OTUs of *Desulfosporosinus* (Figure 6.1), reactive cycling of Fe and S can be expected in this Zone through related (a)biotic reactions. In groundwater data, a high concentration of benzene (Figure 6.2) may be because of the dechlorination of (di)chlorinated benzenes. Moreover, another daughter product, chloride also increases significantly as a function of depth in Zone 1. Although aniline and benzene are difficult to degrade through abiotic reactions alone, clay lenses found in this zone together with Fe(III) mineral coatings serve as substrates with a high surface area and a strong affinity for organics, which potentially enhance further biotic degradation of aromatic organics. Additionally, dissolved Fe(II) adsorbed onto the surface of oxidized minerals further supports abiotic reduction by forming the $\equiv$Fe-O-Fe^{2+} structure with oxidized iron[144]). Reduced iron sulfides consumed in abiotic dehalogenation can be replenished through sulfate-reducing microorganisms at the same time. Zone 1 is an important example of how biotic and abiotic processes work together to achieve self-sustaining natural attenuation through redox cycling of iron reactive minerals.

In contrast to Zone 1, Zone 2 is in the C-Aquifer below the NAPL-bearing area where a high concentration of iron mineral coatings is observed. However, concentrations

of Fe mineral coatings drop steeply as a function of depth (Figures 6.1 and 6.3). At the same time, the dissolved oxygen concentration and pH in groundwater do not show significant changes (Appendix C), which may be artifacts of the sampling and analytical methods. Siderite is the most dominant reduced iron mineral coating in this zone and has been reported to result in slower rates of dehalogenation compared to iron sulfides.[27, 145] In this zone, S concentrations were low and, morphologically, the most abundant mineral coatings were Fe(III) oxyhydroxides. Sulfur is most rich in the aqueous phase as sulfate. Although the dominant OTUs are *Geobacter* and *Desulfosporosinus* (Figure 6.1), iron sulfides were not observed. While these genera are known degraders of contaminants using reactive iron minerals as an electron donor/acceptor, the continuously decreasing iron concentration profile is expected to limit biotic processes in this zone. The potential daughter product benzene, from natural attenuation of COCs also decreases as a function of depth suggesting attenuation via dechlorination of chlorinated benzenes may not be significant. In contrast, low concentrations of benzene could be indictive of on-going biodegradation of this compounds in Zone 2. Two observations in Zone 2 are of interest: the significant difference (i.e., dominant with *Geobacter*) in the microbial community compared to other zones and the lack of interfaces with clay lenses. The former one can be impacted by factors such as the availability of organics and competition between microbes in natural sediment. Since Geobacter is known to degrade benzene,[146] its presence could indicate ongoing biodegradation of this COC. The latter may cause differences in mass transfer, sediment porosity, and surface area, impacting mineral-water interfaces as well as groundwater hydrology. These factors will be further studied in future work.

The gradients in oxidized/reduced mineral coatings in Zone 3 is mainly because of the poor mass transfer in this clay layer and the high concentration of dissolved oxygen contributed by the abutting groundwater. This zone is considered to have a significant gradient in the redox potential; however, it is not evident that there is an attenuation of COCs.

6.6 Summary

Based on geochemical analyses targeting iron mineral coatings, along with water chemistry and microbial data, potential natural attenuation processes in RTZs from the Anaerobic Core have been delineated and evaluated, and implications for biotic and abiotic degradation have been developed. Although active attenuation of COCs is expected to be carried out by biogeochemical cycling of reactive iron mineral coatings, this study indicates that cycling of Fe and S in RTZs can be very different and complicated. Given the complex nature of (a)biotic processes, both indicator microbial species and surface mineral coatings are needed for interpreting ongoing contaminant attenuation in sediment. In identifying reactive iron coatings, XRD supports quantifying crystalline mineral coatings but is greatly limited by interference from bulk minerals. SE focuses on isolating and quantifying different phases of iron minerals; however, results can be impacted by the heterogeneity of the sample as well as uncertainty in the extraction analysis. These two methods in general show similar trends for iron coatings throughout all RTZs. FESEM/EDX provides more detailed information on mineral morphology and elemental composition of iron coatings which helps to identify mineral coatings and reveal potential transformation pathways for reactive iron coatings; this was most significant for the Upper Zone and Zone 1. The presence of reactive iron mineral coatings such as mackinawite (FeS) and pyrite (FeS_2) can

be considered an important indicator of active abiotic dehalogenation of COCs. However, for the long-term remediation and further break down of benzene rings, biotic degradation is necessary. Some species of iron- and sulfate-reducing bacteria can utilize Fe(III) and SO_4^{2-} as electron acceptors to replenish consumed Fe^{2+} and H_2S under anaerobic conditions. Moreover, with high surface area and strong affinity for microorganisms as well as organics, iron oxyhydroxides serve as an important surface for biotic degradation of COCs. Ideally, abiotic and biotic degradation mutually benefit each other, and both are expected to occur in the Upper Zone and Zone 1. However, in some circumstances, iron sulfide does not effectively precipitate from pools of sulfate and dissolved Fe^{2+} in the presence of iron- and sulfate-reducing bacteria for reasons that are not totally understood. Conclusions from this geochemical study of the Anaerobic Core include:

- Natural attenuation can be expected to be active and long-lasting at RTZs where reactive iron mineral coatings cycle between oxidized and reduced status through biogeochemical reactions.

- For the cycling of iron and sulfur in RTZs, the abiotic and biotic processes are inseparable and rely on one another for the sustainability of continued cycling.

- Siderite as a dominant reduced iron coating in RTZs is not expected to play an important role in attenuation as compared to the iron sulfide minerals.

- RTZs occur in the transition of interfaces between aquifers and clay lenses or aquitards in sediment where both biotic and abiotic degradation are expected to be most significant.

CHAPTER 7

IMPACT OF CRYOGENIC SAMPLING PROCESS ON IRON MINERAL COATINGS IN CONTAMINATED SEDIMENT

This study focused on comparing iron mineral coatings found in contaminated sediments from a cryogenic (Cryo Core) core versus an Anaerobic Core. After thawing the Cryo Core in an oxygen-free glovebox, a suite of analyses was applied on sediments from both cores. Moreover, to better understand why the metastable minerals were not present, a freeze/thaw process was simulated on Anaerobic Core samples using a liquid-nitrogen quench with surface coatings characterized by FESEM/EDX.

7.1 Freeze-Induced Acceleration Reaction

In-situ sampling techniques with liquid nitrogen (at 77 K) and CO_2 (at 195 K) are known as cryogenic core collection processes that have been widely used for collecting saturated and cohesionless sediments.[147-152] Physical, chemical, and biological characteristics of cryogenic core sediment have been probed for constituents of concern including the presence of volatile organic compounds, oxidation/reduction (redox)-sensitive inorganic couples, and the microbiology.[153-155] In general, chemical and microbial reaction rates in the frozen sediment are slowed because of the relatively low temperature. However, studies[156-161] have shown that some reactions are accelerated in ice at very low temperatures. Pincock[156] proposed that the driving force for these accelerated reactions was because of unfrozen areas of solution and therefore concentrated solute in ice. In O'Concubhair and Sodeau review,[162] several mechanisms have been attributed to this freeze-induced acceleration reaction. One mechanism involves the freeze-concentration occurring when a large number of solutes are rejected from the growing ice crystals, and reaction rates are

elevated by the concentrated unfrozen solute in space not occupied by the ice structure; reactions of second order or higher are affected by the elevated concentrations in solution.[163] The second type of mechanism is the freezing potential: a small portion of solute can be incorporated from solution into the ice. Because of the imbalance of incorporated cations and anions, an electric potential is generated at the ice-water interface.[164-166] This potential may be negative or positive based on the initial conditions and ions present, and the magnitude is more dependent on ion size, structure, and their concentrations in the solution, as well as growth rate and surface condition of the ice.[167] In this case, diffusion of H^+ and OH^- ions at the ice/water interface neutralizes the imbalanced charge.[168] Another mechanism is referred to as the catalytic effect of the ice-liquid water interface: unique characteristics have been observed in a thin wet layer on the ice surface known as a quasi-liquid layer (QLL) unique from pure liquid water. This interface of atoms/molecules in QLL encounters unequal bonding forces from one side to another.[169] Other effects include convection where the concentration gradient of the solution is impacted by the direction of freezing and temperature differences; variations in the sample can lead to differing thermodynamics and kinetics of reactions. Among the mechanisms described above, freeze-concentration and freezing potential are reported to be the dominant factors in accelerating reactions.[166, 170]

7.2 Bulk and Iron Coating Identification in the Cryo Core

7.2.1 XRD Analysis

The most dominant peaks are from quartz, which are also used to correct diffractogram shifting. Other bulk minerals (Figure 7.1) include anorthite and albite belonging to the feldspar group, two clay minerals, muscovite and clinochlore, from the mica and chlorite groups, respectively, as well as different forms of zeolite which potentially developed during weathering of feldspar precursor minerals.[86] Generally, the bulk mineralogy identified in the Cryo Core shows consistency with the Anaerobic Core at a similar depth. For iron-containing mineral coatings, semi-quantitative analysis was constrained based on the possible candidates provided by the search and match program (PANalytical's HighScore plus, ver. 3.0.5) with relatively high match scores. Fe(II) mineral fractions include pyrrhotite ($Fe_{1-x}S$ (where x = 0 to 0.17)), siderite ($FeCO_3$), and pyrite (FeS_2). Magnetite (Fe_3O_4) was the only Fe(II)/(III) mineral detected. Fe(III) mineral fractions observed included goethite (α-FeO(OH)), ferrihydrite (generally considered as $5Fe_2O_3 \cdot 9H_2O$),[125] and lepidocrocite (γ-FeO(OH)). Iron coatings at low concentrations (around 1% mass) may be difficult to distinguish in XRD, as their main peaks are possibly located within other peaks such as a broad peak from an amorphous mineral that overlaps along with strong peaks from bulk minerals. Furthermore, distinguishing the presence of lower concentration iron mineral coatings was further resolved using complementary analyses in the following FESEM/EDX section. Pyrite was distinguishable in diffractograms (Figure 7.1 and Appendix D). As discussed above, the trend observed in the Fe(II), Fe(II/III), Fe(III) mineral coatings throughout the core studied demonstrates the
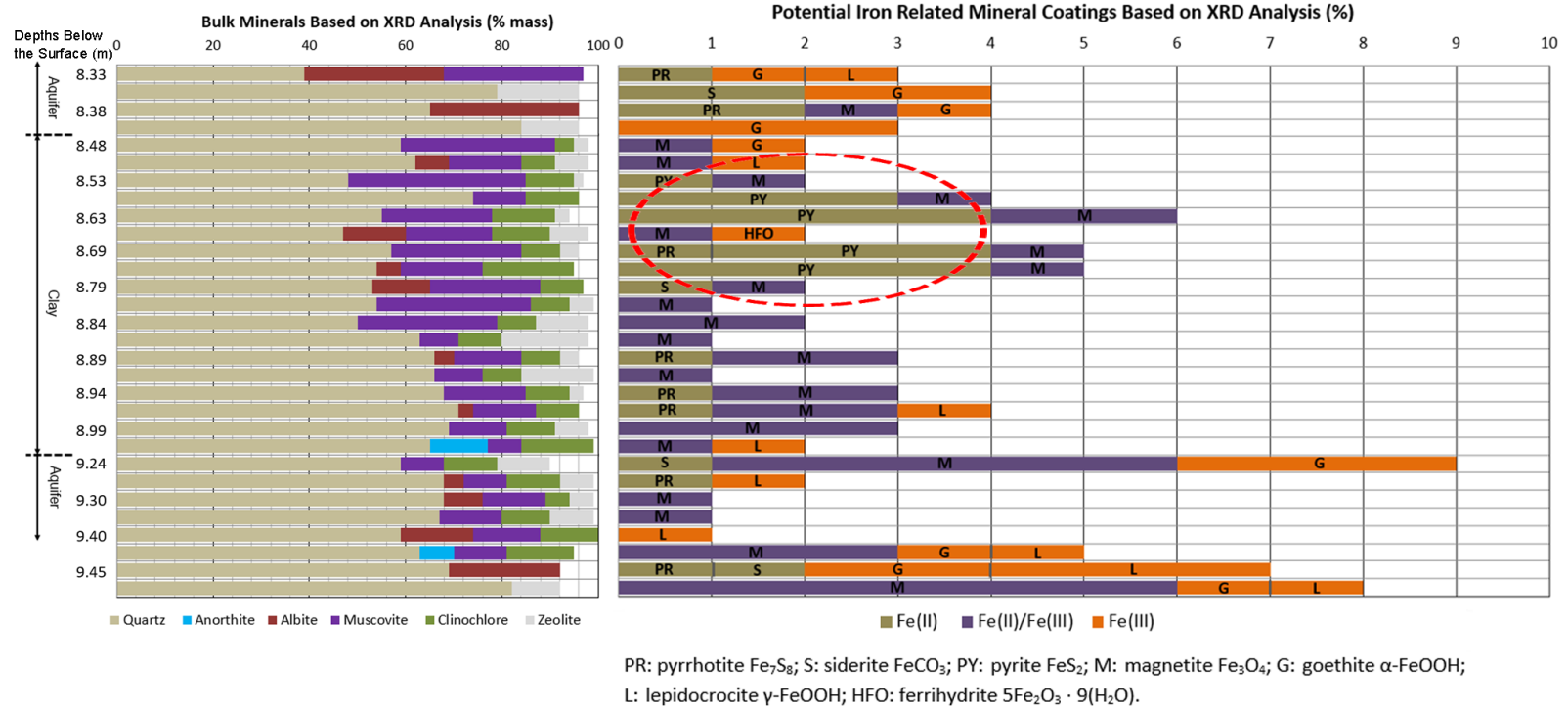
Figure 7.1 XRD identification and semi-quantification results for bulk minerals as well as iron related mineral coatings in the section of 8.33 to 9.45 m DBS.

redox changes. Compared to the relatively low concentrations in the anaerobic core, elevated concentrations of pyrite were found in the Cryo Core.

The zone of focus (8.28 to 9.45 m DBS, Figure 7.1) can be divided into a clay layer (aquitard) of intact sediments sandwiched between two sandy aquifers. Pyrite peaks at the top of the clay layer ranging from 8.53 to 8.69 m DBS (Figure 7.1, dashed oval) with lower concentrations of Fe(III) minerals than in sandy aquifers. In contrast, for the aquifers, siderite is the more dominant Fe(II) mineral and is collocated with higher concentrations of Fe(III) minerals including goethite and lepidocrocite. The trend in dominant iron mineral coatings indicates a redox gradient from the upper aquifer layer through the adjacent clay layer where the highest concentration of pyrite was observed.

7.2.2 FESEM/EDX

For (1,500×) EDX mapping, iron mineral coatings include crystalline iron sulfides and iron oxyhydroxides with diameters greater than 300 nm, easily distinguishable from bulk minerals throughout the Cryo Core. However, some iron mineral coatings found with XRD may not be as easily identified by EDX mapping because of the limits in crystalline size and randomness in mapping locations. FESEM results indicate that iron sulfides identified in the Cryo Core are mostly pyrite peaking at a DBS between 8.48 and 8.64 m, which is consistent with XRD analysis and XRF screening of Fe and S concentrations. Two samples (Figures 7.2A and B) highlight the elevated concentration of pyrite randomly scattered on the bulk mineral surface. Multiple morphologies were observed as individual grains of cubic or octahedral pyrite abut truncated grains (Figure 7.2C), spherical-packed framboids (Figure 7.2D), or raspberry-shaped aggregates of pyrite interpenetrated in different
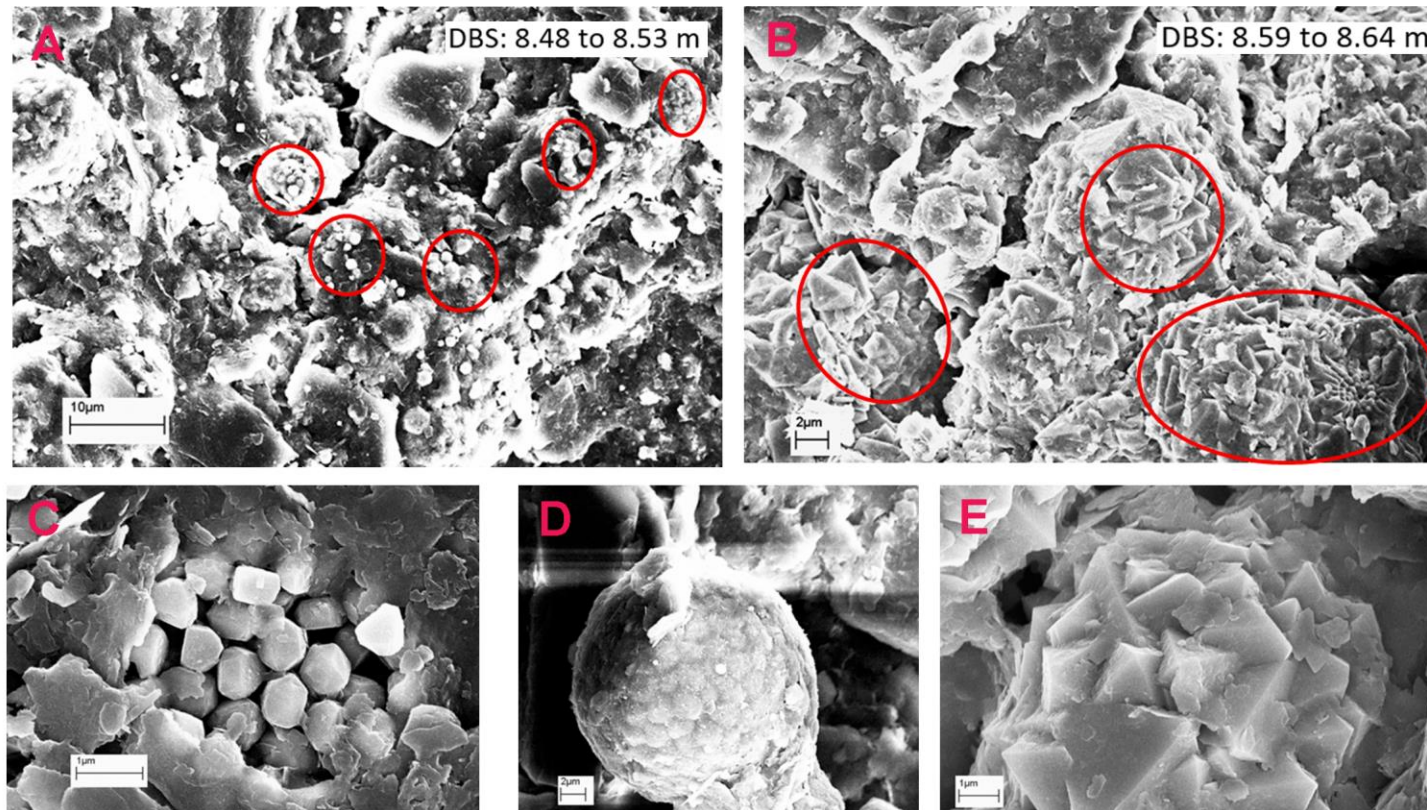
Figure 7.2 Morphology of mineral coatings observed in two samples by FESEM. (A): iron sulfide mineral coatings on the bulk mineral surface, framboidal and cubic/octahedral pyrite are observed; (B): coatings of interpenetrated highly crystalline pyrite; (C): framboidal pyrite with irregular nanoparticles; (D): spherical framboids of pyrite; and (E): highly crystalline pyrite at a high resolution.

directions (Figure 7.2E). Fe/S ratios, elemental composition, and mineral morphology along with XRD results were applied to identify iron mineral coatings. Other species of iron sulfide such as mackinawite (FeS) and greigite (Fe_3S_4) were not detected in samples from the Cryo Core.

7.3 Quench Study Iron Sulfide Mineral Coatings Comparison

7.3.1 Liquid Nitrogen Quench Study

The objective of the cryogenic preservation study (referred to as a quench study) was to simulate a cryogenic collection process with samples from the Anaerobic Core to better understand the impact of a liquid nitrogen quench on the formation and transformation of iron mineral surface coatings. Two subsamples from the Anaerobic Core were selected for the quench study at depths with relatively high iron and sulfur concentrations and unique iron mineral coatings. The sample located at 4.27 m DBS within the first RTZ[124] referred to as Sample 2-10 was observed with abundant iron sulfide mineral coatings primarily comprised of framboidal pyrite and greigite. Another sample, which is referred to as Sample 7-1 (6.8 m DBS, second RTZ), was found to contain abundant mackinawite with small quantities of pyrite and pyrrhotite. Samples 2-10 and 7-1 were split and studied with and without quenching. All quenched sediments (approximately 10 g) were transferred into plastic centrifuge tubes in individual heat-sealing Mylar bags, and then bathed in liquid nitrogen (77 K) for one hour. Subsequently, samples were thawed in the glovebox and further probed with FESEM/EDX analysis. The surface composition and coating morphology of reactive iron minerals were compared between sets of samples.

7.3.2 Iron Sulfide Mineral Coatings Comparison in Quench Study

After comparing samples from the Anaerobic Core with and without quenching using FESEM/EDX, some inconsistencies in mineral morphology and surface mineral species were observed. For example, spherical framboidal greigite was abundant in Sample 2-10 (Figure 7.3A and C). However, for samples with and without quenching, even though the atomic ratios of Fe:S (0.61 and 0.69 for Figure 7.3A and C, respectively) are close to the stoichiometry of greigite (Fe_3S_4), a difference is observed in the morphology of greigite: the structure of greigite particles in the framboid can be recognized in the sample without quenching (Figure 7.3A), while it is no longer observed after quenching (Figure 7.3C). For pyrite coatings observed in Sample 7-1 (Figure 7.3B and D), the characteristic cubic and, to a lesser extent, octahedral structures were found without quenching (Figure 7.3B), which was also found in the previous study at this depth.[124] However, in samples after quenching, the crystalline pyrite was observed to a much smaller extent; even in samples with the atomic ratio of Fe:S, the usual crystalline structure was not present (Figure 7.3D). Other metastable iron sulfides identified through S elemental mapping, including mackinawite (FeS), were abundant in Samples 2-10 and 7-1 without quenching (Figure 7.3E and F); however, after quenching these minerals were no longer found (Figure 7.3G and H). Instead, mapping revealed an increase in potential pyrite based on composition, although again the characteristic morphology was lost (Figure 7.3G). This phenomenon is similar to the observation in the Cryo Core, where mackinawite was not found and only pyrite was detected in the iron sulfide mineral coatings. Pyrite found in the quenched anaerobic samples increased by comparing coatings under the same magnification using

Anaerobic Samples without Quenching

FESEM/EDX

Element	Atomic%
O K	30.56
Si K	1.46
S K	41.50
Fe K	25.21

Element	Atomic%
O K	43.82
Al K	3.36
Si K	4.98
S K	30.59
Fe K	17.25

Anaerobic Samples after Quenching

FESEM/EDX

Element	Atomic%
O K	24.76
Al K	2.65
Si K	3.31
S K	41.04
Fe K	28.24

Element	Atomic%
O K	33.65
Al K	1.95
Si K	2.91
S K	40.80
Fe K	19.47

EDX Mapping

S Ka1   Fe Ka1
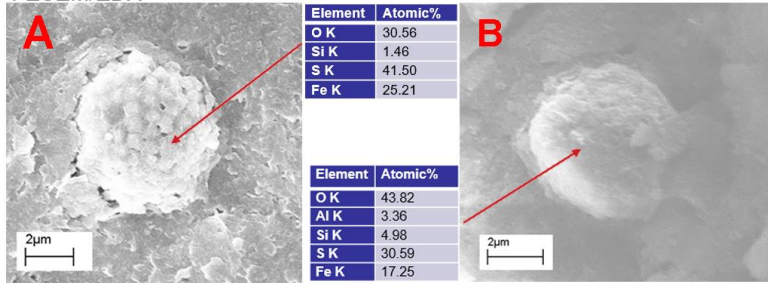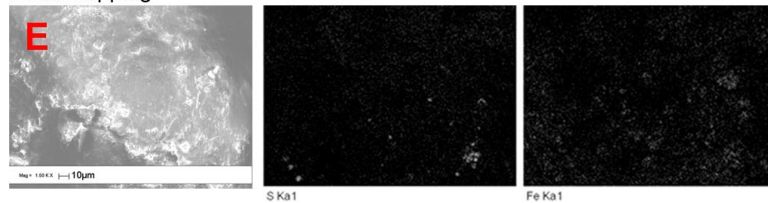
EDX Mapping in Earlier Work

S Ka1   Fe Ka1

EDX Mapping

S Ka1   Fe Ka1

S Ka1   Fe Ka1
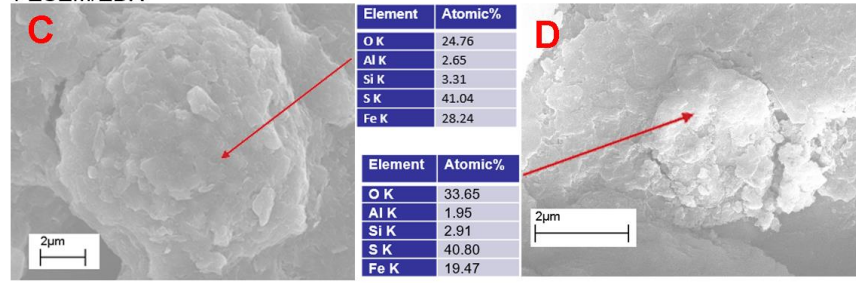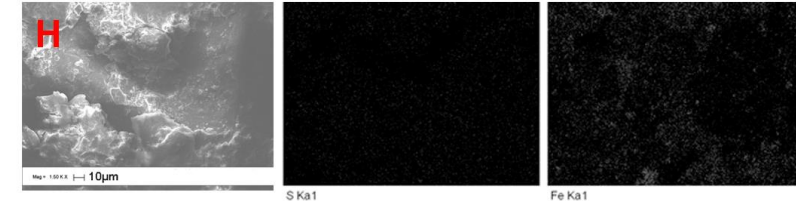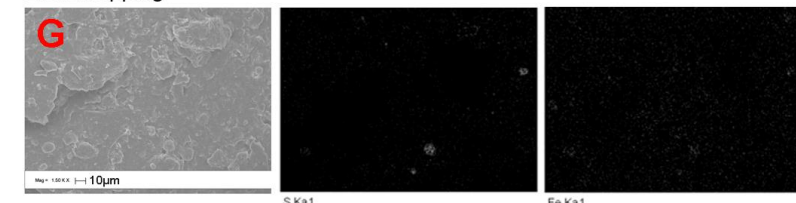
Figure 7.3 Results for the cryogenic quench study with anaerobic samples. For samples without quenching, morphology and elemental distribution of observed coatings: greigite (A) and pyrite (B), are presented, as well as elemental mappings of S and Fe on bulk mineral surface (E); (F) shows elemental mappings from earlier work for consistency; After quenching, the same characterizing process has been done for greigite and pyrite coatings shown in (C) and (D); (G) and (H) are elemental mappings for comparison.

the FESEM/EDX mapping. The differences in morphologies and mineral composition may be attributed to the quenching process.

7.4 Formation and Transformation of Iron Sulfides in the Cryo Core

In anaerobic systems, iron sulfides have been observed in sediments as mineral coatings [1]. Dissolved iron in the pore water can result from the chemical and biological reduction of Fe(III) oxyhydroxides and iron-bearing clay minerals adsorbed on the surface of detrital silicates.[59, 171] On the other hand, sulfides result from bacterial reduction of sulfate and may be found as H_2S, HS^-, S^0, and polysulfides.[172, 173] Because iron sulfides are sparingly soluble, iron(II) monosulfide initially precipitates from the aqueous phase.[174] The stability of precipitated mackinawite in groundwater can be evaluated with the following reactions:

$$FeS_{makinawite} + 2H^+ \rightarrow Fe^{2+} + H_2S \text{ (when pH < 7), or} \tag{7.1}$$

$$FeS_{makinawite} + H^+ \rightarrow Fe^{2+} + HS^- \text{ (when pH > 7)} \tag{7.2}$$
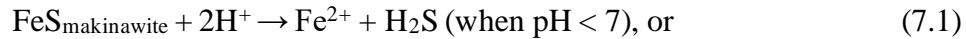
Rickard[175] reported the equilibrium constant $K_{sp(mackinawite)}$ for Reaction (7.1) is $10^{3.5}$ and $K_{sp(mackinawite)}$ for Reaction (7.2) is $10^{-3.5 \pm 0.25}$ between pH of 3 and 10, and $\sum[S(-II)]$ 10^{-6} to 10^{-1} M at 23 °C. Based on geochemical conditions reflected in the MLS data (Table 7.1), the formation of mackinawite is possible. Moreover, considering the complexity and inhomogeneity of sediment, mackinawite is expected to precipitate under the current geochemical conditions (plus the potential contribution from sulfate reducing bacteria[176]). Subsequent transformation results in potentially one of several metastable forms including mackinawite (FeS) and greigite (Fe_3S_4), as well as more stable forms such as pyrite (FeS_2) and pyrrhotite ($Fe_{1-x}S$). Iron monosulfides such as mackinawite can react with H_2S[177, 178] or S^0 (including polysulfides)[179-181] to form pyrite under oxygen-free conditions. Butler

Table 7.1 Multi-Level System (MLS) Ground Water Data and Geochemistry Screening Data for the Cryo Core (8.23 m to 9.45 m DBS)

Parameter Category	Result	Units	Analytical Method
Nitrate nitrogen (dissolved)	0.0046	mg/L	EPA Method 353.2
Ammonia nitrogen	4.5	mg/L	4500-NH_3 B/C modified-1997
Chloride (titrimetric)	512	mg/L	4500-Cl C-1997
Sulfate (dissolved)	200	mg/L	EPA 300
Sulfide	0.054	mg/L	3500-S2 D-2000
Total alkalinity	203	mg $CaCO_3$	2320 B-1997
Total phosphorus as PO_4 (dissolved)	0.25	mg/L	EPA 365.1
Iron (dissolved)	59.6	mg/L	EPA 6010B
Magnesium (dissolved)	50.7	mg/L	EPA 6010B
Manganese (dissolved)	3.91	mg/L	EPA 6010B
Calcium (dissolved)	62.2	mg/L	EPA 6010B
Sodium (dissolved)	344	mg/L	EPA 6010B
pH in ground water	6.59	-	EPA 150.3
pH in sediment	5.0 - 7.1 (ave. 6.4)	-	Burt, 2014[75]
ORP in sediment	90.9 - 598.2 (ave. 211.0)	mV	Yu and Rinklebe, 2013[73]
Iron in sediment	7.3 – 66.6 (ave. 25)	1000 ppm	EPA 6200
Sulfur in sediment	0.4 – 11.9 (ave. 2.9)	1000 ppm	EPA 6200

and Rickard[90] demonstrated another pathway to form framboidal pyrite through redox-dependent abiotic reactions using FeS and H_2S which has been demonstrated in previous chapters. Although mackinawite and greigite are not necessarily prerequisite minerals for pyrite formation,[182] in groundwater systems at ambient temperature and relatively low dissolved concentrations of Fe and S, these iron sulfides can be referred to as "precursors" in sediment. The precursor pathways are consistent with the presence of iron sulfides in the Anaerobic Core where pyrite, mackinawite, and greigite were abundant (Figure 7.3).

Morphologies of pyrite identified in the Cryo Core (Figure 7.2) can be considered as crucial indicators of geochemical conditions in mineral nucleation and growth. Based on the work of Wilkin and Barnes[182], Butler and Rickard[90] reported that framboidal and single pyrite grains were directly formed as products of mackinawite oxidation by H_2S in anaerobic aqueous solutions at pH 6 and temperatures ranging from 60 °C to 140 °C. They reported that the framboidal texture results from rapid nucleation under supersaturated conditions, while single pyrite crystals are generated at or below saturation with slow nucleation. Framboidal pyrite can also be indirectly formed through FeS transformation to framboidal greigite (Fe_3S_4) as an intermediate resulting in spherical framboidal pyrite (Figure 7.2 D).[129] Framboidal greigites have been found in numerous studies,[183, 184] and their potential transformation to pyrite was demonstrated with synchrotron-based energy dispersive X-ray diffraction (ED-XRD).[87] Greigite was reported to have been found in natural sediment of near-shore, shoreline, and fresh water systems,[90, 95] which may be associated with a sharp redox gradient under Fe- and S-rich conditions. As a result, framboidal pyrite via intermediate framboidal greigite may be another possible pathway for pyrite framboids to form as observed in the Cryo Core. A unique aggregated crystalline

pyrite structure of interpenetrated grains (Figure 7.2B and E) was classified as another framboidal structure formed through rapid crystal growth at this location.[185] In redox-active systems, pyrites are oxidized to Fe(III) species through biotic or abiotic pathways as iron cycling of sediment systems.[186-189] However, neither mackinawite nor greigite, common precursors of pyrite, were observed morphologically across the entire Cryo Core set of samples. For comparison, Sample 7-1 (6.8 m DBS) from the Anaerobic Core and the zone of focus in the Cryo Core (8.48 to 8.64 m DBS) both revealed elevated concentrations of Fe and S in sediment with gradients in the redox condition. While mackinawite was found to be the most dominant iron sulfide coating along with cubic euhedral pyrite in Sample 7-1 (Figure 7.3B, E, and F), framboidal pyrite was only detected in sediments around Sample 2-10 (4.27 m DBS) generally abutting framboidal greigite. The unique mineralogy of the cryogenically preserved core indicates the potential impacts of the cryogenic process.

7.5 The Impact from Pore Water Freezing Effect

To explain the absence of mackinawite and greigite in the Cryo Core, as well as the mineralogical difference between split Anaerobic Core samples in quench study, the pore water freezing mechanism may be responsible. During quenching, the unfrozen solute trapped in ice junctions (also known as "micropockets") is concentrated from the surrounding growing ice crystals, as some solutes are not incorporated into the increasing ice structure. The inequality of anions and cations at the ice and solute interface generates a freezing potential; it has been reported to range from -90 to +210 V depending on the size and structure of the ion.[165, 190] For example, when a diluted NaCl system is freezing, the trapped ions in the micropockets are concentrated during the development of ice. At

the ice-water interface, the ice lattice observed preferentially incorporates Cl^- over Na^+, which is based on the sizes and structures of the ions causing minimum readjustment of the ice lattice,[166, 190] the excess of Na^+ as a counterion accumulates in the aqueous phase at the interface. Theoretically, Cl^- ions in the ice are neutralized by H_3O^+, and OH^- ions move in the electric field to the interface to neutralize ions on the solute side. The buildup of Na^+ and OH^- ions in the double layer at the ice-water interface results in a concentrated solution in these micropockets, which is alkaline. In the Cryo Core groundwater, MLS data (Table 7.1) show the highest concentration of ions (pH = 6.4) are chloride (512 mg/L), sodium (344 mg/L), sulfate (200 mg/L), iron (59.6 mg/L), and calcium (62.2 mg/L). In a system with large anions such as SO_4^{2-}, the anions accumulate to a greater degree in the aqueous phase while a smaller counterion such as sodium creates a larger positive potential in ice at the interface than the negative potential brought by halides systems (the ammonium cation is one exception,[162] however, its concentration is much lower than sulfate in this case). Therefore, at the ice-water interface, the freezing potential results in a negative charge in the solute compared to the ice when pore water started to freezing. H_3O^+ ions from the ice phase migrate across the interface to neutralize the negative charge, resulting in acidification of the (unfrozen) pore water in micropockets. As a result, during the freezing process of the anaerobic sediment, the unfrozen pore water in these micropockets potentially becomes locations with elevated electrolyte concentrations and lower pH compared to the initial condition.

A freezing potential mechanism leading to a lower pore water pH may explain the phenomena observed in the quench study. Because the stability of iron sulfide can be reduced under acidic conditions based on Reaction (7.1), the dissolution of mackinawite is

dependent on the H^+ concentration in an acidic solution (defined as pH less than 5.3[175]), and is pH-independent at neutral to alkaline conditions.[175, 191, 192] The lowest pH measured in groundwater was 5.0 (Table 7.1), but it could be lower during quenching because of the freezing potential. The precipitated mackinawite on the bulk mineral surfaces becomes more soluble in acidified solutions with the dissolution of $Fe(H_2O)_6^{2+}$ and $H_2S^o_{(aq)}$. Simultaneously, concentrations of reduced iron and sulfur ions increases in the (ion concentrated) solution found at the interface of the ice. As a result of freezing potential and freezing-concentration mechanisms, the concentrated reduced iron and sulfur ions in the micropockets enhances the reprecipitation of nano-sized pyrite (FeS_2).[179] This mechanism may surpass the negative impact brought on by the low temperature and explains why mackinawite is not observed in the Cryo Core and quenched samples but is abundant in unquenched samples. Consequently, reprecipitated pyrites form within a shorter time period, yet the time is insufficient to develop observable typical cubic and octahedral crystalline structures as observed in sediment cores. This mechanism also explains why the iron sulfide coatings have the same surface composition as pyrite after being quenched, but do not exhibit the distinguishable crystalline morphology. Moreover, the morphology of framboidal greigite (Fe_3S_4) in Sample 2-10 (Figure 7.3C) changes: the crystalline structure is lost after the cryogenic quench while the surface composition and the spherical shape of framboids remain intact. The cryogenic process may dissolve a surface layer of greigite but not impact mineralogy. For pyrite coatings, their characteristically cubic and octahedral morphologies appear to remain intact in the Cryo Core. After the quench study, however, precipitates of pyrite in the Anaerobic Core were found to have increased to some extent as nanoscale coatings lacking the characteristic morphology. For most iron oxyhydroxide

minerals detected with FESEM/EDX in both the Cryo Core and the quenched Anaerobic Core samples remained intact, the impact of liquid nitrogen may be related to iron mineral solubility in acidic groundwater where mackinawite > greigite > pyrite ≥ most Fe(III) oxyhydroxides.

7.6 Summary

A set of analyses has been applied to study the mineralogy and morphology of reactive iron mineral coatings in a sediment core with a cryogenic collection system. XRD analysis was applied to probe iron mineral species, while FESEM/EDX analyses provide micro- to nano-resolution data about mineral coating composition and morphology. Sharp redox gradients were found (discussed above) between geological layers by characterizing iron mineral coatings. Among the identified reactive iron minerals, pyrite was abundant in the section of 8.33 to 9.45 m DBS. However, after comparing identified surface mineral coatings to a previously collected Anaerobic Core at an adjacent location, the two most important iron sulfide "precursors" of pyrite, mackinawite and greigite, were not found in the Cryo Core but were ubiquitous in RTZs of the (unquenched) Anaerobic Core. These results are not consistent with potential transformation pathways for iron sulfides in RTZs of sediments. By conducting a cryogenic quench study at 77 K on split samples from the Anaerobic Core, mackinawite was observed to decrease while pyrite increased; overall morphological information on surface coatings was also lost. These phenomena can be explained by a mackinawite dissolution, transformation, and reprecipitation process during the freezing process driven by mechanisms of freezing-concentration and freeze potential in the cryogenic process. Impacts from a cryogenic quench are found to depend on the

thermodynamic stability of mineral coatings in groundwater. The results of the quench study also provide evidence that the cryogenic sampling technique for collecting sediment samples may result in a loss of mineralogy and morphology of metastable forms of iron sulfide coatings. Because these metastable forms of iron sulfide minerals have high reactivity in dechlorination reactions within groundwater systems, the natural attenuation of chlorinated compounds may be underestimated.

For on-site sediment sampling, cryogenic preservation of cores is considered a robust method for sediment collection with pore fluids, allowing for the preservation of contaminants as well as microbial ecology. However, caution should be taken when using the cryogenic process for samples bearing redox-sensitive minerals. The change and transition in redox conditions potentially depend on the surface coating mineralogy, solute speciation, and concentration in pore water, as well as the freezing rate.[167]

CHAPTER 8

CONCLUSIONS AND FUTURE WORK

To better understand iron and sulfur cycling in the anaerobic environment and natural attenuation of a contaminated site, an anaerobic 18-m sediment core was collected with an adapted biogeochemical coring system and studied from cm to nm scale resolution with redox conditions preserved. By utilizing screening results such as XRF, VOCs in the headspace, sediment pH and ORP, as well as abundant bacteria in subsampled anaerobic sediment, potential RTZs in this Anaerobic Core were identified and expected to be critical areas for the further mineral coating characterization with higher resolution. A set of analyses was developed and applied to investigate mineralogy, morphology, and surface composition of iron mineral coatings with XRD and FESEM/EDX. Among the five RTZs, the Upper Zone and Zone 1 were found to be abundant in reactive iron mineral coatings. Additionally, given the unique morphologies observed in the two transition zones, the Upper Zone and Zone1, distinct transformation pathways were found for pyrite formation. With framboidal greigite observed abundantly in the Upper Zone, the formation of framboidal pyrite from mackinawite with greigite as an intermediate is expected to be the dominant pathway for iron sulfide transformation. However, in Zone 1, transformation pathways of iron sulfides without the presence of greigite are likely to involve mackinawite reacting either with S_0, polysulfides, and other S intermediates, or dissolved H_2S to form pyrite. Along with evidence from sequential extraction, groundwater chemistry, and dominant microbial groups, these two RTZs are expected to support self-sustaining natural attenuation processes through the redox cycling of iron reactive minerals.

In contrast to Zone 1, Zone 2 is in the aquifer below the NAPL-bearing area where a high concentration of iron mineral coatings is observed. However, concentrations of Fe mineral coatings drop steeply as a function of depth. S concentrations were not observed and morphologically the most abundant mineral coatings were the Fe(III) oxyhydroxides. Sulfur is most rich in the aqueous phase as sulfate. Although dominant OTUs are *Geobacter* and *Acidovorax*, iron sulfides are not observed. While these genera are known degraders of contaminants using reactive iron minerals as an electron donor/acceptor, the continuously decreasing iron concentration profile is expected to limit biotic processes in this zone. In Zone 3, the gradients in oxidized/reduced mineral coatings are mainly due to the poor mass transfer in this clay layer and the high concentration of dissolved oxygen brought from the abutting groundwater. This zone is considered to have a significant gradient in the redox potential; however, it is not evident that there is an attenuation of COCs.

Future work associated with this research should include studies focused on further characterization of hydrological conditions, sediment properties, and natural attenuation processes. Because sediments are complex and affected by both biotic and abiotic processes at the same time, the data collected from critical zones will eventually help to better understand contaminant fate, transport, and exposure in the environment. More research is needed to quantitatively evaluate biotic/abiotic contributions and related reaction rates in each step of attenuation processes. Using the methodology developed in this research along with results from studies probing COC degradation, this work provides the foundation for identifying where natural attenuation is most significant, applying

abiotic processes in remediating sites, and promoting RTZs in subsurface remediation to enhance degradation of contaminants.

In studies comparing reactive iron coatings between the Cryo Core and the Anaerobic Core, the two most important iron sulfide "precursors" of pyrite, mackinawite, and greigite, were not found in the Cryo Core. However, pyrite, is a dominant iron sulfide mineral coating, abundant in the zones of interest and present in different morphologies. Interestingly, the quench study with split subsamples from the Anaerobic Core showed that pyrite concentrations increased while the characteristic morphological features were lost on the bulk mineral surfaces and mackinawite was no longer found. These phenomena may be explained by mackinawite dissolution into acidified groundwater trapped in ice gaps with H^+ release from surrounding ice referred to as the freezing potential mechanism, and then reprecipitated as nano-sized pyrite in the freezing-concentration mechanism. The experimental results indicated that cryogenic coring may affect redox-sensitive iron sulfide mineralogy during the sample quenching process. Further studies are needed to better evaluate these potential freezing factors under different geochemical conditions.

APPENDIX A

XRD DIFFRACTOGRAMS FOR THE UPPER ZONE AND ZONE 1

XRD diffractograms collected from sediment samples in the Upper Zone and Zone 1.
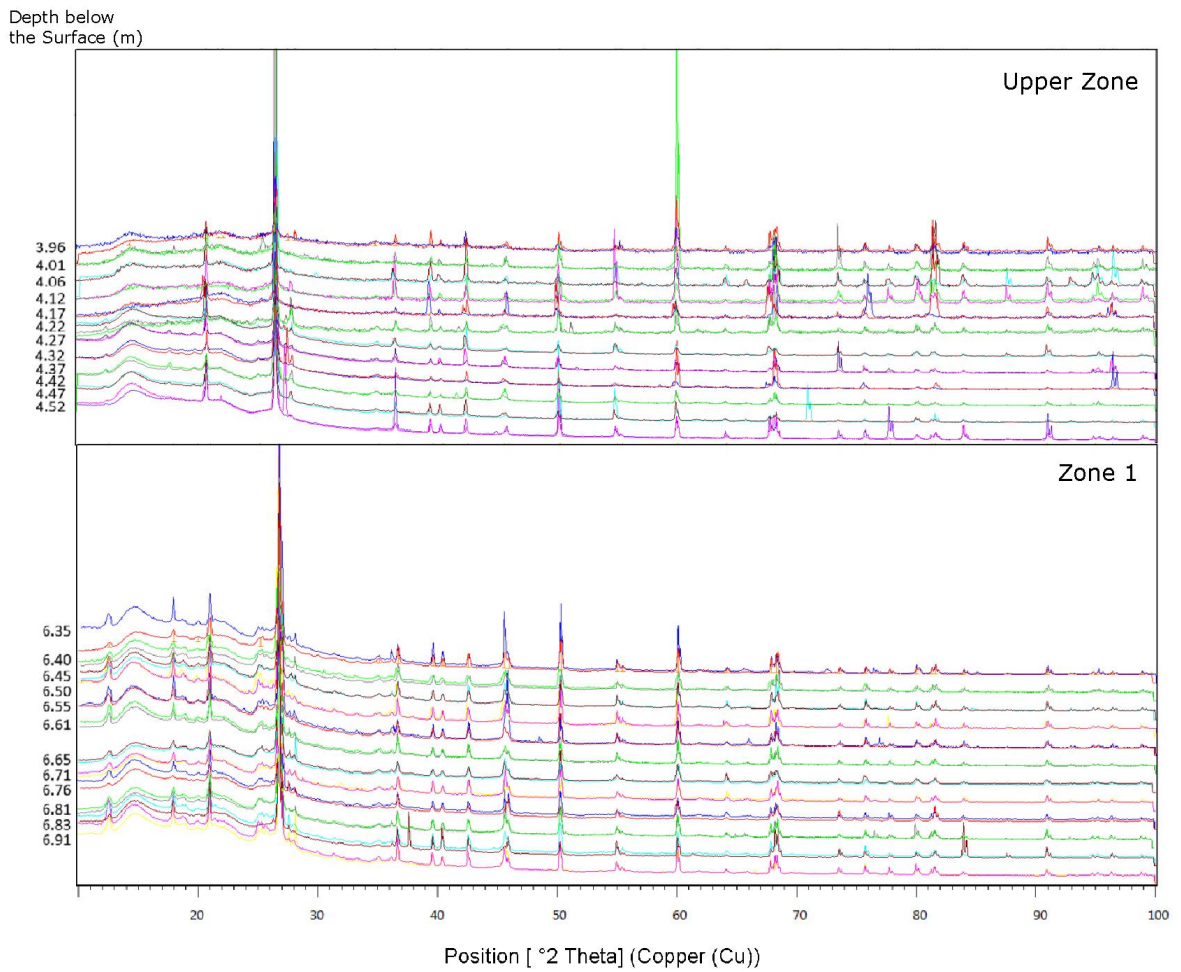
In XRD diffractograms, clay minerals in Zone2, clay minerals decreased as a function of depth. In Zone 3, highly dense kaolinite was found as a new bulk clay mineral.
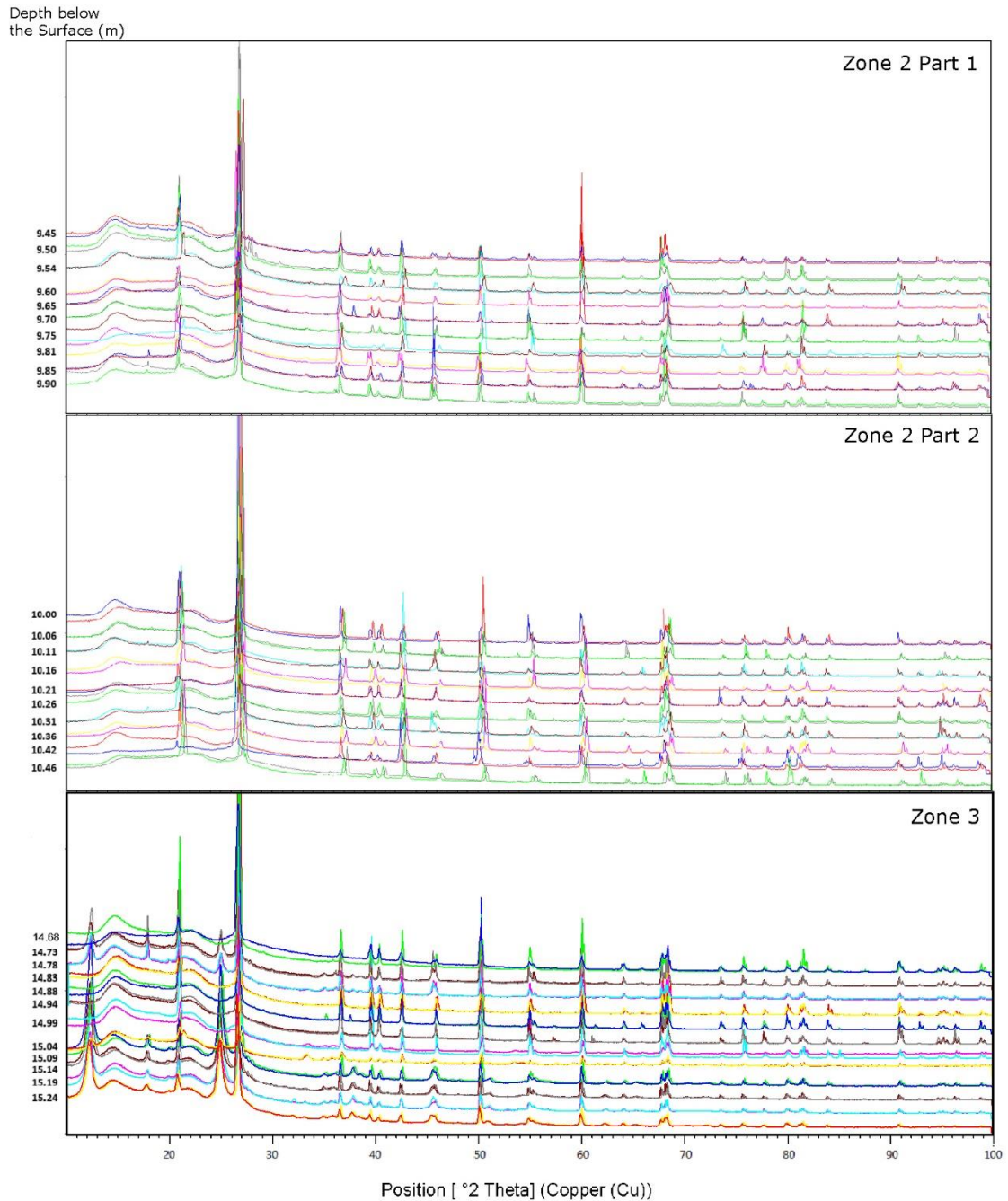
APPENDIX C

PROFILES OF DISSOLVED OXYGEN AND PH IN GROUNDWATER

The concentration of dissolved oxygen in groundwater peaked at Zone 3 where was the transition area between a thin clay player and a groundwater layer. Although pH in the sediment changed very little, groundwater at Zone 1 showed a relatively reduced condition.
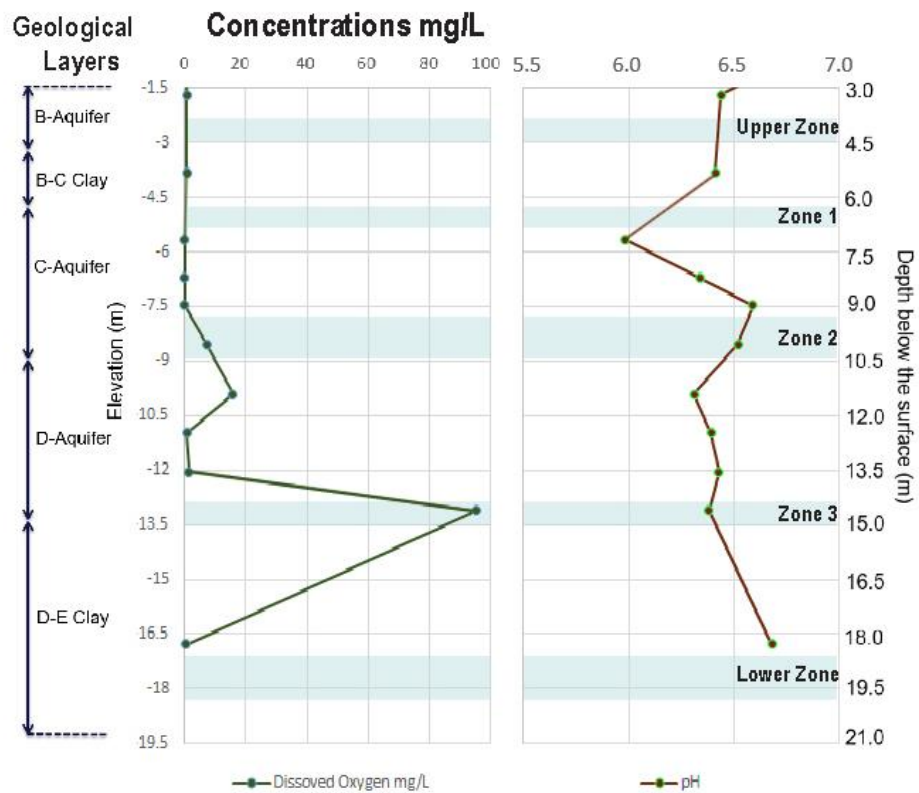
APPENDIX D

XRD DIFFRACTOGRAMS FOR CRYO CORE

XRD diffractograms with peak identification for Zone of interest.
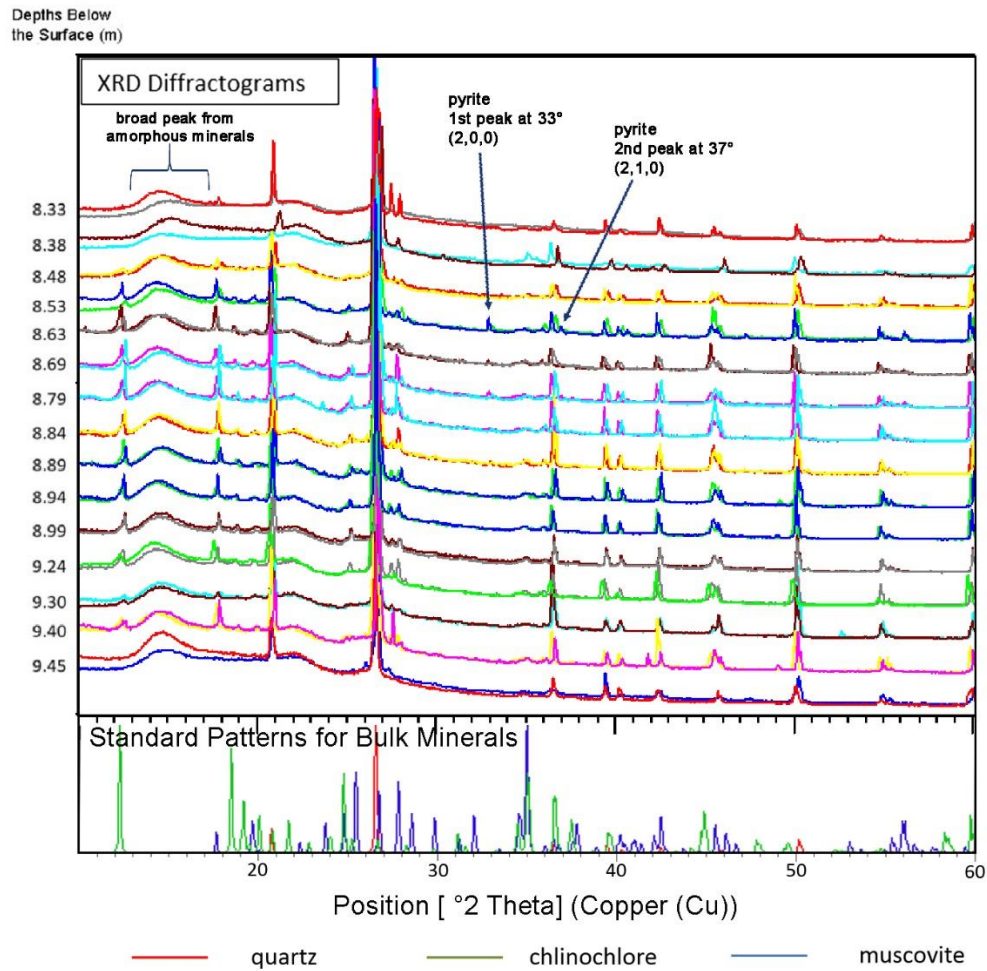
REFERENCES

1.   He, Y.; Su, C.; Wilson, J.; Wilkin, R.; Adair, C.; Lee, T.; Bradley, P.; Ferrey, M. Identification and characterization methods for reactive minerals responsible for natural attenuation of chlorinated organic compounds in ground water; U.S. Environmental Protection Agency, Washington, DC, EPA/600/R-09/115, **2009**.

2.   Rickard, D.; Luther, G. W., Chemistry of iron sulfides. *Chem. Rev.* **2007,** *107*, (2), 514-562.

3.   Landis, R.; Hua, H.; Yin, X.; Axe, L.; Morgan, S., Biogeochemical coring and preservation method for unconsolidated soil samples. under review.

4.   McCaulou, D. R.; Jewett, D. G.; Huling, S. G. Nonaqueous phase liquids compatibility with materials used in well construction, sampling, and remediation. US Environmental Protection Agency, Office of Research and Development, Office of Solid Waste and Emergency Response. Ground Water Issue **1995**.

5.   DNAPL remediation: Selected projects approaching regulatory closure; U.S. Environmental Protection Agency: **2004**.

6.   Clement, T. P.; Truex, M. J.; Lee, P., A case study for demonstrating the application of US EPA's monitored natural attenuation screening protocol at a hazardous waste site. *J. Contam. Hydrol.* **2002,** *59*, (1-2), 133-162.

7.   Rivett, M. O.; Wealthall, G. P.; Dearden, R. A.; McAlary, T. A., Review of unsaturated-zone transport and attenuation of volatile organic compound (VOC) plumes leached from shallow source zones. *J. Contam. Hydrol.* **2011,** *123*, (3-4), 130-156.

8.   Bradley, P. M.; Chapelle, F. H., Kinetics of DCE and VC mineralization under methanogenic and Fe(III)-reducing conditions. *Environ. Sci. Technol.* **1997,** *31*, (9), 2692-2696.

9.   Lee, M.; Odom, J.; Buchanan Jr, R., New perspectives on microbial dehalogenation of chlorinated solvents: insights from the field. *Annu. Rev. Microbiol.* **1998,** *52*, (1), 423-452.

10.   Morel, F.; Price, N., The biogeochemical cycles of trace metals in the oceans. *Science* **2003,** *300*, (5621), 944-947.

11.   Jickells, T.; An, Z.; Andersen, K. K.; Baker, A.; Bergametti, G.; Brooks, N.; Cao, J.; Boyd, P.; Duce, R.; Hunter, K., Global iron connections between desert dust, ocean biogeochemistry, and climate. *Science* **2005,** *308*, (5718), 67-71.

12. Lovley, D. R., Fe (III) and Mn (IV) reduction. In *Environmental microbe-metal interactions*, American Society of Microbiology, Washington, DC **2000**; pp 3-30.

13. Thamdrup, B., Bacterial manganese and iron reduction in aquatic sediments. In *Advances in microbial ecology*, Springer Boston, MA: 2000; pp 41-84.

14. Vogel, T. M.; Criddle, C. S.; McCarty, P. L.; Arcos, J. C., Transformations of halogenated aliphatic compounds: Oxidation, reduction, substitution, and dehydrohalogenation reactions occur abiotically or in microbial and mammalian systems. *Environ. Sci. Technol.* **1987,** *21*, (8), 722-736.

15. Davis, J. A.; Hayes, K. F., *Geochemical processes at mineral surfaces*. American Chemical Society Washington, DC: **1986**.

16. Johnson, T. L.; Scherer, M. M.; Tratnyek, P. G., Kinetics of halogenated organic compound degradation by iron metal. *Environ. Sci. Technol.* **1996,** *30*, (8), 2634-2640.

17. Gillham, R. W.; O'Hannesin, S. F., Enhanced degradation of halogenated aliphatics by zero-valent iron. *Groundwater* **1994,** *32*, (6), 958-967.

18. Matheson, L. J.; Tratnyek, P. G., Reductive dehalogenation of chlorinated methanes by iron metal. *Environ. Sci. Technol.* **1994,** *28*, (12), 2045-2053.

19. O'Hannesin, S. F.; Gillham, R. W., In situ degradation of halogenated organics by permeable reaction wall. *Ground Water Currents* **1993**.

20. Wilkin, R. T.; Puls, R. W. *Capstone report on the application, monitoring, and performance of permeable reactive barriers for ground-water remediation: Volume 1: Performance evaluations at two sites*; Technical Report No. EPA/600/R-03/045A; U.S. Environmental Protection Agency: Cincinnati, OH, **2003**.

21. Tratnyek, P. G.; Scherer, M. M.; Johnson, T. L.; Matheson, L. J., Permeable reactive barriers of iron and other zero-valent metals. *Environ. Sci. Pollut. Control Ser.* **2003**, 371-422.

22. Butler, E. C.; Hayes, K. F., Effects of solution composition and pH on the reductive dechlorination of hexachloroethane by iron sulfide. *Environ. Sci. Technol.* **1998,** *32*, (9), 1276-1284.

23. Butler, E. C.; Hayes, K. F., Kinetics of the Transformation of Trichloroethylene and Tetrachloroethylene by Iron Sulfide. *Environ. Sci. Technol.* **1999,** *33*, (12), 2021-2027.

24. Liang, X.; Dong, Y.; Kuder, T.; Krumholz, L. R.; Philp, R. P.; Butler, E. C., Distinguishing abiotic and biotic transformation of tetrachloroethylene and trichloroethylene by stable carbon isotope fractionation. *Environ. Sci. Technol.* **2007,** *41*, (20), 7094-7100.

25. Butler, E. C.; Hayes, K. F., Factors influencing rates and products in the transformation of trichloroethylene by iron sulfide and iron metal. *Environ. Sci. Technol.* **2001,** *35*, (19), 3884-3891.

26. Jeong, H. Y.; Kim, H.; Hayes, K. F., Reductive dechlorination pathways of tetrachloroethylene and trichloroethylene and subsequent transformation of their dechlorination products by mackinawite (FeS) in the presence of metals. *Environ. Sci. Technol.* **2007,** *41*, (22), 7736-7743.

27. Zwank, L.; Elsner, M.; Aeberhard, A.; Schwarzenbach, R. P.; Haderlein, S. B., Carbon isotope fractionation in the reductive dehalogenation of carbon tetrachloride at iron (hydr) oxide and iron sulfide minerals. *Environ. Sci. Technol.* **2005,** *39*, (15), 5634-5641.

28. Choi, J.; Choi, K.; Lee, W., Effects of transition metal and sulfide on the reductive dechlorination of carbon tetrachloride and 1, 1, 1-trichloroethane by FeS. *J. Hazard. Mater.* **2009,** *162*, (2-3), 1151-1158.

29. Gander, J. W.; Parkin, G. F.; Scherer, M. M., Kinetics of 1, 1, 1-trichloroethane transformation by iron sulfide and a methanogenic consortium. *Environ. Sci. Technol.* **2002,** *36*, (21), 4540-4546.

30. Butler, E. C.; Hayes, K. F., Kinetics of the transformation of halogenated aliphatic compounds by iron sulfide. *Environ. Sci. Technol.* **2000,** *34 (3)*, 422–429.

31. Lee, W.; Batchelor, B., Abiotic reductive dechlorination of chlorinated ethylenes by iron-bearing soil minerals. 1. Pyrite and magnetite. *Environ. Sci. Technol.* **2002,** *36*, (23), 5147-5154.

32. Kriegman-King, M. R.; Reinhard, M., Transformation of carbon tetrachloride in the presence of sulfide, biotite, and vermiculite. *Environ. Sci. Technol.* **1992,** *26*, (11), 2198-2206.

33. Lee, W.; Batchelor, B., Abiotic reductive dechlorination of chlorinated ethylenes by iron-bearing soil minerals. 2. Green rust. *Environ. Sci. Technol.* **2002,** *36*, (24), 5348-5354.

34. Ferrey, M. L.; Wilkin, R. T.; Ford, R. G.; Wilson, J. T., Nonbiological removal of cis-dichloroethylene and 1,1-dichloroethylene in aquifer sediment containing magnetite. *Environ. Sci. Technol.* **2004,** *38*, (6), 1746-1752.

35.	He, Y.; Wilson, J.; Su, C.; Wilkin, R., Review of abiotic degradation of chlorinated solvents by reactive iron minerals in aquifers. *Groundwater Monitoring & Remediation* **2015,** *35*, (3), 57-75.

36.	Davis, A.; Fennemore, G.; Peck, C.; Walker, C.; McIlwraith, J.; Thomas, S., Degradation of carbon tetrachloride in a reducing groundwater environment: implications for natural attenuation. *J. Appl. Geochem.* **2003,** *18*, (4), 503-525.

37.	Kenneke, J. F.; Weber, E. J., Reductive dehalogenation of halomethanes in iron- and sulfate-reducing sediments. 1. Reactivity pattern analysis. *Environ. Sci. Technol.* **2003,** *37*, (4), 713-720.

38.	Devlin, J.; Müller, D., Field and laboratory studies of carbon tetrachloride transformation in a sandy aquifer under sulfate reducing conditions. *Environ. Sci. Technol.* **1999,** *33*, (7), 1021-1027.

39.	Darlington, R.; Lehmicke, L.; Andrachek, R. G.; Freedman, D. L., Biotic and abiotic anaerobic transformations of trichloroethene and cis-1,2-dichloroethene in fractured sandstone. *Environ. Sci. Technol.* **2008,** *42*, (12), 4323-4330.

40.	Whiting, K.; Evans, P. J.; Lebrón, C.; Henry, B.; Wilson, J. T.; Becvar, E., Factors controlling in situ biogeochemical transformation of trichloroethene: field survey. *Groundwater Monitoring & Remediation* **2014,** *34*, (3), 79-94.

41.	Kennedy, L. G.; Everett, J. W.; Becvar, E.; DeFeo, D., Field-scale demonstration of induced biogeochemical reductive dechlorination at Dover Air Force Base, Dover, Delaware. *J. Contam. Hydrol.* **2006,** *88*, (1-2), 119-136.

42.	He, Y. T.; Wilson, J. T.; Wilkin, R. T., Transformation of reactive iron minerals in a permeable reactive barrier (biowall) used to treat TCE in groundwater. *Environ. Sci. Technol.* **2008,** *42*, (17), 6690-6696.

43.	Damgaard, I.; Bjerg, P. L.; Bælum, J.; Scheutz, C.; Hunkeler, D.; Jacobsen, C. S.; Tuxen, N.; Broholm, M. M., Identification of chlorinated solvents degradation zones in clay till by high resolution chemical, microbial and compound specific isotope analysis. *J. Contam. Hydrol.* **2013,** *146*, 37-50.

44.	Heron, G.; Crouzet, C.; Bourg, A. C.; Christensen, T. H., Speciation of Fe(II) and Fe(III) in contaminated aquifer sediments using chemical extraction techniques. *Environ. Sci. Technol.* **1994,** *28*, (9), 1698-1705.

45.	Poulton, S. W.; Canfield, D. E., Development of a sequential extraction procedure for iron: implications for iron partitioning in continentally derived particulates. *Chem. Geol.* **2005,** *214*, (3-4), 209-221.

46. Jeong, H. Y.; Anantharaman, K.; Hyun, S. P.; Son, M.; Hayes, K. F., pH impact on reductive dechlorination of cis-dichloroethylene by Fe precipitates: An X-ray absorption spectroscopy study. *Water Res.* **2013,** *47*, (17), 6639-6649.

47. Han, Y.-S.; Hyun, S. P.; Jeong, H. Y.; Hayes, K. F., Kinetic study of cis-dichloroethylene (cis-DCE) and vinyl chloride (VC) dechlorination using green rusts formed under varying conditions. *Water Res.* **2012,** *46*, (19), 6339-6350.

48. Lee, T. R.; Wilkin, R. T., Iron hydroxy carbonate formation in zerovalent iron permeable reactive barriers: Characterization and evaluation of phase stability. *J. Contam. Hydrol.* **2010,** *116*, (1-4), 47-57.

49. Chen, C.; Puhakka, J. A.; Ferguson, J. F., Transformations of 1,1,2,2-tetrachloroethane under methanogenic conditions. *Environ. Sci. Technol.* **1996,** *30*, (2), 542-547.

50. De Wildeman, S.; Verstraete, W., The quest for microbial reductive dechlorination of C 2 to C 4 chloroalkanes is warranted. *Appl. Microbiol. Biol.* **2003,** *61*, (2), 94-102.

51. Goltz, M. N.; Park, J.-W.; Feng, P. P.; Young, H. C., Organic chemicals in groundwater: Modeling fate and transport. In *Water Pollution*, Springer: 2005; pp 33-63.

52. McCarty, P. L.; Reinhard, M., Biological and chemical transformations of halogenated aliphatic compounds in aquatic and terrestrial environments. In *Biogeochemistry of Global Change*, Springer: 1993; pp 839-852.

53. Field, J.; Sierra-Alvarez, R., Biodegradability of chlorinated solvents and related chlorinated aliphatic compounds. *Reviews in environmental Science and Bio/technology* **2004,** *3*, (3), 185-254.

54. Van Eekert, M. H.; Schröder, T. J.; Stams, A. J.; Schraa, G.; Field, J. A., Degradation and fate of carbon tetrachloride in unadapted methanogenic granular sludge. *Appl. Environ. Microbiol.* **1998,** *64*, (7), 2350-2356.

55. Tobiszewski, M.; Namieśnik, J., Abiotic degradation of chlorinated ethanes and ethenes in water. *Environ. Sci. Pollut. Res.* **2012,** *19*, (6), 1994-2006.

56. Mohn, W. W.; Tiedje, J. M., Microbial reductive dehalogenation. *Microbiol. Mol. Biol. Rev.* **1992,** *56*, (3), 482-507.

57. Gerkens, R. R.; Franklin, J. A., The rate of degradation of 1,1,1-trichloroethane in water by hydrolysis and dehydrochlorination. *Chemosphere* **1989,** *19*, (12), 1929-1937.

58. Stone, A. T., Reactions of extracellular organic ligands with dissolved metal ions and mineral surfaces. *Geomicrobiology: Interactions between microbes and minerals* **1997,** *35*, 309-344.

59. Poulton, S. W., Sulfide oxidation and iron dissolution kinetics during the reaction of dissolved sulfide with ferrihydrite. *Chem. Geol.* **2003,** *202*, (1-2), 79-94.

60. Pyzik, A. J.; Sommer, S. E., Sedimentary iron monosulfides: kinetics and mechanism of formation. *Geochim. Cosmochim. Acta* **1981,** *45*, (5), 687-698.

61. Rickard, D.; Morse, J. W., Acid volatile sulfide (AVS). *Mar. Chem.* **2005,** *97*, (3-4), 141-197.

62. Ionescu, D.; Heim, C.; Polerecky, L.; Thiel, V.; De Beer, D., Biotic and abiotic oxidation and reduction of iron at circumneutral pH are inseparable processes under natural conditions. *Geomicrobiol. J.* **2015,** *32*, (3-4), 221-230.

63. Tobler, N. B.; Hofstetter, T. B.; Schwarzenbach, R. P., Assessing iron-mediated oxidation of toluene and reduction of nitroaromatic contaminants in anoxic environments using compound-specific isotope analysis. *Environ. Sci. Technol.* **2007,** *41*, (22), 7773-7780.

64. Williams, A. G.; Scherer, M. M., Spectroscopic evidence for Fe(II)− Fe(III) electron transfer at the iron oxide− water interface. *Environ. Sci. Technol.* **2004,** *38*, (18), 4782-4790.

65. Roden, E. E., Microbial iron-redox cycling in subsurface environments. *Biochem. Soc. Trans.* **2012,** *40*, 1249-1256.

66. He, Y. T.; Wilson, J. T.; Wilkin, R. T., Impact of iron sulfide transformation on trichloroethylene degradation. *Geochim. Cosmochim. Acta* **2010,** *74*, (7), 2025-2039.

67. Jeong, D.; Kim, K.; Min, D. W.; Choi, W., Freezing-enhanced dissolution of iron oxides: effects of inorganic acid anions. *Environ. Sci. Technol.* **2015,** *49*, (21), 12816-12822.

68. Yin, X.; Hua, H.; Burns, R. F.; Fennell, D.; Dyer, J. A.; Landis, R.; Axe, L., Identifying redox transition zones in the subsurface from a site with historical contamination. *Sci. Total Environ.,* **2020,** https://doi.org/10.1016/j.scitotenv.2020.143105.

69. Sackett, D.; Martin, K. *EPA method 6200 and field portable X-ray fluorescence*; U.S. Environmental Protection Agency, 1998.

70. Kalnicky, D. J.; Singhvi, R., Field portable XRF analysis of environmental samples. *J. Hazard. Mater.* **2001,** *83*, (1-2), 93-122.

71. Soil, K. *Survey laboratory methods manual*; United States Department of Agriculture, Natural Resources Conservation Service, National Soil Survey Center, Kellogg Soil Survey Laboratory: **1996**.

72. Sumner, M., Measurement of soil pH: problems and solutions. *Communications in Soil Science and Plant Analysis* **1994,** *25*, (7-8), 859-879.

73. Yu, K.; Rinklebe, J., Soil redox potential and pH controllers. *Methods in Biogeochemistry of Wetlands* **2013**, 107-116.

74. Haag, W.; Wrenn, C., The PID Handbook-Theory and Applications of Direct-Reading Photoionization Detectors (PIDs), 2nd. *San Jose, CA: RAE Systems Inc* **2006**.

75. Burt, R.; Staff, S., Kellogg Soil Survey Laboratory Methods Manual. *Natural Resources Conservation Services. National Soil Survey Center,* Lincoln, Nebraska **2014**.

76. Raju, S. C.; Lagström, S.; Ellonen, P.; De Vos, W. M.; Eriksson, J. G.; Weiderpass, E.; Rounge, T. B., Reproducibility and repeatability of six high-throughput 16S rDNA sequencing protocols for microbiota profiling. *J. Microbiol. Methods* **2018,** *147*, 76-86.

77. Kozich, J. J.; Westcott, S. L.; Baxter, N. T.; Highlander, S. K.; Schloss, P. D., Development of a dual-index sequencing strategy and curation pipeline for analyzing amplicon sequence data on the MiSeq Illumina sequencing platform. *Appl. Environ. Microbiol.* **2013,** *79*, (17), 5112-5120.

78. Yin, X.; Hua, H.; Dyer, J. A.; Axe, L., Investigating reactive iron minerals cycling in redox transition zones from the site with historical contamination with sequential extraction, unpublished results.

79. Tessier, A.; Campbell, P. G.; Bisson, M., Sequential extraction procedure for the speciation of particulate trace metals. *Anal. Chem.* **1979,** *51*, (7), 844-851.

80. Larner, B. L.; Seen, A. J.; Townsend, A. T., Comparative study of optimised BCR sequential extraction scheme and acid leaching of elements in the certified reference material NIST 2711. *Anal. Chim. Acta* **2006,** *556*, (2), 444-449.

81. Scouller, R. C.; Snape, I.; Stark, J. S.; Gore, D. B., Evaluation of geochemical methods for discrimination of metal contamination in Antarctic marine sediments: A case study from Casey Station. *Chemosphere* **2006,** *65*, (2), 294-309.

82. Claff, S. R.; Sullivan, L. A.; Burton, E. D.; Bush, R. T., A sequential extraction procedure for acid sulfate soils: partitioning of iron. *Geoderma* **2010,** *155*, (3-4), 224-230.

83. Chung, F. H., Quantitative interpretation of X-ray diffraction patterns of mixtures. I. Matrix-flushing method for quantitative multicomponent analysis. *J. Appl. Crystallogr.* **1974,** *7*, (6), 519-525.

84. Kahle, M.; Kleber, M.; Jahn, R., Review of XRD-based quantitative analyses of clay minerals in soils: the suitability of mineral intensity factors. *Geoderma* **2002,** *109*, (3-4), 191-205.

85. Agarwal, U. P.; Ralph, S. A.; Baez, C.; Reiner, R. S.; Verrill, S. P., Effect of sample moisture content on XRD-estimated cellulose crystallinity index and crystallite size. *Cellulose* **2017,** *24*, (5), 1971-1984.

86. Hay, R. L.; Sheppard, R. A., Occurrence of zeolites in sedimentary rocks: An overview. *Rev Mineral Geochem* **2001,** *45*, (1), 217-234.

87. Hunger, S.; Benning, L. G., Greigite: a true intermediate on the polysulfide pathway to pyrite. *Geochem. Trans.* **2007,** *8*, (1), 1.

88. Vaughan, D. J.; Craig, J. R., *Mineral chemistry of metal sulfides*. Cambridge University Press: Cambridge, **1978**.

89. Lennie, A. R.; Vaughan, D. J., Spectroscopic studies of iron sulfide formation and phase relations at low temperatures. *Mineral Spectroscopy: A Tribute to Roger G. Burns* , Geochemical Society, Washington, D.C. **1996,** *5*, 117-131.

90. Butler, I. B.; Rickard, D., Framboidal pyrite formation via the oxidation of iron(II) monosulfide by hydrogen sulphide. *Geochim. Cosmochim. Acta* **2000,** *64*, (15), 2665-2672.

91. Yamaguchi, S.; Katsurai, T.; Z, K., Zur Bildung des ferromagnetischen Fe_3S_4. *Kolloid Zeit* **1960,** *170*, 147-149.

92. Lennie, A. R.; Redfern, S. A. T.; Schofield, P. F.; Vaughan, D. J., Synthesis and Rietveld crystal structure refinement of mackinawite, tetragonal FeS. *Mineral. Mag.* **1995,** *59*, (397), 677-83.

93. Lennie, A. R.; Redfern, S. A. T.; Champness, P. E.; Stoddart, C. P.; Schofield, P. F.; Vaughan, D. J., Transformation of mackinawite to greigite: An in situ X-ray powder diffraction and transmission electron microscope study. In *Am. Mineral.*, **1997**; Vol. 82, p 302.

94.   Wang, Q.; Morse, J. W., Pyrite formation under conditions approximating those in anoxic sediments: I. Pathway and morphology. *Mar. Chem.* **1996,** *52*, 99-121.

95.   Hilton, J., Greigite and the magnetic properties of sediments. *Limnol. Oceanogr.* **1990,** *35*, (2), 509-520.

96.   Schoonen, M. A. A.; Barnes, H. L., Reactions forming pyrite and marcasite fom solution 2. Via FeS precursors below 100 °C. *Geochim. Cosmochim. Acta* **1991,** *55*, 1505-1514.

97.   Rickard, D., Kinetics of pyrite formation by the H_2S oxidation of iron(II) monosulfide in aqueous solutions between 25 and 125 °C: The rate equation. *Geochim. Cosmochim. Acta* **1997,** *61*, (1), 115-134.

98.   Kennedy, L. G.; Everett, J. W., Microbial degradation of simulated landfill leachate: solid iron/sulfur interactions. *Advances in Environmental Research* **2001,** *5*, (2), 103-116.

99.   Neal, A. L.; Techkarnjanaruk, S.; Dohnalkova, A.; McCready, D.; Peyton, B. M.; Geesey, G. G., Iron sulfides and sulfur species produced at hematite surfaces in the presence of sulfate-reducing bacteria. *Geochim. Cosmochim. Acta* **2001,** *65*, (2), 223-235.

100.   Benning, L. G.; Wilkin, R. T.; Barnes, H., Reaction pathways in the Fe–S system below 100 °C. *Chemical Geology* **2000,** *167*, (1-2), 25-51.

101.   Schoonen, M. A.; Strongin, D. R., Catalysis of electron transfer reactions at mineral surfaces. *ChemInform* **2006,** *37*, (32).

102.   Faivre, D.; Menguy, N.; Guyot, F.; Lopez, O.; Zuddas, P., Morphology of nanomagnetite crystals: Implications for formation conditions. *Am. Mineral.* **2005,** *90*, (11-12), 1793-1800.

103.   Elsner, M.; Schwarzenbach, R. P.; Haderlein, S. B., Reactivity of Fe(II)-bearing minerals toward reductive transformation of organic contaminants. *Environ. Sci. Technol.* **2004,** *38*, (3), 799-807.

104.   Huang, J.; Dai, Y.; Liu, C.-C.; Zhang, H., Effects of second metal oxides on surface-mediated reduction of contaminants by Fe (II) with iron oxide. *ACS Earth Space Chem.* **2019,** *3*, (5), 680-687.

105.   Gorski, C. A.; Nurmi, J. T.; Tratnyek, P. G.; Hofstetter, T. B.; Scherer, M. M., Redox behavior of magnetite: Implications for contaminant reduction. *Environ. Sci. Technol.* **2010,** *44*, (1), 55-60.

106.	Vikesland, P. J.; Heathcock, A. M.; Rebodos, R. L.; Makus, K. E., Particle size and aggregation effects on magnetite reactivity toward carbon tetrachloride. *Environ. Sci. Technol.* **2007,** *41*, (15), 5277-5283.

107.	Canfield, D. E.; Raiswell, R.; Westrich, J. T.; Reaves, C. M.; Berner, R. A., The use of chromium reduction in the analysis of reduced inorganic sulfur in sediments and shales. *Chemical geology* **1986,** *54*, (1-2), 149-155.

108.	Latta, D. E.; Neumann, A.; Premaratne, W.; Scherer, M. M., Fe(II)–Fe(III) electron transfer in a clay mineral with low Fe content. *ACS Earth Space Chem.* **2017,** *1*, (4), 197-208.

109.	Rosso, K. M.; Yanina, S. V.; Gorski, C. A.; Larese-Casanova, P.; Scherer, M. M., Connecting observations of hematite (α-Fe2O3) growth catalyzed by Fe(II). *Environ. Sci. Technol.* **2010,** *44*, (1), 61-67.

110.	Morgan, S. A., Chambers Works SAB, unpublished data. *shared by AECOM* **2016**.

111.	Andreoni, V.; Cavalca, L.; Rao, M.; Nocerino, G.; Bernasconi, S.; Dell'Amico, E.; Colombo, M.; Gianfreda, L., Bacterial communities and enzyme activities of PAHs polluted soils. *Chemosphere* **2004,** *57*, (5), 401-412.

112.	Yu, J.; Liu, Q.; Liu, L.; Chen, J., Cloning and characterization of dichloromethane dehalogenase from Methylobacterium rhodesianum for dichloromethane degradation. *Bioremediat. J.* **2017,** *21*, (2), 71-80.

113.	Anderson, R. T.; Rooney-Varga, J. N.; Gaw, C. V.; Lovley, D. R., Anaerobic benzene oxidation in the Fe(III) reduction zone of petroleum-contaminated aquifers. *Environ. Sci. Technol.* **1998,** *32*, (9), 1222-1229.

114.	Coates, J. D.; Bhupathiraju, V. K.; Achenbach, L. A.; Mclnerney, M.; Lovley, D. R., Geobacter hydrogenophilus, Geobacter chapellei and Geobacter grbiciae, three new, strictly anaerobic, dissimilatory Fe(III)-reducers. *Int. J. Syst. Evol. Microbiol.* **2001,** *51*, (2), 581-588.

115.	Eriksson, M.; Sodersten, E.; Yu, Z.; Dalhammar, G.; Mohn, W. W., Degradation of polycyclic aromatic hydrocarbons at low temperature under aerobic and nitrate-reducing conditions in enrichment cultures from northern soils. *Appl. Environ. Microbiol.* **2003,** *69*, (1), 275-284.

116.	Dippon, U.; Pantke, C.; Porsch, K.; Larese-Casanova, P.; Kappler, A., Potential function of added minerals as nucleation sites and effect of humic substances on mineral formation by the nitrate-reducing Fe(II)-oxidizer Acidovorax sp. BoFeN1. *Environ. Sci. Technol.* **2012,** *46*, (12), 6556-6565.

117. Stackebrandt, E.; Sproer, C.; Rainey, F. A.; Burghardt, J.; Päuker, O.; Hippe, H., Phylogenetic Analysis of the Genus Desulfotomaculum: Evidence for the Misclassification of Desulfotomaculum guttoideum and Description of Desulfotomaculum orientis as Desulfosporosinus orientis gen. nov., comb. nov. *Int. J. Syst. Evol. Microbiol.* **1997,** *47*, (4), 1134-1139.

118. Robertson, W.; Franzmann, P.; Mee, B., Spore-forming, Desulfosporosinus-like sulphate-reducing bacteria from a shallow aquifer contaminated with gasolene. *J. Appl. Microbiol.* **2000,** *88*, (2), 248-259.

119. Zhang, J.; Ma, T.; Feng, L.; Yan, Y.; Abass, O. K.; Wang, Z.; Cai, H., Arsenic behavior in different biogeochemical zonations approximately along the groundwater flow path in Datong Basin, northern China. *Sci. Total Environ.* **2017,** *584*, 458-468.

120. Nayak, A. S.; Veeranagouda, Y.; Lee, K.; Karegoudar, T., Metabolism of acenaphthylene via 1,2-dihydroxynaphthalene and catechol by Stenotrophomonas sp. RMSK. *Biodegradation* **2009,** *20*, (6), 837.

121. Radianingtyas, H.; Robinson, G. K.; Bull, A. T., Characterization of a soil-derived bacterial consortium degrading 4-chloroaniline. *Microbiology* **2003,** *149*, (11), 3279-3287.

122. Boonchan, S.; Britz, M. L.; Stanley, G. A., Surfactant-enhanced biodegradation of high molecular weight polycyclic aromatic hydrocarbons by Stenotrophomonas maltophilia. *Biotechnol. Bioeng.* **1998,** *59*, (4), 482-494.

123. Rickard, D.; Schoonen, M. A.; Luther III, G., Chemistry of iron sulfides in sedimentary environments. In ACS Publications: **1995**.

124. Hua, H.; Yin, X.; Dyer, J. A.; Landis, R.; Axe, L., Characterizing reactive iron mineral coatings in redox transition zones. *ACS Earth Space Chem., in press* **2020**.

125. Fleischer, M.; Chao, G.; Kato, A., New mineral names: Ferrihydrite (MF). *Amer. Mineral* **1975,** *60*, 485-486.

126. Boursiquot, S.; Mullet, M.; Abdelmoula, M.; Génin, J.-M.; Ehrhardt, J.-J., The dry oxidation of tetragonal FeS_{1-x} mackinawite. *Physics and Chemistry of Minerals* **2001,** *28*, (9), 600-611.

127. Rickard, D.; Luther, G. W., Kinetics of pyrite formation by the H_2S oxidation of iron(II) monosulfide in aqueous solutions between 25 and 125°C: The mechanism. *Geochim. Cosmochim. Acta* **1997,** *61*, (1), 135-147.

128. Wilkin, R.; Barnes, H.; Brantley, S., The size distribution of framboidal pyrite in modern sediments: an indicator of redox conditions. *Geochim. Cosmochim. Acta* **1996,** *60*, (20), 3897-3912.

129. Wilkin, R.; Barnes, H., Pyrite formation by reactions of iron monosulfides with dissolved inorganic and organic sulfur species. *Geochim. Cosmochim. Acta* **1996,** *60*, (21), 4167-4179.

130. Berner, R. A., Sedimentary pyrite formation: an update. *Geochim. Cosmochim. Acta* **1984,** *48*, (4), 605-615.

131. Finster, K.; Liesack, W.; Thamdrup, B., Elemental sulfur and thiosulfate disproportionation by Desulfocapsa sulfoexigens sp. nov., a new anaerobic bacterium isolated from marine surface sediment. *Appl. Environ. Microbiol.* **1998,** *64*, (1), 119-125.

132. Canfield, D. E.; Thamdrup, B.; Fleischer, S., Isotope fractionation and sulfur metabolism by pure and enrichment cultures of elemental sulfur‐disproportionating bacteria. *Limnol. Oceanogr.* **1998,** *43*, (2), 253-264.

133. Donald, R.; Southam, G., Low temperature anaerobic bacterial diagenesis of ferrous monosulfide to pyrite. *Geochim. Cosmochim. Acta* **1999,** *63*, (13-14), 2019-2023.

134. Kennedy, L. G.; Everett, J. W.; Gonzales, J., Assessment of biogeochemical natural attenuation and treatment of chlorinated solvents, Altus Air Force Base, Altus, Oklahoma. *J. Contam. Hydrol.* **2006,** *83*, (3-4), 221-236.

135. Davison, W.; Seed, G., The kinetics of the oxidation of ferrous iron in synthetic and natural waters. *Geochim. Cosmochim. Acta* **1983,** *47*, (1), 67-79.

136. King, D. W.; Lounsbury, H. A.; Millero, F. J., Rates and mechanism of Fe(II) oxidation at nanomolar total iron concentrations. *Environ. Sci. Technol.* **1995,** *29*, (3), 818-824.

137. Miller, C. J.; Rose, A. L.; Waite, T. D., Impact of natural organic matter on H_2O_2-mediated oxidation of Fe (II) in a simulated freshwater system. *Geochim. Cosmochim. Acta* **2009,** *73*, (10), 2758-2768.

138. Weber, K. A.; Achenbach, L. A.; Coates, J. D., Microorganisms pumping iron: anaerobic microbial iron oxidation and reduction. *Nat. Rev. Microbiol.* **2006,** *4*, (10), 752-764.

139. Karimian, N.; Johnston, S. G.; Burton, E. D., Iron and sulfur cycling in acid sulfate soil wetlands under dynamic redox conditions: A review. *Chemosphere* **2018,** *197*, 803-816.

140. Dos Santos Afonso, M.; Stumm, W., Reductive dissolution of iron(III) (hydr)oxides by hydrogen sulfide. *Langmuir* **1992,** *8*, (6), 1671-1675.

141. Lovley, D. R.; Holmes, D. E.; Nevin, K. P., Dissimilatory Fe(III) and Mn(IV) reduction. *Adv. Microb. Physiol.* **2004,** *49*, (2004), 219-286.

142. Clément, J.-C.; Shrestha, J.; Ehrenfeld, J. G.; Jaffé, P. R., Ammonium oxidation coupled to dissimilatory reduction of iron under anaerobic conditions in wetland soils. *Soil Biology and Biochemistry* **2005,** *37*, (12), 2323-2328.

143. Kukkadapu, R. K.; Zachara, J. M.; Smith, S. C.; Fredrickson, J. K.; Liu, C., Dissimilatory bacterial reduction of Al-substituted goethite in subsurface sediments. *Geochim. Cosmochim. Acta* **2001,** *65*, (17), 2913-2924.

144. Danielsen, K. M.; Hayes, K. F., pH dependence of carbon tetrachloride reductive dechlorination by magnetite. *Environ. Sci. Technol.* **2004,** *38*, (18), 4745-4752.

145. Stroo, H. F.; Wilson, J. T.; Evans, P. J.; Lebron, C. A.; Henry, B. M.; Latta, D. E.; Ghosh, R. S.; Leeson, A. *In Situ Biogeochemical Treatment Demonstration: Lessons Learned from ESTCP Project ER 201124*; Stroo Consulting, Ashland, United States: **2015**.

146. Lovley, D. R.; Giovannoni, S. J.; White, D. C.; Champine, J. E.; Phillips, E.; Gorby, Y. A.; Goodwin, S., Geobacter metallireducens gen. nov. sp. nov., a microorganism capable of coupling the complete oxidation of organic compounds to the reduction of iron and other metals. *Arch. Microbiol.* **1993,** *159*, (4), 336-344.

147. Singh, S.; Seed, H. B.; Chan, C.-Y., Undisturbed sampling of saturated sands by freezing. *Journal of Geotechnical and Geoenvironmental Engineering* **1982,** *108*, (GT2).

148. Hatanaka, M.; Uchida, A.; Oh-oka, H., Correlation between the liquefaction strengths of saturated sands obtained by in-situ freezing method and rotary-type triple tube method. *Soils and Foundations* **1995,** *35*, (2), 67-75.

149. Yoshimi, Y.; Tokimatsu, J.; Ohara, A., In situ liquefaction resistance of clean sands over a wide density range. *Geotechnique* **1994,** *44*, (3), 479-494.

150. Schulze, T.; Ricking, M.; Schröter-Kermani, C.; Körner, A.; Denner, H.-D.; Weinfurtner, K.; Winkler, A.; Pekdeger, A., The German environmental specimen bank. *J. Soils Sediments* **2007,** *7*, (6), 361-367.

151. Araújo, C. V.; Diz, F. R.; Laiz, I.; Lubián, L. M.; Blasco, J.; Moreno-Garrido, I., Sediment integrative assessment of the Bay of Cádiz (Spain): an ecotoxicological and chemical approach. *Environ. Int.* **2009,** *35*, (6), 831-841.

152.   Kiaalhosseini, S.; Johnson, R. L.; Rogers, R. C.; Renno, M. I.; Lyverse, M.; Sale, T. C., Cryogenic core collection (C3) from unconsolidated subsurface media. *Groundwater Monitoring & Remediation* **2016,** *36*, (4), 41-49.

153.   Sale, T.; Kiaalhosseini, S.; Olson, M.; Johnson, R.; Rogers, R. *Third Generation (3G) Site Characterization: Cryogenic Core Collection and High Throughput Core Analysis-An Addendum to Basic Research Addressing Contaminants in Low Permeability Zones-A State of the Science Review*; Colorado State University, Fort Collins, United States: **2016**.

154.   Cahoon, D. R.; Marin, P. E.; Black, B. K.; Lynch, J. C., A method for measuring vertical accretion, elevation, and compaction of soft, shallow-water sediments. *J. Sediment. Res.* **2000,** *70*, (5), 1250-1253.

155.   Johnson, R. L.; Brow, C. N.; Johnson, R. O. B.; Simon, H. M., Cryogenic core collection and preservation of subsurface samples for biomolecular analysis. *Groundwater Monitoring & Remediation* **2013,** *33*, (2), 38-43.

156.   Pincock, R. E., Reactions in frozen systems. *Acc. Chem. Res.* **1969,** *2*, (4), 97-103.

157.   Grant, N. H.; Clark, D. E.; Alburn, H. E., Imidazole-and base-catalyzed hydrolysis of penicillin in frozen systems. *Journal of the American Chemical Society* **1961,** *83*, (21), 4476-4477.

158.   Grant, N.; Alburn, H., Acceleration of enzyme reactions in ice. *Nature* **1966,** *212*, (5058), 194.

159.   Fan, T.-Y.; Tannenbaum, S. R., Factors influencing the rate of formation of nitrosomorpholine from morpholine and nitrite. II. Rate enhancement in frozen solution. *J. Agric. Food Chem.* **1973,** *21*, (6), 967-969.

160.   Hatley, R. H.; Franks, F.; Day, H., Subzero-temperature preservation of reactive fluids in the undercooled state: II. The effect on the oxidation of ascorbic acid of freeze concentration and undercooling. *Biophys. Chem.* **1986,** *24*, (2), 187-192.

161.   Takenaka, N.; Ueda, A.; Maeda, Y., Acceleration of the rate of nitrite oxidation by freezing in aqueous solution. *Nature* **1992,** *358*, (6389), 736.

162.   O'Concubhair, R.; Sodeau, J. R., The effect of freezing on reactions with environmental impact. *Acc. Chem. Res.* **2013,** *46*, (11), 2716-2724.

163.   Takenaka, N.; Bandow, H., Chemical kinetics of reactions in the unfrozen solution of ice. *The Journal of Physical Chemistry A* **2007,** *111*, (36), 8780-8786.

164. Workman, E.; Reynolds, S., Electrical phenomena occurring during the freezing of dilute aqueous solutions and their possible relationship to thunderstorm electricity. *Physical Review* **1950,** *78*, (3), 254.

165. Gross, G.; Gutjahr, A.; Caylor, K., Recent experimental work on solute redistribution at the ice/water interface. Implications for electrical properties and interface processes. *Le Journal de Physique Colloques* **1987,** *48*, (C1), C1-527-C1-533.

166. Bronshteyn, V. L.; Chernov, A. A., Freezing potentials arising on solidification of dilute aqueous solutions of electrolytes. *J. Cryst. Growth* **1991,** *112*, (1), 129-145.

167. Haymet, A.; Wilson, P., The Workman–Reynolds "Freezing Potential": A new look at the inherent physical process. *J. Mol. Liq.* **2017,** *228*, 243-246.

168. Gross, G. W.; Wong, P. M.; Humes, K., Concentration dependent solute redistribution at the ice–water phase boundary. III. Spontaneous convection. Chloride solutions. *J. Chem. Phys.* **1977,** *67*, (11), 5264-5274.

169. Boxe, C.; Saiz-Lopez, A., Multiphase modeling of nitrate photochemistry in the quasi-liquid layer (QLL): implications for NO x release from the Arctic and coastal Antarctic snowpack. *Atmospheric Chem. Phys.* **2008,** *8*, (16), 4855-4864.

170. Fennema, O. In *Reaction kinetics in partially frozen aqueous systems*, Proceedings of an International Symposium on Water Relations of Foods, **1975**.

171. Raiswell, R.; Canfield, D., Rates of reaction between silicate iron and dissolved sulfide in Peru Margin sediments. *Geochim. Cosmochim. Acta* **1996,** *60*, (15), 2777-2787.

172. Kamyshny, A.; Goifman, A.; Gun, J.; Rizkov, D.; Lev, O., Equilibrium distribution of polysulfide ions in aqueous solutions at 25 C: a new approach for the study of polysulfides' equilibria. *Environ. Sci. Technol.* **2004,** *38*, (24), 6633-6644.

173. Rozan, T. F.; Theberge, S.; Luther III, G., Quantifying elemental sulfur (S^0), bisulfide (HS^-) and polysulfides (S_x^{2-}) using a voltammetric method. *Analytica Chimica Acta* **2000,** *415*, (1-2), 175-184.

174. Rickard, D.; Schoonen, M. A.; Luther, G. In *Chemistry of iron sulfides in sedimentary environments*, ACS symposium series, 1995; ACS Publications: 1995; pp 168-193.

175. Rickard, D., The solubility of FeS. *Geochim. Cosmochim. Acta* **2006,** *70*, (23), 5779-5789.

176. Lovley, D. R.; Phillips, E. J., Organic matter mineralization with reduction of ferric iron in anaerobic sediments. *Appl. Environ. Microbiol.* **1986,** *51*, (4), 683-689.

177. Rickard, D.; Luther III, G. W., Kinetics of pyrite formation by the H_2S oxidation of iron (II) monosulfide in aqueous solutions between 25 and 125 C: the mechanism. *Geochim. Cosmochim. Acta* **1997,** *61*, (1), 135-147.

178. Rickard, D., Kinetics of pyrite formation by the H_2S oxidation of iron (II) monosulfide in aqueous solutions between 25 and 125 C: the rate equation. *Geochim. Cosmochim. Acta* **1997,** *61*, (1), 115-134.

179. Luther III, G. W., Pyrite synthesis via polysulfide compounds. *Geochim. Cosmochim. Acta* **1991,** *55*, (10), 2839-2849.

180. Butler, I. B.; Böttcher, M. E.; Rickard, D.; Oldroyd, A., Sulfur isotope partitioning during experimental formation of pyrite via the polysulfide and hydrogen sulfide pathways: implications for the interpretation of sedimentary and hydrothermal pyrite isotope records. *Earth Planet. Sci. Lett.* **2004,** *228*, (3-4), 495-509.

181. Henneke, E.; Luther III, G. W.; De Lange, G. J.; Hoefs, J., Sulphur speciation in anoxic hypersaline sediments from the eastern Mediterranean Sea. *Geochim. Cosmochim. Acta* **1997,** *61*, (2), 307-321.

182. Wilkin, R.; Barnes, H., Formation processes of framboidal pyrite. *Geochim. Cosmochim. Acta* **1997,** *61*, (2), 323-339.

183. Sweeney, R.; Kaplan, I., Pyrite framboid formation; laboratory synthesis and marine sediments. *Econ Geol* **1973,** *68*, (5), 618-634.

184. Muramoto, J. A.; Honjo, S.; Fry, B.; Hay, B. J.; Howarth, R. W.; Cisne, J. L., Sulfur, iron and organic carbon fluxes in the Black Sea: sulfur isotopic evidence for origin of sulfur fluxes. *Deep Sea Research Part A. Oceanographic Research Papers* **1991,** *38*, S1151-S1187.

185. Harmandas, N.; Navarro Fernandez, E.; Koutsoukos, P., Crystal growth of pyrite in aqueous solutions. Inhibition by organophosphorus compounds. *Langmuir* **1998,** *14*, (5), 1250-1255.

186. Luther III, G. W.; Kostka, J. E.; Church, T. M.; Sulzberger, B.; Stumm, W., Seasonal iron cycling in the salt-marsh sedimentary environment: the importance of ligand complexes with Fe (II) and Fe (III) in the dissolution of Fe (III) minerals and pyrite, respectively. *Mar. Chem.* **1992,** *40*, (1-2), 81-103.

187. Emerson, D.; Fleming, E. J.; McBeth, J. M., Iron-oxidizing bacteria: an environmental and genomic perspective. *Annu. Rev. Microbiol.* **2010,** *64*, 561-583.

188.   Straub, K. L.; Benz, M.; Schink, B., Iron metabolism in anoxic environments at near neutral pH. *FEMS Microbiol. Ecol.* **2001,** *34*, (3), 181-186.

189.   Hedrich, S.; Schlömann, M.; Johnson, D. B., The iron-oxidizing proteobacteria. *Microbiology* **2011,** *157*, (6), 1551-1564.

190.   Cobb, A. W.; Gross, G. W., Interfacial electrical effects observed during the freezing of dilute electrolytes in water. *J. Electrochem. Soc.* **1969,** *116*, (6), 796-804.

191.   Pankow, J. F.; Morgan, J. J., Dissolution of tetragonal ferrous sulfide (mackinawite) in anoxic aqueous systems. 2. Implications for the cycling of iron, sulfur, and trace metals. *Environ. Sci. Technol.* **1980,** *14*, (2), 183-186.

192.   Rickard, D.; Sjoeberg, E. L., Mixed kinetic control of calcite dissolution rates. *Am. J. Sci.* **1983,** *283*, (8), 815-830.